INFORMATION TO USERS

This manuscript has been reproduced from the microfilm master. UMI films the text directly from the original or copy submitted. Thus, some thesis and dissertation copies are in typewriter face, while others may be from any type of computer printer.

The quality of this reproduction is dependent upon the quality of the copy submitted. Broken or indistinct print, colored or poor quality illustrations and photographs, print bleedthrough, substandard margins, and improper alignment can adversely affect reproduction.

In the unlikely event that the author did not send UMI a complete manuscript and there are missing pages, these will be noted. Also, if unauthorized copyright material had to be removed, a note will indicate the deletion.

Oversize materials (e.g., maps, drawings, charts) are reproduced by sectioning the original, beginning at the upper left-hand corner and continuing from left to right in equal sections with small overlaps.

Photographs included in the original manuscript have been reproduced xerographically in this copy. Higher quality 6" x 9" black and white photographic prints are available for any photographs or illustrations appearing in this copy for an additional charge. Contact UMI directly to order.

ProQuest Information and Learning
300 North Zeeb Road, Ann Arbor, MI 48106-1346 USA
800-521-0600

Alignment tolerance study between VCSEL arrays and a new kind of ordered fiber array technology considered for two dimensional parallel optical interconnects.

by

Frédérick Mathieu

Departement of Electrical and Computer Engineering

McGill University, Montreal

August 1999

A thesis submitted to the Faculty of Graduate Studies and Research

in partial fulfilment of the requirements of the degree of

Master of Engineering

Abstract

There is a need for two dimensional parallel optical interconnects for large bandwidth transfer of data over a distance ranging from tens of centimeters to a few meters. Optical transmission of data through "free-space" using imaging or diffractive elements would fulfil this need for very large bandwidth and high throughput density, but is not yet a practical approach. A commercially viable approach in the shorter term is to use optical fiber technologies as the communication medium. Fiber image-guides can be mass produced and are easy to align with the source but have insertion losses of the order of -3 dB. Ordered fiber arrays can be constructed using the same technology as fiber image-guides, and can have lower insertion losses but at the cost of reduced alignment tolerances.

We present a model for the numerical calculation of the insertion loss in ordered fiber arrays when coupling light from an array of VCSELs of equal dimensions. We then apply this model to study the impact of alignment on insertion losses as a function of the different fiber array parameters: core radius and of the individual fiber elements, and the dimensions of the array. We conclude that the alignment tolerances for multimode ordered fiber arrays should be compatible with present-day connector technology.

Sommaire

Il existe un besoin de communiquer optiquement d'énormes quantités d'information de manière parallèle en deux dimensions, et cela sur des distances de quelques dizaines de centimètres à quelques mètres. L'approche qui est de transmettre optiquement l'information dans l'espace par le seul bias de lentilles et d'éléments diffractifs peut satisfaire ce besoin, mais est en ce moment difficilement réalisable. Une approche plus facilement réalisable commercialement serait d'utiliser une technologie basée sur les fibres optiques comme moyen de communication. Les guides d'image peuvent être construits en grandes quantités, sont faciles à aligner avec la source, mais dont l'utilisation occasionne une perte de puissance de l'ordre de -3 dB. Un étalage ordonné de fibres optiques peut être construit par la même méthode qu'un guide d'image et offre la possibilité d'avoir un perte moins importante de puissance, mais dont le coût est une augmentation de la précision nécessaire pour aligner la source.

Nous présentons un modèle qui nous permet de calculer numériquement la perte de puissance induite lors du couplage entre un étalage ordonné de fibres optiques et un étalage de VCSELs aux mêmes dimensions. Nous employons ce modèle pour étudier l'impact de l'alignement sur cette perte de puissance, et ce en fonction des divers paramètres de l'étalage ordonné de fibres optiques: le rayon du coeur des fibres individuelles, et les dimensions de l'étalage. Lorsque notre analyse est menée a bien, nous

pouvons conclure que les conditions nécessaires pour aligner adéquatement ces étalages sont compatibles avec les technologies déjà en place pour la production de connecteurs.

Table of contents

List of tables

List of figures

Acknowledgments

I would like to first of all thank my research advisor, professor Andrew Kirk, without whom this thesis would never have been finished. Thank you for your great patience when faced with my often slow progress. Thank you for giving me the opportunity to do research in the amazing field that is photonics.

I wish to also thank Colm Cryan and Schott Fiber Optics Ltd. for their kind donation of fiber array samples.

Thank you to my colleagues of the Photonic Systems Group, professor Dave Plant, and especially Xue Xin and Cheung Fan for teaching me a few words of Chinese. Congratulations Fan for having your baby.

Finalement, je desire remercier ma famille et mes amis, dont le support m'a été indispensable. Une grande bise à Lucie qui m'a toujours conseillé de ne pas être trop perfectionniste.

The work described in this thesis has been supported by the Canadian Institute for Telecommunications Research, the Nortel/NSERC industrial research chair in photonic systems, NSERC (OGP0194547), and FCAR (NC-1778).

Chapter 1

Introduction

In the last decade, tremendous effort has been expended by the industrial and research community in order to interconnect the world and to find better ways to do it. The role of optics to communicate information is becoming increasingly important and optical fiber is already the mainstay of long-distance telecommunications. The ability to use light to interconnect electronic devices in other types of applications is presently under intense scrutiny.

But what advantages do optical interconnects have over their electrical counterparts? From a purely physical standpoint, both types of interconnect carry signals in the form of electromagnetic waves. The real difference between electrical and optical physics stems from the higher carrier frequency (500 THz for light versus 0.001-10 GHz for electronics) for radiation in the optical range (Miller 1997). This single fact has several far reaching consequences.

One consequence is that since the carrier frequency of light is much greater than practical modulation frequencies, high speed modulation creates no frequency-dependent losses or signal distortion. Dispersive effects resulting from high-speed modulation are

usually only present over large distances in optical fiber, and losses are typically 0.2 dB/km. In electrical interconnections, the skin effect and/or filtering effects resulting from the equivalent RC circuit of the line create large signal distortions at high speeds. Distortion leads to intersymbol interference and create many challenges in system design, such as the reliable extraction of timing information (Miller 1997). Also, electrical wires are good antennas at high frequencies, leading to frequency-dependent crosstalk, an effect that is essentially absent in optical interconnects because light waves do not interact in a linear medium. Other benefits of optical transmission over electronic transmission include: ability to create very short femtosecond pulses, wavelength-division multiplexing, ability to use low-loss dielectric materials, voltage isolation, lower power consumption and the possibility to use free-space propagation of the signal (Tooley 1996; Miller 1997). Last but not least, optics offers the opportunity to arrange channels in two dimensions to increase interconnection density.

Despite the possible advantages, from an engineering point of view, optical interconnects will only be viable alternatives if they can deliver increased performance and solve design problems at a reasonable cost. An important challenge is the identification of applications which can best take advantage of the benefits of optical interconnects (Tooley 1996). Many interconnection levels exits: chip-to-chip, board-to-board, box-to-box, etc. Because the power consumed to transfer data electrically increases with distance for a given level of performance, while optical transmission is independant of it, some studies have argued that an appropriate application for optical interconnects is one which needs to communicate large bandwith over an estimated distances no shorter than tens of millimeters. Since the most serious interconnection bottleneck occurs at the board to board level,

which transfers data over a lenght of approximately 30 cm, and where physical constraints (such as the number of connections that can fit on the edge of a board) limit the performance of electronic data transmission in electrical backplanes (Plant 1997), an optical backplane would represent an attractive solution because of its high interconnection density. How can such a link be implemented at low cost?

Vertical-cavity surface-emitting lasers (VCSELs; Iga et al. 1988), are very promising candidates among emitter technologies for interconnect design. They are amenable to on-wafer processing, testing and screening. This saves on handling and labor time, and is conducive to high yields (Morgan et al. 1991; Lebby et al. 1996). VCSELs can be easily fabricated in two-dimensional arrays, are compatible with flip-chip bonding techniques, and do not require any cleaving or individual anti-reflection coatings. Furthermore, only simple drive circuits are required because of the low threshold currents (<100 μA; Hayashi et al. 1996), low operating voltage (< 2V; Choquette et al. 1994) and low power consumption which characterizes these devices. All these factors contribute in achieving low cost. In addition, high wall-plug efficiencies(57%; Jäger et al. 1997) and high-speeds, with modulation bandwidths of 16.3 GHz (Lebby et al. 1996), have been reported.

Another desirable feature of VCSELs is superior beam characteristics compared to the older edge-emitting semiconductor laser structures. Indeed, the beam from an edge-emitter is highly elliptical, with a divergence as large as 50 degrees, which presents a challenge when coupling to optical elements is necessary. By contrast, VCSELs can be fabricated to exhibit a stable, circular symmetric TEM_{00} (Gaussian) transverse mode (Morgan et al. 1993 &1995; Sandusky & Brueck 1996) with low divergence (~12 degrees WFHM). Also, because the basic structure of a VCSEL consists of a thin (~ 1 λ) active

region surrounded by two stacks of alternating quarter-wavelength thick semiconductor layers, both of which are acting as distributed Bragg reflectors, a single well-defined longitudinal mode can be produced. Finally, polarization control can be achieved in VCSELs over a wide temperature range (Takahashi et al. 1997), which is important in low-noise applications where polarization fluctuations can cause excessive intensity noise even in single transverse mode operations (Mukaihara et al. 1995).

After choosing an appropriate emitter technology, an important step in the design process is the choice of a suitable medium for optical power propagation. One method of implementing an optical backplane is by using the "free-space" approach. A plane of emitters can be imaged onto a plane of receivers using simple optical elements: lens, lenslet arrays, beamsplitters, etc. In this way, thousands of beams can be routed, to obtain extremely high interconnection densities. Working optical systems with more than 60 000 beams have been demonstrated under laboratory conditions (Hinton et al. 1994). Beams can cross through one another without interference, and with the ability of free-space optics to provide large power fan out per node and spatial-angular multiplexing, it becomes possible to implement global topologies such as perfect shuffles (Brenner and Huang 1988) and crossover networks (Jahns and Murdocca 1988). The high connectivity of these types of networks makes them amenable for massively parallel computer applications.

At present, many technological hurdles have to be overcome to make free-space commercially viable. The most pressing concerns involve the initial precision to which it is possible to align the system and the precision required to maintain this alignment during operation on the field (Tooley 1996). Directly related to these issues are the high cost and

difficulty of manufacturing the optics and optomechanics involved, and the cost, frequency and difficulty of system maintenance (or repair).

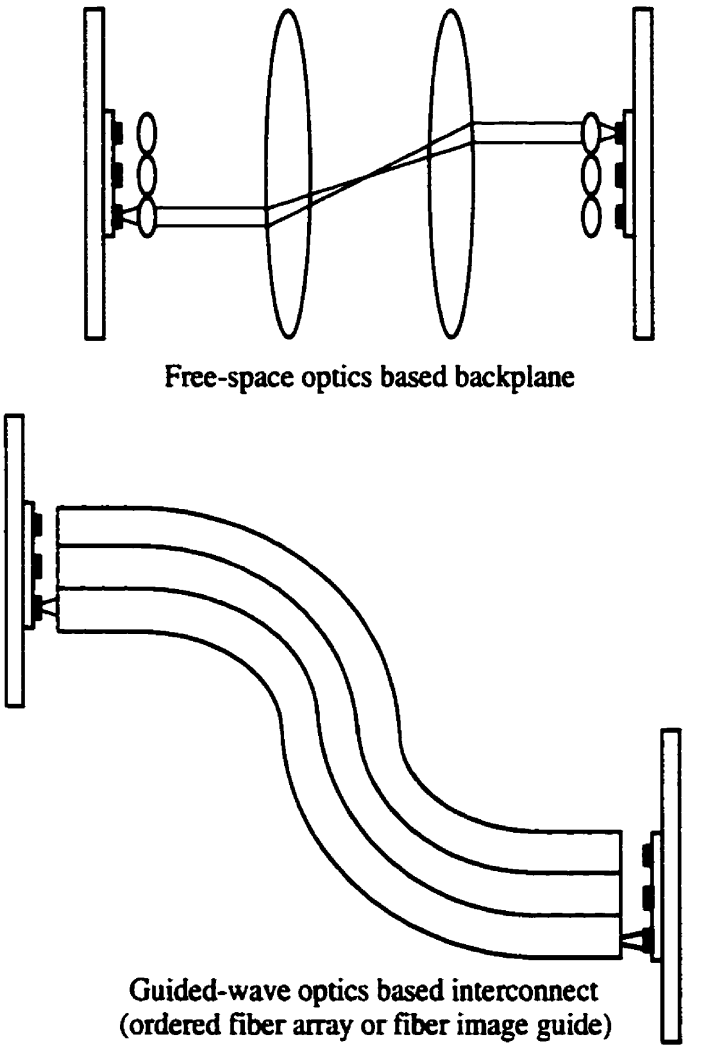

FIGURE 1.1 Free-space approach to optical backplanes versus guided-wave approach

Until the low-cost practical packaging of free-space interconnections can be demonstrated, a waveguide based approach could provide a cheaper and more practical alternative. Because the channels can no longer cross or fan out, such an approach would be suitable for point-to-point applications, where the high connectivity of global

topologies possible with free-space optics are not required. Because of the suppleness of optical fiber, there is built-in flexibility against motion during operation, and greater freedom in board positioning. By contrast, board connected by free-space optics must be kept rigid and interboard spacing cannot be changed for a given optical design (figure 1.1).

Two promising fiber technologies have been marked for use in 2D short-distance (<100m) applications: fiber image-guides (Kosaka et al.1997; Kawai 1997) and ordered multimode fiber arrays (Kirk et al. 1997). The difference between both technologies is basically one of fiber pitch.

A fiber image-guide, well-known for its applications in medical endoscopes, consists typically of around 10 000-20 000 fibers in a closely-packed, hexagonal lattice. The individual fibers will have diameters of up to approximately 8 μm. High bit-rate parallel transmission using a two-dimensional VCSEL array through a fiber-image guide was demonstrated (Kosaka et al.1997). Because of the tight pitch, each beam couples to a cluster of neighboring fibers, thus creating at the output "exact" copies of the pattern of spots at the input. Because of the large transmission surface available and the absence of any significant dependence on lateral displacement, alignment at the input end is very easy. In this way, 1 Gb/s per channel data transmission at a distance of 1 m was shown, with a bit-error rate of 10^{-8} and an average received power of -27.7 dBm. With a 6x6 VCSEL array, the total throughput was 36 Gb/s.

Despite the relaxed alignment tolerances of fiber image-guides, coupling efficiency at the input plane is limited by the ratio of the core area to total fiber cross-section (~50-60 %; Cryan 1998). Because the bit-error rate (BER) of an interconnect and optical

power are directly related, where increased optical power translates to a lowering of the BER, the limited efficiency of the fiber-image guides could have a negative impact in applications such as optical backplanes, which requires very reliable data transmission. Increasing the core size ratio can be done but at the expense of increasing background optical crosstalk.

Results for fiber image-guides are in sharp contrast with those for multimode fiber arrays. With multimode fiber, a BER at 1 Gb/s of less than 10^{-11} was measured for an average received power of -26 dBm and a link distance of 5 m (Kosaka et al.1997). With graded-index fibers, even better performance can be achieved (BER<10^{-11} at -28 dBm for a 1 Gb/s 100 m link; Schnitzer et al. 1996). Arrayed multimode fibers thus become an attractive solution when high transmission efficiency of optical power and low bit-error rates are required. For ordered fiber arrays, each beam couples to a single fiber, in which case stricter initial alignment at the input is required.

Several methods of fabrication to create a generic two dimensional interconnect technology with fiber arrays have been previously been presented in the literature. Many of these techniques involve fitting commercially available optical fiber into a lattice of precision holes on a substrate and then held in place with UV cured epoxy (Koepf and Marley1984; Sasian et al. 1994; Proudley, Stace and White 1994). By referencing light exiting the core of each individual fiber to a second, lithographically made, array of annuluses, and subsequently gluing the fibers into place inside the oversized holes, a 4x8 array was constructed (Sasian et al. 1994) ,with fiber ends deviating no more than 1.5 μm from

their ideal location and accurately pointed to within 30 arc-minutes from the ideal exit angle (90 degrees with respect to the output surface).

These techniques have a few disadvantages. The precise placement of each fiber is time consuming (~10 min/fiber) and becomes exceedingly difficult for larger arrays. A single mishap in the placement of a fiber ruins the array. Also, using epoxy for assembly lacks the stability available with an all-glass construction.

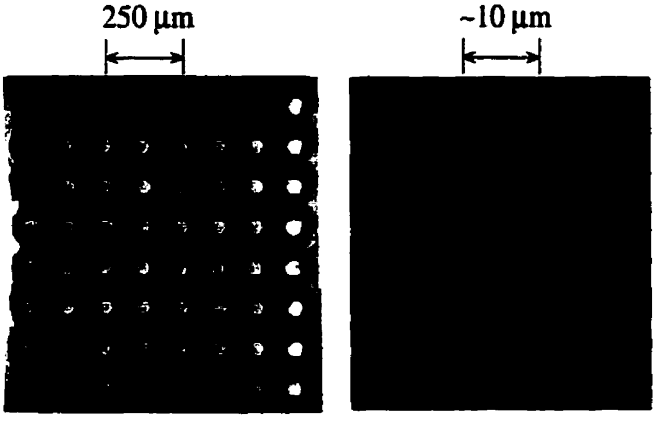

FIGURE 1.2 Fused glass fiber arrays. Ordered fiber array (left) and fiber image-guide (right). Note the difference in the spacing between individual fibers.

A novel approach to array construction is the use of fiber image-guide manufacturing technology. Instead of the usual closely-packed hexagonal structure, a regular square lattice (figure 1.2) is made (Kirk et al. 1997; Cryan 1998). Each individual fiber that makes up the array is fabricated using the rod in tube method. The fiber preform consists of three concentric glass layers. The central layer is a high-index core, the intermediate layer a low index cladding, and the outer layer a acid soluble glass. The optical properties of the array is determined primarily by the choice of core materials. Attenuation coefficients of 0.2

dB/km and numerical apertures between 0.1 and 1.25 can be achieved with commercially available glasses.

The size of each core and separation between cores is determined by selecting appropriate glass rods and tubes. The fiber preforms are drawn into fused fiber rods approximately 1 m long and 4 mm in diameter. The draw is carried out with standard production equipment, and carefully monitored in order to control the diameter and cross-section of each rod. These fiber rods are then individually located in a square lattice configuration. Accurate alignment at this stage is possible because of the large diameter and flexural rigidity of the rods. In addition, location errors occurring at the assembly stage will be reduced in proportion to the draw down ratio. The array of rods is drawn to a length of 1 m and a diameter of 1mm. During the draw, the individual fiber elements fuse together, filling any interstitial gaps in the array. A typical preform array will yield approximately eighty 1 m interconnects. Each face can then be polished perpendicular to the fiber axis. In this way, an 8x8 array was constructed, with a core diameter of 50 μm and a pitch of 125 μm. The location of center of each core was measured to be within 5 μm of their ideal position. No fiber deviated by more than 0.3 milliradians from the ideal exit angle (Cryan 1998). Arrays with core diameters of 100 μm and a pitch of 250 μm were also drawn (Kirk et al.1997).

A flexible array can be fabricated by removing the acid soluble glass along the center of the array while preserving the fused sections at both ends. Selective removal of the glass can be achieved by protecting the ends with an acid resistant coating. The array can then be inserted into a flexible outer jacket for better mechanical stability.

In order to justify the use of this novel fiber array technology for parallel optical interconnects, ease of fabrication cannot be the sole determinant of its merit. The optical properties of an array and their influence on packaging strategies must also be determined. From these, the alignment requirements of the array and of each fiber element in the array is of great consequence, since alignment has a direct impact on such things as coupling efficiency, power uniformity across the array and optical crosstalk. These alignment tolerances in turn determine the precision of the optomechanics necessary to build the package.

What are the alignment requirements for a fused glass ordered fiber array? How does core radius, pitch between fiber, array size and numerical aperture influence these tolerances? The objective of this thesis is to provide a theoretical answer to these questions using the optical power coupling efficiency between the VCSEL array and fiber array as a figure of merit. In chapter 2, we present the mathematical framework necessary to obtain an expression for the coupling efficiency. The model assumes a single-clad fiber configuration of the modes (Appendix A) and a Gaussian beam (Appendix B) for each VCSEL's output. In chapter 3, we proceed to the numerical evaluation of the expressions found in chapter 2 as a function of the parameters of interest. From these results, a conclusion about the feasibility of using fused glass ordered fiber arrays for optical interconnects, on the basis of its alignment requirements alone, will be presented in chapter 4.

Chapter 2

Launching of Gaussian beams into multimode optical fiber

2.1 Mode excitation by plane waves

Snyder (1969b) developed a model by which he obtained an expression for the launching efficiency of plane waves into a dielectric rod. It is useful to follow this method since it can be adapted readily to optical fiber and to other types of beams.

Figure 2.1 illustrates the geometry to consider. A semi-infinite optical fiber, with core refractive index n_1 and cladding refractive index n_2, is excited by a plane wave propagating at oblique incidence θ over an aperture d. The aperture can represent the finite radius of the waveguide or an otherwise truncated incident field. The core radius is a.

An exact analysis of the aperture fields at the fiber face is extremely complicated, and requires knowledge of the dyadic Green's functions and the evaluation of a complex integral equation (Morse and Feshbach1953; Smith 1997). But the analysis simplifies considerably by assuming that the complex amplitudes of the electric and magnetic fields in the aperture ($\boldsymbol{E}^t$, $\boldsymbol{H}^t$) is produced by a plane wave ($\boldsymbol{E}$,$\boldsymbol{H}$) from a uniform dielectric interface; that is, the presence of an aperture or a change in the refractive index across the fiber

face has little effect on the field. Inasmuch as the incident field is also a plane wave, the problem can be thus be approximately solved by considering it equivalent to the transmission of plane waves across a semi-infinite and uniform dielectric interface. The above assumption, similar to that of Born's or Kirchhoff's (Morse and Feshbach1953; Smith 1997), is reasonable only if the core radius a is much larger than the wavelength, or if the difference between n_1 and n_2 is small (in which case the aperture, d, itself must be much larger compared to the wavelength).

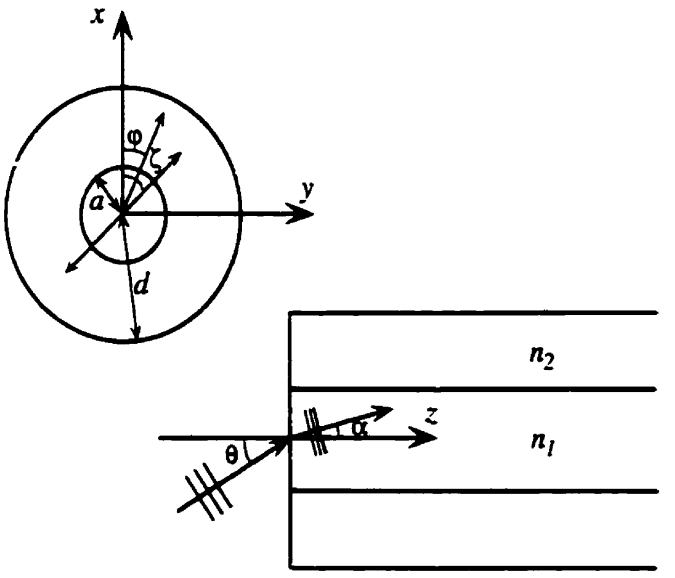

FIGURE 2.1 Optical fiber excited a by plane wave field over an aperture $d \geq a$.

The Born-Kirchhoff approximation leads to the following expressions for the field components in the x-y plane:

$$\begin{aligned} \boldsymbol{E}^t &= \boldsymbol{E} = t\boldsymbol{E}^{inc} \\ \boldsymbol{H}^t &= \boldsymbol{H} = (\hat{z} \times \boldsymbol{E})Y \end{aligned} \tag{2.1}$$

where Y is the z-directed admittance, and t is the appropriate Fresnel transmission coefficient. Precise techniques have shown that equation (2.1) gives excellent accuracy in cases of practical importance (El-Mikati and Davies 1985). The Fresnel reflection coefficient for the glass-air interface is typically around 4% for normal incidence and is consistent with results which show that the reflected power is less than 4% of the incident power for single-clad fibers (Mostafavi et al. 1975)

The transverse fields at the fiber aperture (z=0+) can be represented as an expansion of appropriate orthonormal eigenfunctions; i.e. the modal solutions of the electric and magnetic fields, $\boldsymbol{e}_p$ and $\boldsymbol{h}_p$ respectively, for single-clad cylindrical dielectric waveguides

$$\begin{aligned} \boldsymbol{E}^t &= \sum_p a_p \boldsymbol{e}_p(x, y) \\ \boldsymbol{H}^t &= \sum_p a_p \boldsymbol{h}_p(x, y) \end{aligned} \tag{2.2}$$

The radiation field, the portion of the power not guided by the optical fiber, is also included in the notation. Expressions for the modes are derived in appendix A.

The exact mathematical expressions for the modes in a cylindrical dielectric waveguide, although well known, are generally unwieldy and not transparent to physical interpretation. The expressions for the modes can be greatly simplified by making the assumption that the difference in dielectric constants between the cladding and the core of the fiber is very small. Since this assumption is implicit to our Born-Kirchhoff approximation, manipulating the exact formulas for the modes would not convey any additional information and are thus unnecessary. Also, most optical fibers used by the telecommunications industry have indeed very small dielectric constant differences between the core

and cladding. We are thus justified in using the approximate mode solutions (A-44), appropriate for weakly-guiding cylindrical waveguides, in our analysis. Also, since the modes are orthogonal to the z axis in this approximation, only the transverse components of the aperture field will be guided.

The amplitude coefficients a_p are found via the orthogonality relations (Collin 1960)

$$\int (\boldsymbol{e}_p \times \boldsymbol{h}_q^*) \cdot \hat{\boldsymbol{z}} dA = \begin{cases} 0 & p \neq q \\ 1 & p = q \end{cases}. \tag{2.3}$$

where the integration is performed over the entire cross-section ($dA=\rho d\rho d\varphi$). With (2.2) and (2.3) a_p is

$$a_p = \int (\boldsymbol{E}^t \times \boldsymbol{h}_p^*) \cdot \hat{\boldsymbol{z}} dA. \tag{2.4}$$

or

$$a_p = \int (\boldsymbol{e}_p^* \times \boldsymbol{H}^t) \cdot \hat{\boldsymbol{z}} dA. \tag{2.5}$$

In the context of the weakly-guided approximation, the magnetic field of the mode is related to the electric field by

$$\boldsymbol{h}_p = \sqrt{\frac{\varepsilon_1}{\mu}} \hat{\boldsymbol{z}} \times \boldsymbol{e}_p. \tag{A-34}$$

We now have all the ingredients necessary to estimate the launching efficiency in each mode by an incident plane wave. Using (A-34) into (2.4) and (2.1) into (2.5), the amplitude coefficient becomes

$$a_p = \sqrt{\frac{\varepsilon_1}{\mu_0}}\int[\boldsymbol{E}\times(\hat{z}\times\boldsymbol{e}_p)]\cdot\hat{z}dA = \sqrt{\frac{\varepsilon_1}{\mu_0}}\int[(\boldsymbol{E}\cdot\boldsymbol{e}_p)\hat{z}-(\boldsymbol{E}\cdot\hat{z})\boldsymbol{e}_p]\cdot\hat{z}dA$$
$$= \sqrt{\frac{\varepsilon_1}{\mu_0}}\int(\boldsymbol{E}\cdot\boldsymbol{e}_p)dA \qquad (2.6)$$

or

$$a_p = Y\int[\boldsymbol{e}_p\times(\hat{z}\times\boldsymbol{E})]\cdot\hat{z}dA = Y\int[(\boldsymbol{E}\cdot\boldsymbol{e}_p)\hat{z}-(\boldsymbol{e}_p\cdot\hat{z})\boldsymbol{E}]\cdot\hat{z}dA$$
$$= Y\int(\boldsymbol{E}\cdot\boldsymbol{e}_p)dA \qquad (2.7)$$

where we have used the identity

$$\boldsymbol{a}\times(\boldsymbol{b}\times\boldsymbol{c}) = (\boldsymbol{a}\cdot\boldsymbol{c})\boldsymbol{b}-(\boldsymbol{a}\cdot\boldsymbol{b})\boldsymbol{c} \ . \qquad (2.8)$$

and the orthogonality of the fields to the z axis. In order for (2.6) and (2.7) to be compatible, the condition $Y \equiv \sqrt{\varepsilon_1/\mu_0}$ must be satisfied. Generally, this can only be the case when the angle of incidence is small.

The modal power or launching efficiency is defined as

$$P_p \equiv \frac{|a_p|^2}{2} = \frac{1}{2}\left(\frac{\varepsilon_1}{\mu_0}\right)\left|\int(\boldsymbol{E}\cdot\boldsymbol{e}_p)dA\right|^2 . \qquad (2.9)$$

The plane wave is taken as propagating in the fiber at angle α with the z axis in the x-z plane. This angle is related to the propagation angle of the plane wave outside the fiber, θ, via the paraxial Snell's Law; i.e. $\theta=n_1\alpha$. The tranverse field, at z=0+, associated with the linearly polarized plane wave is given by

$$\boldsymbol{E} = E_0 e^{-jkx\sin\alpha}(\hat{x}\cos\alpha\cos\zeta + \hat{y}\sin\zeta) \ , \tag{2.10}$$

where E_0 is a normalization constant given by

$$E_0^2 = \frac{2}{\pi d^2}\sqrt{\frac{\mu_0}{\varepsilon_1}}, \tag{2.11}$$

and ζ is the angle the polarization makes with the x axis (see fig. 2.1). Since we are concerned only with small angles of incidence, the polarization of the incident field is, to first order of α, in the x-y plane. With the transformation $x = \rho\cos\varphi$, and for $\alpha \ll 1$, the incident field becomes

$$\boldsymbol{E} = E_0 e^{-jR\Delta\cos\varphi}(\hat{x}\cos\zeta + \hat{y}\sin\zeta) \ , \tag{2.12}$$

where

$$\Delta = ak\ \alpha = ak_0\theta, \tag{2.13}$$

and $R=\rho/a$.

From (2.12), it can be seen that the amplitude of the incident field has even (cosine) symmetry about the $\varphi = 0$ axis. The excited modes must then also have even symmetry, otherwise P_p will be zero (which follows from the orthogonality of the sine functions). From inspection of equations (A-44), it can be seen that all the hybrid modes will be excited independent of the polarization of the incident beam, since cosine modes exists for both the x and the y polarizations. However, when the incident field is polarized in the x

direction, there are no TE modes and when it is polarized in the *y* direction, there is no TM field.

For hybrid modes, after substituting (A-44) and (2.12) into (2.9), and removing terms that are not cosine symmetric, the launching effciency becomes

$$P_p = \frac{1}{2}\left(\frac{\varepsilon_1}{\mu_0}\right)\frac{E_0}{\psi_p}\left|\int f_l(R)e^{-jR\Delta\cos\varphi}\cos(l \mp 1)\varphi dA\right|^2 \begin{pmatrix} \cos^2\beta \\ or \\ \sin^2\beta \end{pmatrix}. \qquad (2.14)$$

From this last equation, we can see that power is launched in both possible modes of the degenerate set. The total power launched is

$$P_p = \frac{1}{2}\left(\frac{\varepsilon_1}{\mu_0}\right)\frac{E_0}{\psi_p}\left|\int f_l(R)e^{-jR\Delta\cos\varphi}\cos(l \mp 1)\varphi dA\right|^2 \qquad \text{hybrid} \qquad (2.15)$$

For TM and TE modes, the launching efficiency is expressed by

$$P_p = \frac{1}{2}\left(\frac{\varepsilon_1}{\mu_0}\right)\frac{E_0}{\psi_p}\left|\int f_0(R)e^{-jR\Delta\cos\varphi}\cos\varphi dA\right|^2\cos^2\beta \qquad \text{TM} \qquad (2.16)$$

and

$$P_p = \frac{1}{2}\left(\frac{\varepsilon_1}{\mu_0}\right)\frac{E_0}{\psi_p}\left|\int f_0(R)e^{-jR\Delta\cos\varphi}\cos\varphi dA\right|^2\sin^2\beta \qquad \text{TE.} \qquad (2.17)$$

respectively. The total power launched in these modes is given by

$$P_p = \frac{1}{2}\left(\frac{\varepsilon_1}{\mu_0}\right)\frac{E_0}{\psi_p}\left|\int f_0(R)e^{-jR\Delta\cos\varphi}\cos\varphi da\right|^2 \qquad \text{TM + TE.} \qquad (2.18)$$

which is identical to (2.15) with l=0.

The phase term in (2.15) is expanded as a sum of Bessel functions,

$$e^{-jR\,\Delta\cos\phi} = J_0(R\,\Delta) + 2\sum_{i=1}^{\infty}(-j)^i J_i(R\,\Delta)\cos i\,\phi\,. \tag{2.19}$$

We then integrate over φ and use the orthogonality property of the cosines,

$$\int_0^{2\pi}\cos mx\,\cos nx\,dx = \begin{cases}\pi\delta_{mn} & n\neq 0\\ 2\pi\delta_{mn} & n=0\end{cases}, \tag{2.20}$$

where

$$\delta_{mn} = \begin{cases}0 & m\neq n\\ 1 & m=n\end{cases}. \tag{2.21}$$

which leads to

$$P_p = (2\pi a^2)\frac{1}{2}\left(\frac{\varepsilon_1}{\mu_0}\right)\frac{E_0}{\psi_p}I^2 = \frac{1}{\xi}\left(\frac{2U_pI}{VD}\right)^2. \tag{2.22}$$

I is the integral

$$I = \begin{cases}\int_0^D f_l(R)J_{l\mp 1}(R\,\Delta)RdR & \text{hybrid}\\ \int_0^D f_0(R)J_1(R\,\Delta)RdR & \text{TM}+\text{TE}\end{cases}. \tag{2.23}$$

D=d/a is the normalized aperture radius, and the appropriate expressions for E_0 and ψ_p, (2.11) and (A-42), have been used. The definition of f_l is given by (A-40).

Since we used the expression for a normalized field *in the fiber*, we need only multiply (2.2) by the appropriate Fresnel power transmittance to obtain the coupling efficiency of the incident field *outside the fiber*; that is, for near normal incidence,

$$T = 1 - \left(\frac{1-n_1}{1+n_1}\right)^2. \tag{2.24}$$

Equation (2.22) is plotted for a beam with a diameter equal to the core's (D=1), that strikes the fiber at normal incidence (Δ=0), for some of the lower order modes (fig.2.2). As shown by Snyder (1969b), only the HE_{1m} modes are excited in the case of normal incidence, since $J_{n-1}(0)$=0 for all n≠1, with the HE_{11} mode being the dominant mode for all values of V (the normalized frequency; see equation (A-4)).

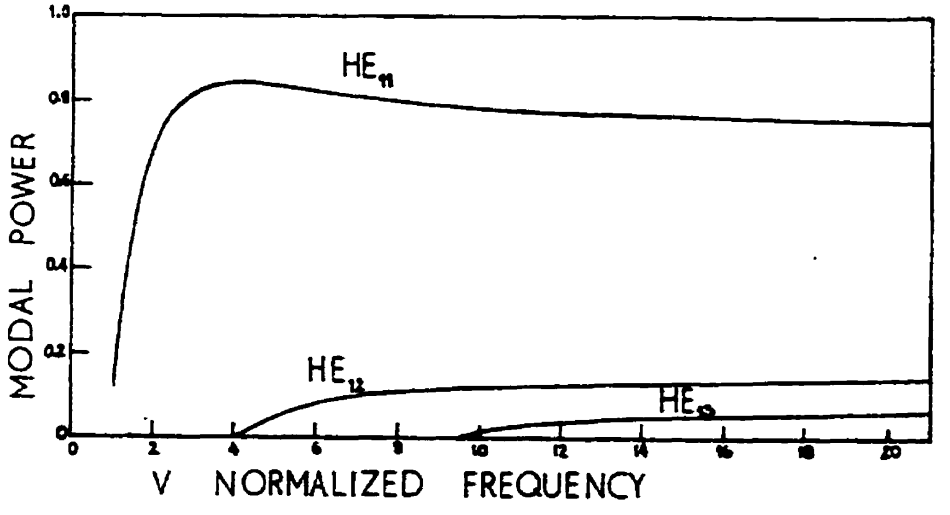

FIGURE 2.2 Modal launching efficiency at normal incidence and D = 1 (Snyder 1969b).

The modal launching efficiency is very sensitive to any deviation of the angle from normal incidence. From fig.(2.3), we can see that as the angle deviates from normal inci-

dence, the HE_{11} mode declines sharply and modes not present at normal incidence, are excited. Results from Snyder (1969b) shows that, far from cutoff, a mode reaches maximum launching efficiency when

$$U_p = \Delta, \tag{2.25}$$

except HE_{11} which dominates at normal incidence. Also, since the efficiency curves for the modes overlap greatly, it is very difficult to stimulate a mode without exciting another.

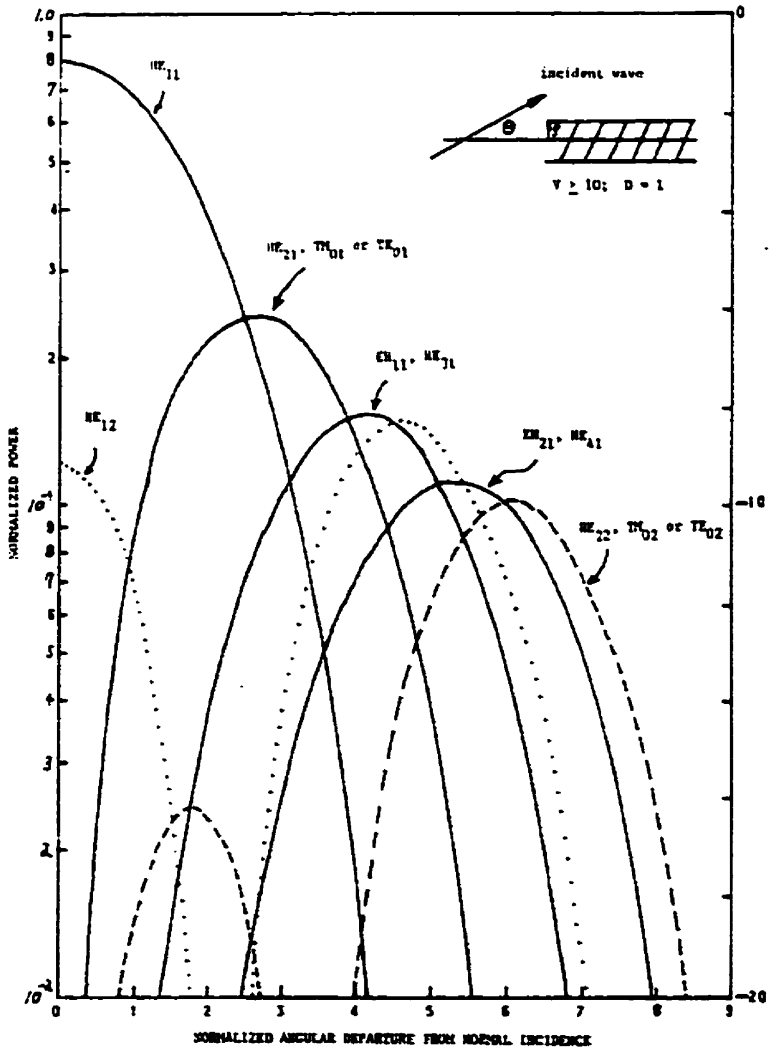

FIGURE 2.3 Modal launching efficiency of a tilted beam, far from cutoff, and $D = 1$ (Snyder 1969b).

2.2 Mode excitation by a Gaussian beam

Snyder's method can be readily adapted to incident Gaussian beams by simply assuming that the aperture field is now also Gaussian (a Born-Kirchhoff approximation). Under this assumption, equation (2.9) for the modal power remains valid. The earliest work investigated the launching efficiency into the HE_{11} mode as a function of V (Stern et al.1970), lateral offset (Stern & Dyott 1971), tilt and beam radius (Marcuses 1970), but was limited to a fiber face positioned at the beam waist, in which case the effects of the wavefront curvature could be neglected. Further work aimed to include the effects of beam curvature, and to determine the launching efficiencies into higher order modes (Imai & Hara 1974; *idem* 1975; Miyagi et al.1975). The technique was also adapted to doubly clad waveguide structures (Cartledge 1978; Chandra 1979). None of these papers consider any changes to the Gaussian beam as it crosses the dielectric interface.

2.2.1 Tilted beams

Let us consider replacing the previous plane wave by a Gaussian beam. We define the coordinate system $x'y'z'$ whose origin is located at the beam waist, where the z' axis coincides with the center of the beam, and $y'=y$. The z' axis crosses the center of the fiber face, at an oblique angle θ with the z axis in the x-z plane. The origins of the coordinate system are separated by a distance b (figure 2.4).

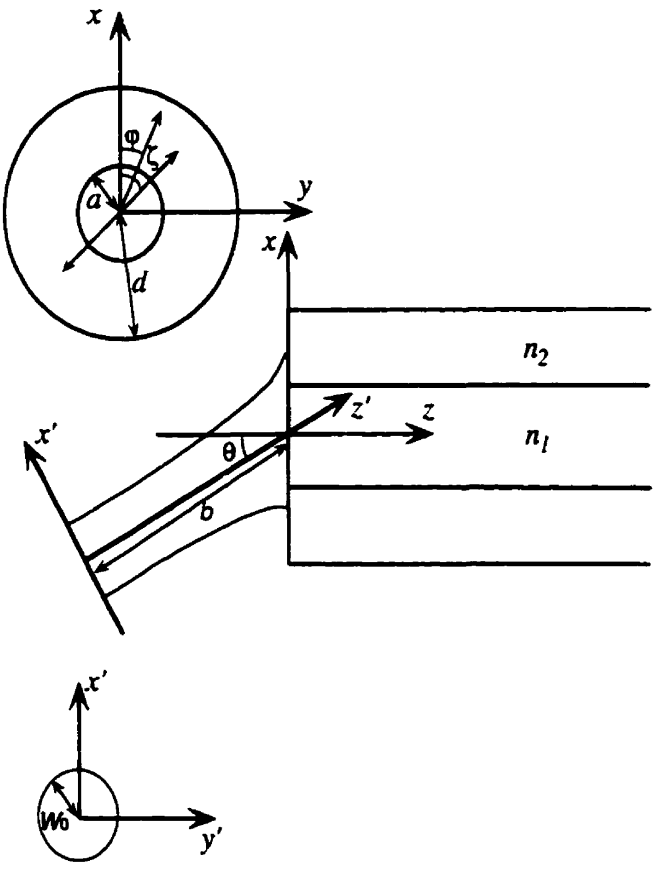

FIGURE 2.4 Considered geometry for tilted Gaussian beams

Our assumption that the field remains Gaussian once it crosses the fiber face deserves further comment. What is the actual form of the reflected and transmitted field? To answer this question, the problem of Gaussian beam interaction with a planar dielectric interface, as a function of arbitrary values of θ, was investigated by several authors (Horowitz & Tamir 1971; Ra et al. 1973; Antar & Boerner 1973; White et al. 1977; Kozaki and Sakurai 1977). Most work involve the use of Fourier optics where the incident beam is expanded as a function of an infinite set of plane waves of varying spatial frequency, to which the well known Fresnel coefficients are applied. Results show that the transmitted and reflected beam is distorted from its Gaussian shape. Among well established effects are a

lateral and angular shift of the path of the beam "center" away from the path described by geometrical optics.

For well collimated beams (kw_0>>1) or, equivalently, for small far-field divergence, analytical expressions for the reflected and transmitted beam can be obtained. These expressions show that the fields are composed of a "fundamental mode" which is Gaussian in shape and whose amplitude is corrected by the appropriate Fresnel coefficient, and to which are added higher order terms which take into account the distorsions present. A careful review of these expressions suggests to us that the higher order terms can be neglected for small deviations from normal incidence. Thus our basic assumption that the aperture field is Gaussian is valid for small values of θ, and for beams that are paraxial. Also it can be assumed that the beam axis follow the path described by geometrical optics (Snell's law).

Thus, the normalized field just inside the fiber aperture is obtained from (B-16),

$$E(x'', y'', z'')|_{z=0} = \frac{2\sqrt{\frac{\eta}{\pi}}}{w''(z'')} e^{j\Phi''(z'')} e^{-\left(\frac{\rho''}{w''(z'')}\right)^2} e^{-j\left(kz'' + \frac{k\rho''^2}{2\Gamma''(z'')}\right)} (\hat{x}''\cos\zeta + \hat{y}''\sin\zeta)\Big|_{z=0} . \tag{2.26}$$

The coordinate system of the transmitted Gaussian beam, $x''y''z''$ (not shown in figure 2.4), is defined such that its origin is at the center of the beam waist which is located at a distance b'' from the center of the fiber face, $y''=y$, and z'' is the direction of propagation. The z'' axis makes an angle α with the z axis, and by Snell's law, $\theta=n_1\alpha$. As in the previous case for plane waves, for small angles the polarization is approximately in the xy plane and

makes an angle ζ with the x axis. Using the well known formulas for transforming coordinates under translation and rotation,

$$\begin{aligned} z'' &= (z-z_0)\cos\alpha + (x-x_0)\sin\alpha \approx (z-z_0) + (x-x_0)\alpha \\ x'' &= (x-x_0)\cos\alpha - (z-z_0)\sin\alpha \approx (x-x_0) - (z-z_0)\alpha \\ z_0 &= -b''\cos\alpha \approx -b'' \\ x_0 &= -b''\sin\alpha \approx -b''\alpha \\ \rho''^2 &= x''^2 + y''^2 = x''^2 + y^2 \end{aligned} \quad , \tag{2.27}$$

(2.26) becomes, to first order of α,

$$\begin{aligned} &\boldsymbol{E}(x'', y'', z'')\big|_{z=0} \\ &= \frac{2\sqrt{\frac{\eta}{\pi}}}{w''(b''+x\alpha)} e^{j\Phi''(b''+x\alpha)} e^{-\left(\frac{\rho}{w''(b''+x\alpha)}\right)^2} e^{-j\left[k[b''+x\alpha] + \frac{k\rho^2}{2\Gamma''(b''+x\alpha)}\right]} (\hat{x}\cos\zeta + \hat{y}\sin\zeta) \end{aligned} \tag{2.28}$$

In practical cases, $1/w''$ and $1/\Gamma''$ are generally slowly varying functions of their argument. The function $1/w''$ varies most far from the beam waist ($b'' >> z_0$), where it is given approximately by

$$1/w(b''+x\alpha) \approx \frac{z_0}{w_0''(b''+x\alpha)}, \tag{2.29}$$

where z_0 is the Rayleigh range. The function $1/\Gamma$ varies most near the beam waist ($b'' \sim 0$) and

$$1/\Gamma(b''+x\alpha) \approx \frac{(b''+x\alpha)}{z_0^2} \approx \frac{x\alpha}{z_0^2}. \tag{2.30}$$

Furthermore, because the field rapidly decays in the transverse direction, it is generally not necessary to integrate equation (2.9) over the whole aperture. It is sufficient to consider the circle with a radius of $1.5w''$, into which about 99% of the total power is concentrated. In which case, from the above expressions, we have

$$1/(wb'' + x\alpha)\Big|_{x = 1.5\frac{w_0''b''}{z_0}} = \frac{z_0}{w_0''(b'' + 1.5\frac{w_0''b''}{z_0}\alpha)} = \frac{z_0}{w_0''b''}\frac{1}{(1 + 1.5\frac{w_0''}{z_0}\alpha)} \approx \frac{z_0}{w_0''b''}, \quad (2.31)$$

and

$$k\rho/2\Gamma(x\alpha)|_{\rho \le 1.5w_0} \le \frac{kx\alpha}{2z_0^2}(1.5w_0)^2 = 1.125\left(\frac{w_0}{z_0}\right)^2 kx\alpha \ll kx\alpha, \quad (2.32)$$

since the beam waist will be smaller than the Rayleigh range at optical frequencies for paraxial fields. We will thus treat the beam radius and curvature in (2.28) as constants.

Similar arguments are used to neglect the influence across the aperture of the Guoy effect (which varies most near the beam waist), because

$$\Phi''(x\alpha)|_{x \le 1.5w_0} \le \frac{1.5w_0}{z_0}\alpha \ll 1. \quad (2.33)$$

We can also relate the beam parameters of the transmitted beam to the those of the incident beam by applying the boundary condition which states that the phase must be continuous across the whole interface; that is

$$k_0[b + \theta x] - \Phi(b) + \frac{k_0\rho^2}{2\Gamma(b)} = k[b'' + \alpha x] - \Phi''(b'') + \frac{k\rho^2}{2\Gamma''(b'')}, \quad (2.34)$$

from which the following expressions are obtained:

$$\begin{aligned} b &= n_1 b'' \\ \Gamma''(b'') &= n_1 \Gamma(b) \end{aligned} \tag{2.35}$$

It also follows that, because the amplitudes of the beams are related to each other by a constant Fresnel transmission coefficient across the interface, their exponential decay rate must match; i.e

$$w''(b'') = w(b). \tag{2.36}$$

We now have a simple expression for the tilted beam to use in (2.9):

$$\boldsymbol{E}(x'', y'', z'')|_{z=0} = \frac{2\sqrt{\frac{\eta}{\pi}}}{w(b)} e^{j\Phi(b)} e^{-\left(\frac{\rho}{w(b)}\right)^2} e^{-j\left[k_0[b + x\theta] + \frac{k_0\rho^2}{2\Gamma(b)}\right]} (\hat{x}\cos\zeta + \hat{y}\sin\zeta). \tag{2.37}$$

Again, since the field is cosine symmetric about the $\phi = 0$ axis, then all hybrid modes will be excited and only the TM and TE modes are polarization sensitive. Thus, the launching efficiency for Gaussian beams is given by the expression

$$P_p = \frac{1}{2}\left(\frac{\varepsilon_1}{\mu}\right)\frac{4\eta a^4}{\pi w^2 \psi_p}\left|\int_0^{2\pi}\int_0^{d/a} f_l(R) e^{-a^2R^2\left(\frac{1}{w^2} + \frac{jk_0}{2\Gamma}\right)} e^{-j\,\Delta R\cos\varphi}\cos(l \mp 1)\varphi R dR d\varphi\right|^2, \quad \text{hybrid} \tag{2.38}$$

and

$$P_p = \frac{1}{2}\left(\frac{\varepsilon_1}{\mu}\right)\frac{4\eta a^4}{\pi w^2 \psi_p}\left|\int_0^{2\pi}\int_0^{d/a} f_0(R)e^{-a^2R^2\left(\frac{1}{w^2}+\frac{jk_0}{2\Gamma}\right)}e^{-j\,\Delta R\cos\varphi}\cos\varphi R dR d\varphi\right|^2 , \qquad \text{TM + TE}$$

(2.39)

where we have omitted the argument of the beam parameters, b. Equation (2.39) is identical to (2.38) with l=0. The expansion in terms of Bessel function and the orthogonality property, given by equation (2.19) and (2.20) respectively, is then used to obtain

$$P_p = \frac{8}{\xi}\left|\frac{aU_pG}{wV}\right|^2 . \tag{2.40}$$

where

$$G = \int_0^D f_l(R)e^{-a^2R^2\left(\frac{1}{w^2}+\frac{jk_0}{2\Gamma}\right)}J_{l\mp1}(R\,\Delta)RdR . \tag{2.41}$$

2.2.2 Modeling offset Gaussian beams

Generally, the incident beam will not be exactly concentric with axis of the optical fiber (fig.2.5) and thus the effect of an offset beam on the modal launching efficiency needs to be evaluated. Consider a Gaussian beam whose propagation axis is parallel to the z axis, but crosses the fiber face at a point (ρ_0,φ_0) in cylindrical coordinates:

$$E(x', y', z')|_{z=0} = \frac{2\sqrt{\frac{\eta}{\pi}}}{w(b)}e^{j\Phi(b)}e^{-\left(\frac{\rho'}{w(b)}\right)^2}e^{-j\left[k_0 b+\frac{k_0\rho'^2}{2\Gamma(b)}\right]}(\hat{x}\cos\zeta+\hat{y}\sin\zeta), \tag{2.42}$$

where ρ' relates to ρ by the Law of Cosines

$$\rho'^2 = \rho^2 + \rho_0^2 - 2\rho\rho_0\cos(\varphi - \varphi_0). \tag{2.43}$$

Equation (2.42) is cosine symmetric relative to the $\varphi=\varphi_0$ axis.

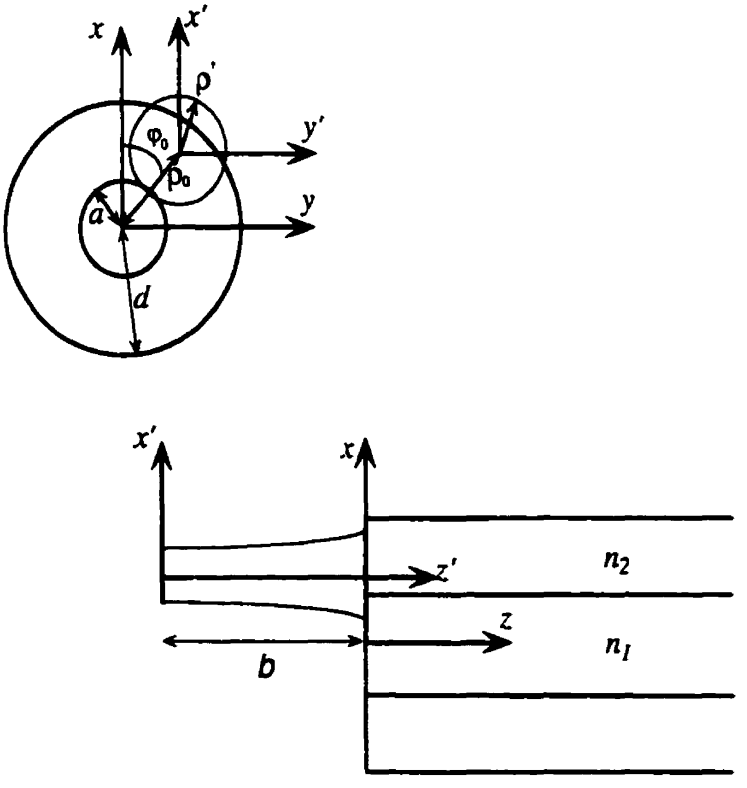

FIGURE 2.5 Geometric configuration for an offset Gaussian beam

The launching efficiency of the Gaussian beam into the hybrid modes becomes

$$P_p = \frac{2a^4\eta\varepsilon_1}{\pi w^2\mu_0\Psi_p}\left|\int_0^{2\pi}\int_0^D RdRd\varphi f_1(R)e^{-a^2[R^2+R_0^2-2RR_0\cos(\varphi-\varphi_0)][1/w^2+jk_0/2\Gamma]}Z(\varphi,\zeta)\right|^2, \tag{2.44}$$

where $R_0=\rho_0/a$, and $Z(\varphi,\zeta)$ is given by

$$Z(\varphi,\zeta)=\begin{bmatrix}\pm\sin(l\mp1)\varphi\cos\zeta+\cos(l\mp1)\varphi\sin\zeta\\ or\\ \pm\cos(l\mp1)\varphi\cos\zeta-\sin(l\mp1)\varphi\sin\zeta\end{bmatrix}. \tag{2.45}$$

Using the well known addition formulas for trigonometric functions, we find

$$\begin{aligned}Z(\varphi,\zeta)&=\sin(\zeta\pm(l\mp1)\varphi)=\sin[\zeta\pm(l\mp1)\varphi_0\pm(l\mp1)(\varphi-\varphi_0)]\\&=\sin(\zeta\pm(l\mp1)\varphi_0)\cos(l\mp1)(\varphi-\varphi_0)\pm\cos(\zeta\pm(l\mp1)\varphi_0)\sin(l\mp1)(\varphi-\varphi_0)\end{aligned}, \tag{2.46}$$

or

$$\begin{aligned}Z(\varphi,\zeta)&=\pm\cos(\zeta\pm(l\mp1)\varphi)=\cos[\zeta\pm(l\mp1)\varphi_0\pm(l\mp1)(\varphi-\varphi_0)]\\&=\pm\cos(\zeta\pm(l\mp1)\varphi_0)\cos(l\mp1)(\varphi-\varphi_0)-\sin(\zeta\pm(l\mp1)\varphi_0)\sin(l\mp1)(\varphi-\varphi_0)\end{aligned}. \tag{2.47}$$

Inserting (2.46) and (2.47) into (2.44), and using the orthogonality properties of trigonometric functions, we find

$$P_p=\left(\frac{\varepsilon_1}{\mu_0}\right)\frac{2a^4\eta}{\pi w^2\psi_p}\times$$
$$\left|\int_0^{2\pi}\int_0^{D}RdRd\varphi f_l(R)e^{-a^2[R^2+R_0^2-2RR_0\cos(\varphi-\varphi_0)][1/w^2+jk_0/2\Gamma]}\cos(l\mp1)(\varphi-\varphi_0)\right|^2 X(\zeta,\varphi_0), \tag{2.48}$$

where

$$X(\zeta,\varphi_0)=\begin{bmatrix}\sin^2(\zeta\pm(l\mp1)\varphi_0)\\ or\\ \cos^2(\zeta\pm(l\mp1)\varphi_0)\end{bmatrix}. \tag{2.49}$$

Since both representations of the degenerate hybrid modes are equivalent, both contribute to the launching efficiency and

$$P_p = \left(\frac{\varepsilon_1}{\mu_0}\right)\frac{2a^4\eta}{\pi w^2} \times \quad \text{hybrid}$$
$$\left|\int_0^{2\pi}\int_0^D RdRd\varphi f_l(R) e^{-a^2[R^2+R_0^2-2RR_0\cos(\varphi-\varphi_0)][1/w^2+jk_0/2\Gamma]}\cos(l\mp 1)(\varphi-\varphi_0)\right|^2 ,$$

(2.50)

which is, as in the case of tilted beams, independant of polarization. Similarly, one finds for the TM and TE modes,

$$P_p = \left(\frac{\varepsilon_1}{\mu_0}\right)\frac{2a^4\eta}{\pi w^2} \times \quad \text{TM}$$
$$\left|\int_0^{2\pi}\int_0^D RdRd\varphi f_0(R) e^{-a^2[R^2+R_0^2-2RR_0\cos(\varphi-\varphi_0)][1/w^2+jk_0/2\Gamma]}\cos(\varphi-\varphi_0)\right|^2 \cos^2(\varphi_0-\zeta) ,$$

(2.51)

and

$$P_p = \left(\frac{\varepsilon_1}{\mu_0}\right)\frac{2a^4\eta}{\pi w^2} \times \quad \text{TE}$$
$$\left|\int_0^{2\pi}\int_0^D RdRd\varphi f_0(R) e^{-a^2[R^2+R_0^2-2RR_0\cos(\varphi-\varphi_0)][1/w^2+jk_0/2\Gamma]}\cos(\varphi-\varphi_0)\right|^2 \sin^2(\varphi_0-\zeta) .$$

(2.52)

The TM mode can only be excited if the direction of the offset is parallel to the polarization of the beam, while for TE modes the offset must be perpendicular. However,

the sum of their respective launching efficiency is independant of polarization, and is given by

$$P_p = \left(\frac{\varepsilon_1}{\mu_0}\right)\frac{2a^4\eta}{\pi w^2} \times \qquad \text{TE} + \text{TM}$$

$$\left|\int_0^{2\pi}\int_0^D RdRd\varphi f_0(R) e^{-a^2[R^2 + R_0^2 - 2RR_0\cos(\varphi-\varphi_0)][1/w^2 + jk_0/2\Gamma]}\cos(\varphi-\varphi_0)\right|^2 , \tag{2.53}$$

which is identical to (2.50) with l=0.

Using a integral representation of the modified Bessel function of the first kind,

$$I_n(z) = \frac{1}{\pi}\int_0^{\pi} e^{z\cos t}\cos(nt)dt. \tag{2.54}$$

(2.50) becomes

$$P_p = \frac{8}{\xi}\left|\frac{aU_pH}{wV}\right|^2, \tag{2.55}$$

where

$$H = e^{-\left(\frac{aR_0}{w}\right)^2}\int_0^D f_l(R) e^{-a^2R^2\left(\frac{1}{w^2}+\frac{jk_0}{2\Gamma}\right)} I_{l\mp1}\left[2a^2RR_0\left(\frac{1}{w^2}+\frac{jk_0}{2\Gamma}\right)\right]RdR. \tag{2.56}$$

In chapter 3, we will need to consider the case where there is also a small tilt, θ, in the same plane as the offset. In this case, the expression for the launching efficiencies retain their symmetry relative to the φ=φ_0 axis and it can be shown that

$$P_p = \frac{8}{\xi}\left|\frac{aU_pL}{wV}\right|^2, \tag{2.57}$$

where,

$$L = e^{-\left(\frac{aR_0}{w}\right)^2}\int_0^D f_l(R)e^{-a^2R^2\left(\frac{1}{w^2}+\frac{jk_0}{2\Gamma}\right)} I_{l\mp1}\left[2a^2RR_0\left(\frac{1}{w^2}+\frac{jk_0}{2\Gamma}-\frac{jk_0\theta}{2aR_0}\right)\right]RdR. \tag{2.58}$$

2.3 General comments

Equations (2.23), (2.41), (2.56) and (2.58) share some common properties. For normal incidence and no offset, the Bessel and modified Bessel function of the first kind in the integrand is null unless $l \mp 1 = 0$. Thus, for normal incidence and no offset, only HE_{1m} modes can be stimulated in both the plane wave and the Gaussian beam case. Other modes are excited when the incident beam is offset or inclined.

As discussed in appendix A, all the modes are degenerate, each sharing the same eigenvalue U_p with one or more modes: TM_{0m} and TE_{0m} are degenerate with HE_{2m}, and the same is true between EH_{lm} and $HE_{(l+2)m}$ modes. Furthermore, inspection of (2.23), (2.41) , (2.56) and (2.58) reveals that degenerate modes also share the same expressions (the order of the Bessel functions are the same) for the launching efficiency. Thus, both facts imply that the sum of the launching efficiencies into the TM and TE modes is equal to that of the HE_{2m} mode. The same is true between EH_{lm} and $HE_{(l+2)m}$ modes. Of course, this means that the launching efficiency into modes other than HE_{1m} can never exceed 50% (Miyagi et al. 1975), and that only the HE modes need be calculated.

2.4 Higher order beams

The Gaussian beam is only the lowest-order solution of a family of solutions satisfying the free space paraxial equation. These higher-order solutions can take the form of Hermite-Gaussian functions in cartesian coordinates or Laguerre-Gaussian functions in cylindrical coordinates. Both set of solutions are equally general and form a complete basis for the expansion of arbitrary optical beams (Siegman 1986). The Laguerre-Gaussian expansion is convenient for problems with a high degree of cylindrical symmetry and would be adequate to model the output of VCSELs. In recent work, the modes of a cylindrical optical fiber were expanded in terms of the Laguerre-Gaussian functions to calculate the near-field and far-field output from the fiber (Sutherland 1997).

The Laguerre-Gaussian family of solutions are given explicitly by

$$E_{lms} = \frac{A_{lm}}{w}\left(\frac{\rho\sqrt{2}}{w}\right)^{l} L_m^{l}\left(\frac{2\rho^2}{w^2}\right) e^{\left[-j(kz - s\varphi - (l+2m+1)\Phi) - \rho^2\left(\frac{1}{w^2} + \frac{jk}{2\Gamma}\right)\right]} . \tag{2.59}$$

A_{lm} is a normalization constant determined by the condition that the power propagated is unity. L^{l}_{m} is the generalized Laguerre polynomial and the indices l, m and s are positive integers. The parameters w, Γ and Φ are identical to those given by (B-13). The Gaussian beam can be retrieved by inserting l=m=0.

Assuming the same approximations as for the zero order Gaussian beam, each source mode given by (2.57) can be substituted into equation (2.9) to obtain the coupling efficiency to each receiving mode. Thus if the source has q modes and the receiving fiber has r modes, then there are $q \times r$ coupling coefficients to compute.

Chapter 3

Alignment requirements for optimal coupling between an 8x8 VCSEL array and an 8x8 fiber array

3.1 An interconnect without optical elements

The simplest form of 2-dimensional interconnect between a set of optical sources and a set of identical receiving fibers is portrayed by figure 3.1. Consider a square array of VCSELs, each emitting a beam to a single corresponding fiber without the presence of any optical element to steer or focus the beams. The electrical contacts to the VCSEL array are not included in the illustration. Both the vertical and horizontal spacing between channels are assumed to be 250 μm unless stated otherwise.

In the analysis which follows, we will consider beam characteristics appropriate for typical VCSEL structures. Namely, we assume the driving current is sufficient to induce lasing, but low enough not to stimulate Laguerre-Gaussian modes beyond the fundamental. In which case, the resulting Gaussian beam typically has a far-field divergence angle, $2\theta_{99\%}$, of approximately 14°, defining a cone into which is propagating 99% of the total power. This angle is directly related to the beam waist by

$$\theta_{99\%} = \frac{1.5\lambda_0}{\pi w_0}. \tag{3.1}$$

We will assume a wavelength of 0.845 μm, which gives a beam waist of approximately $w_0 = 3.3$ μm.

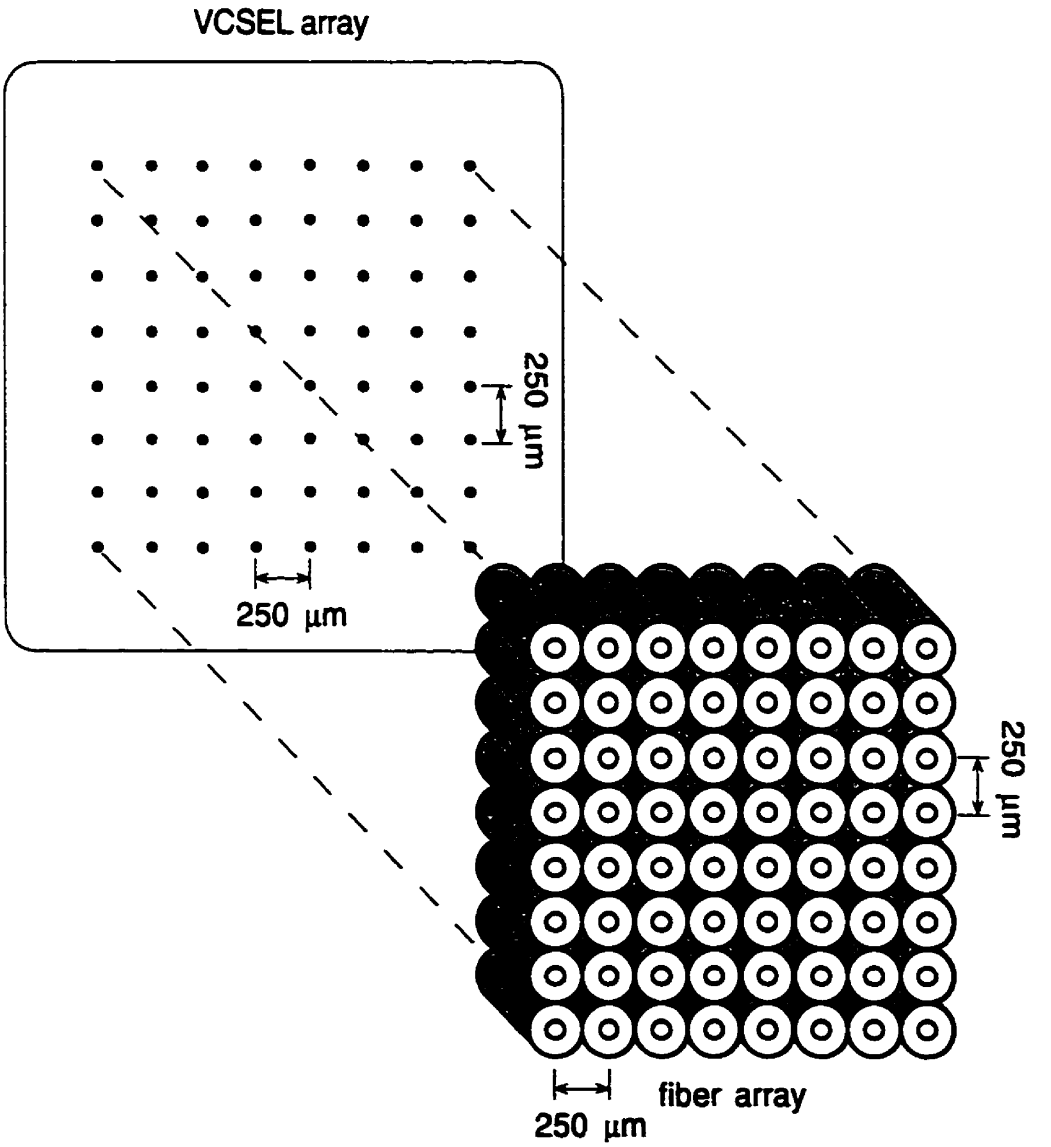

FIGURE 3.1 Simple 2-dimensional interconnect.

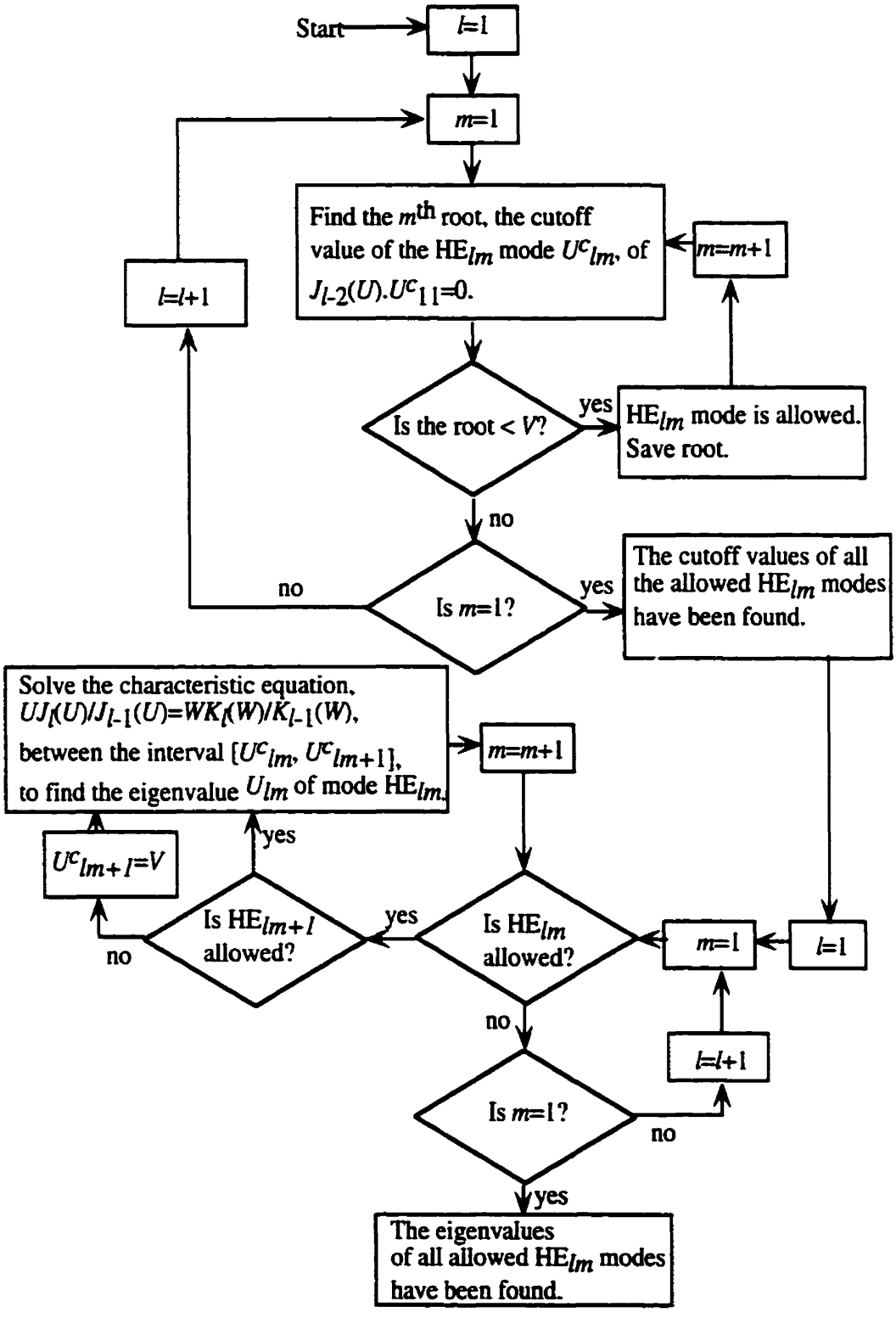

FIGURE 3.2 Flowchart of the proposed algorithm to find the allowed HE_{lm} modes and the eigenvalues U_{lm}.

3.2 Numerical analysis

All calculations have been done using Mathematica, a trademark of Wolfram Research, on a G3 Power Macintosh.

3.2.1 Optical fiber mode solutions

A variety of different fiber parameters will be used in order to investigate their effect on launching efficiency. Specifically, we shall study single mode fiber and multimode fiber with a core radius of up to 50 μm. In each case, we need to determine the allowed HE modes and solve the characteristic equation (A-27) to find the eigenvalue U for each of these modes. Using equation (A.31), an approximate solution to the eigenvalues, is not adequate for the needs of the present analysis. To obtain the total launching efficiency, we must sum the contributions of all modes including higher order modes that have eigenvalues progressively closer to cutoff.Because (A.31) is not a good approximation of the eigenvalues near cutoff, the launching efficiency of the beam into these higher order modes becomes inaccurate and may create a significant error in the sum. A flow chart of the proposed algorithm is illustrated in figure 3.2, and an outline of its implementation using Mathematica will now be described.

First, which modes are guided must be determined. As discussed in appendix A, a mode can exist for every root of $J_{l-2}(U)$, U^c_{lm}, smaller than V. For each l, there are t roots (m = 1, 2, ..., t) which satisfy this condition, where t is a decreasing function of l. The maximum value of l corresponds to that beyond which no more roots can satisfy this condition. A list of these roots can be generated with the function BesselJZeros included

in the NumericalMath'BesselZeros' package included with Mathematica and a simple algorithm can extract the roots that are smaller than V. The resulting list is composed of a set of sublists, one sublist for each allowed value of l, each of which is composed of the set of t eigenvalues. This procedure was implemented by the function CutOff[V], defined in our package HEmodesolver.m, listed in appendix C.

Once determined, the characteristic equation is solved using the function FindRoot for each allowed mode. A starting value is needed to initiate the algorithm and FindRoot uses Newton's Method to find one possible solution to the equation. Thus for a given l, FindRoot must be used t times to obtain a complete set of solutions to the characteristic equation. Since FindRoot will output the first solution it finds, one must be careful to correctly partition the problem. Since it is known that for a fixed l, there exists one and only one solution of the characteristic equation within the interval $[U^c_{lm}, U^c_{lm+1}]$ (as can be seen from figure A.1), FindRoot can be constrained to find a solution within such an interval, using the list of cutoff values obtained previously, and stopping the algorithm when the solution is found (or until it reaches a point outside the defined interval). To make sure that the algorithm stays within the required interval, the option DampingFactor, which specifies the size of the steps used in Newton's method, can be set. The option MaxIterations can also be set to allow the algorithm to converge for larger values of DampingFactor. The procedure is then repeated for each interval. The procedure is implemented by the function HeModeSolve[V], again defined in HEmodesolver.m.

Table I summarizes the fiber parameters that will be used in the following analysis and specifies the number of HE modes in each case. The chosen value of the numerical

aperture, NA=0.2, corresponds to an acceptance angle of $\theta_a = \sin^{-1}NA$ =11.54 degrees, which is more than sufficiently large considering the divergence of the beam ($\theta_{99\%}$=7 degrees).

TABLE I. Optical fiber HE modes solutions as a function of core radius a (λ_0=0.845 μm).

NA =0.2		
a (μm)	V	# modes
1.6	2.380	1
5	7.440	9
10	14.87	32
15	22.31	68
20	29.74	118
25	37.18	182
50	74.36	707

3.2.2 Launching efficiency

Once the eigenvalue of allowed HE mode has been obtained for a given V, it is substituted (along with all the other appropriate parameters, such as the correct beam waist, wavelength,etc.)into one of the equations derived in chapter 2, which is then numerically integrated to obtain the launching efficiency of the beam into that mode. Numerical solutions to the modal launching efficiencies were obtained with the function NIntegrate, leaving the algorithm to the Gauss-Kronrod method of integration. Most the options for this function were left at the default settingwith a few exceptions. MaxRecursion needed to be increased to allow the algorithm to converge for high order modes. Furthemore, since total efficiency cannot be higher than 1 and since there will be at most about 707 excited

HE modes, AccuracyGoal and PrecisionGoal was set to at most 6 digits to increase the speed of the algorithm, and is more than sufficient to get a good estimate of the efficiency.

To determine the total efficiency we must sum the contribution of all modes present. But, as explained in chapter 2, only the contributions of the HE_{lm} modes are needed For each HE_{lm} mode with $l > 2$, there is a EH mode which has the same launching efficiency. For each excited HE_{2m} mode there is an equal contribution from TE and TM modes. Thus, simply doubling the contributions from all HE_{lm} modes with $l > 1$ will produce the correct value of the total launching efficiency. We will also include a 4% loss due to Fresnel reflection in the plots presented in this chapter.

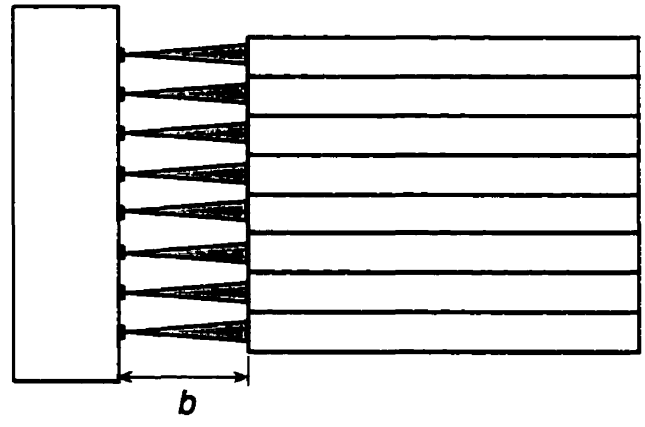

FIGURE 3.3 Spacing between the arrays.

3.3 Effects of misalignment on insertion losses

Misalignment can occur in all six degrees of freedom. Because of the symmetrical nature of the interconnect, we only need to study the effect of four: distance between the arrays along the axis, offset, roll, and tilt. The geometric configuration associated with each type of misalignment is respectively illustrated in figure 3.3 to 3.6.

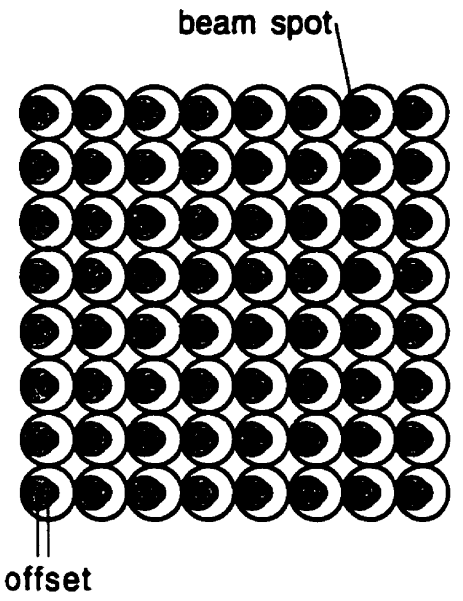

FIGURE 3.4 Misalignment due to offset.

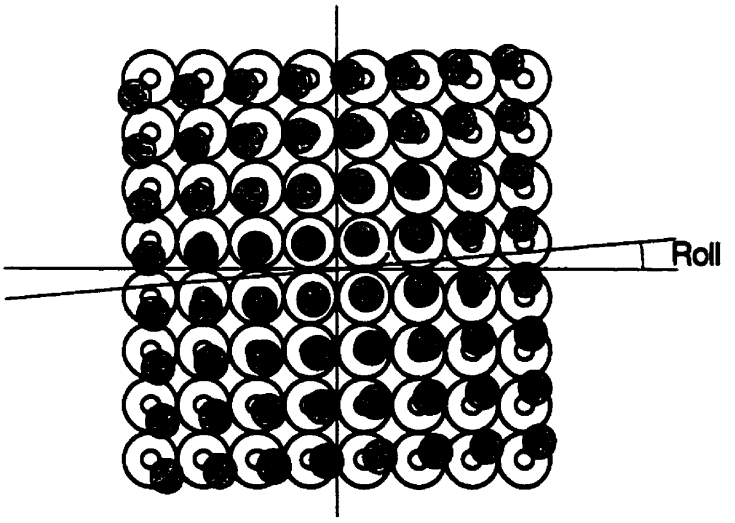

FIGURE 3.5 Misalignment due to roll.

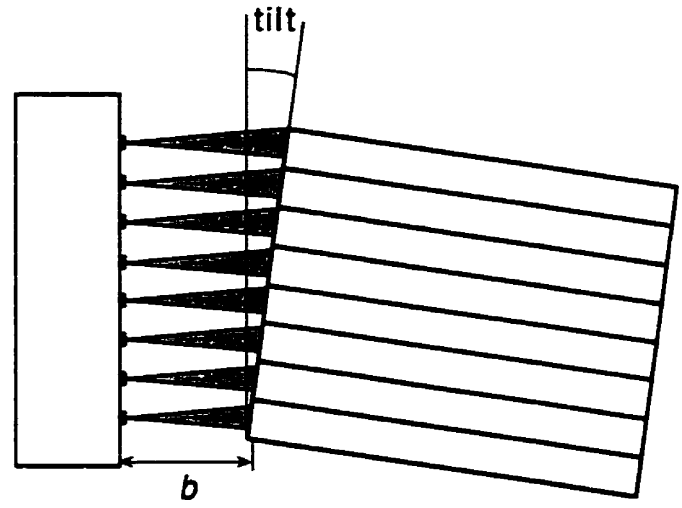

FIGURE 3.6 Misalignment due to tilt.

3.3.1 Spacing between source array and fiber array

The equations derived depend explicitely on the precise value of the beam width and radius of curvature, which in turn are functions of the distance from the beam waist (located at the source when no other optical elements are involved). Both parameters, as functions of distance, are shown respectively in figure 3.7 and 3.8, for the values of wave-length and beam waist chosen for this analysis.

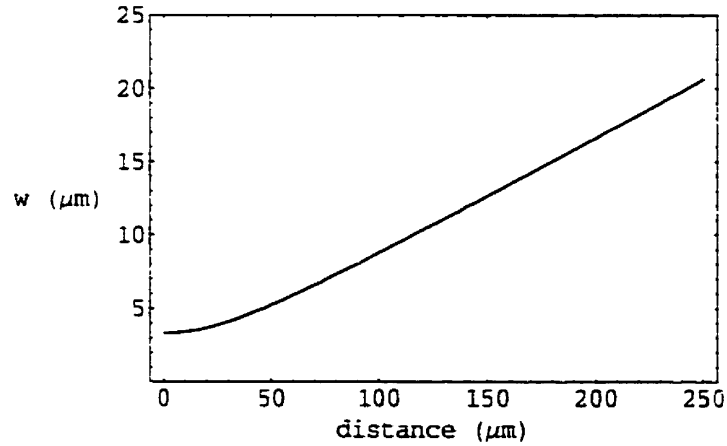

FIGURE 3.7 Beam width versus distance (λ_0=0.845 μm,w_0=3.3 μm).

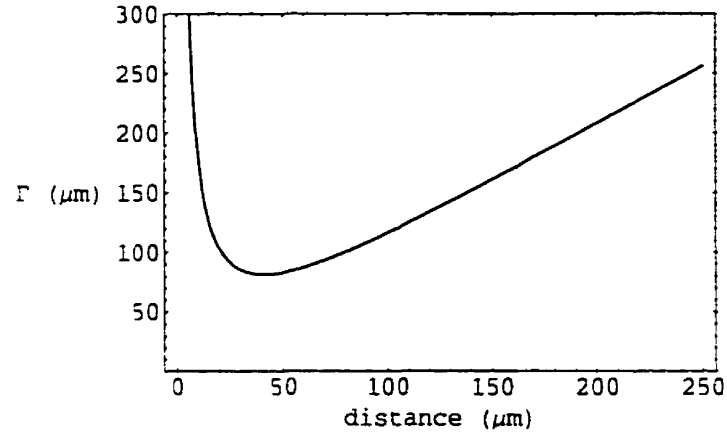

FIGURE 3.8 Wavefront radius of curvature versus distance (λ_0=0.845 μm,w_0=3.3 μm).

Let us first consider arrays which are separated in space but are otherwise perfectly aligned, without tilt, roll, or offset. Shown in figure 3.9, is the insertion loss as a function of this distance for each core radius considered.The insertion loss is obtained by converting the total launching efficiency, which has a value between 0 and 1, into decibel units (dB). From figure 3.3, it is clear that in this case the results presented here apply equally for all channels across the array, since the fibers all have identical positions relative to their respective VCSEL.

The total launching efficiency is maximal when the fiber face is located very near the source, and then decreases with distance. For single-mode fiber (a =1.6 μm), the maximum launching efficiency is ~ 71 % (-1.48 dB loss). As the core radius increases, this maximum rapidly reaches ~96 % (- 0.18 dB loss) , which represents a coupling efficiency of 100% minus the 4% Fresnel reflection.

Also shown, in dashed lines, are the -1 dB (~78 %) and -3 dB (50 %) levels. In this analysis, we consider insertion losses of greater magnitude than -3 dB as unacceptable, and corresponds roughly to the loss which occurs when coupling with fiber image guides (as discussed in chapter 1). Because image guides compete with and are easier to align than the fiber arrays considered here, we must demonstate the conditions in which fiber arrays can not only match but even exceed image guides in performance. To fufill this objective, we determine the tolerances necessary for -1 dB insertion loss due to alignment.

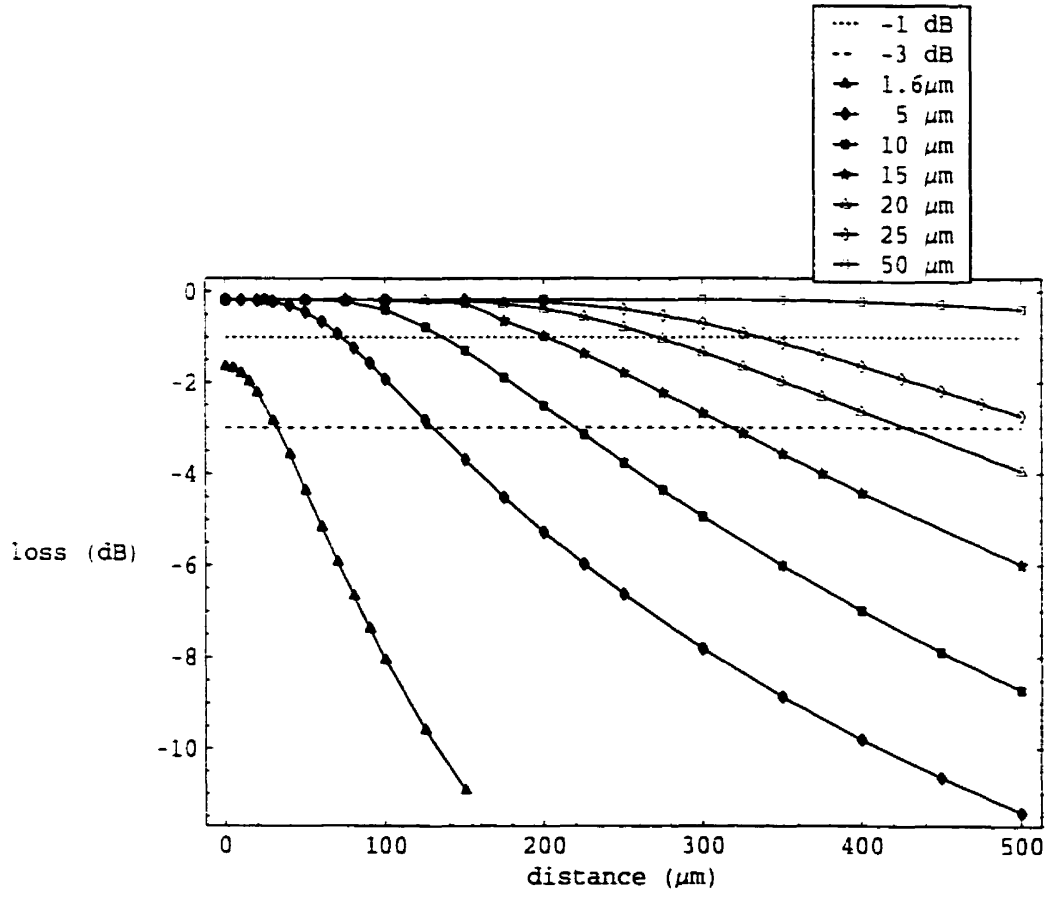

FIGURE 3.9 Insertion loss as a function of distance and core radius, without misalignment.

For single-mode fiber, -1 dB performance is not possible because the radius of the beam is simply too large, even at its narrowest point, and much of the power enters the cladding instead of the core. Beyond a distance of ~30 μm, the efficiency of the connection falls below -3 dB point. But as the core radius increases, so do the -3dB and -1 dB alignment tolerances (figure 3.10). When a = 25 μm, these alignment requirements are 510 μm and 320 μm, respectively. If the core radius is instead 50 μm, the launching efficiency remains above -1 dB over the range of 500 μm considered here.

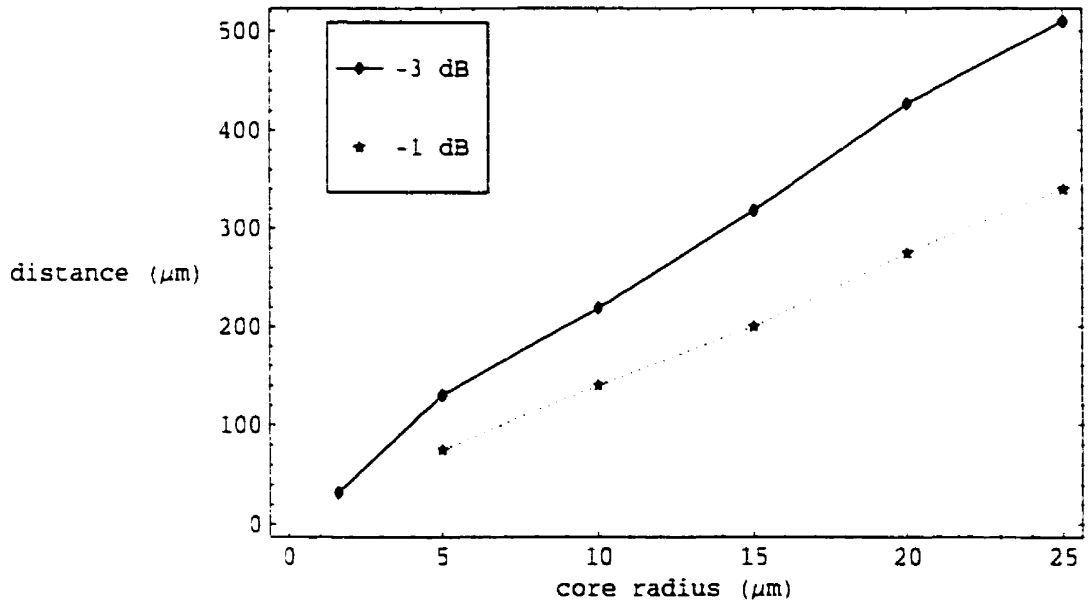

FIGURE 3.10 Tolerated distance between source array and fiber array as a function of the core radius and. power requirements.

Clearly, the spacing between the source array and the fiber array is an important design parameter which will determine the choice of an appropriate core size. If, for example and for various reasons, the array can be positioned no closer than 100 μm from the VCSELs, but no further than 250 μm, then the interconnect designer should consider fibers of 20 μm radius or more.

3.3.2 Offset

Let us now consider misalignment in the form of a lateral displacement (figure 3.4). As in the case of an axial displacement, the launching efficiency is identical in all channels.

Figures 3.11 to 3.17 show the increase of loss with offset for each core radius considered. We include in these plots data taken at different values of VCSEL-fiber spacing to observe its effects on the lateral alignment tolerances. In general, a small VCSEL-fiber distance is more tolerant to offset. When the array is located very near the source, the curves generally form a plateau, followed by an abrupt drop in efficiency for values of the offset which are near the core radius. The single-mode fiber case is an exception to this general rule and has no plateau. At larger distances, the plateau region are reduced in range (or disappears completely) and the drop becomes more gradual, the curves intersecting at the low decibel range.

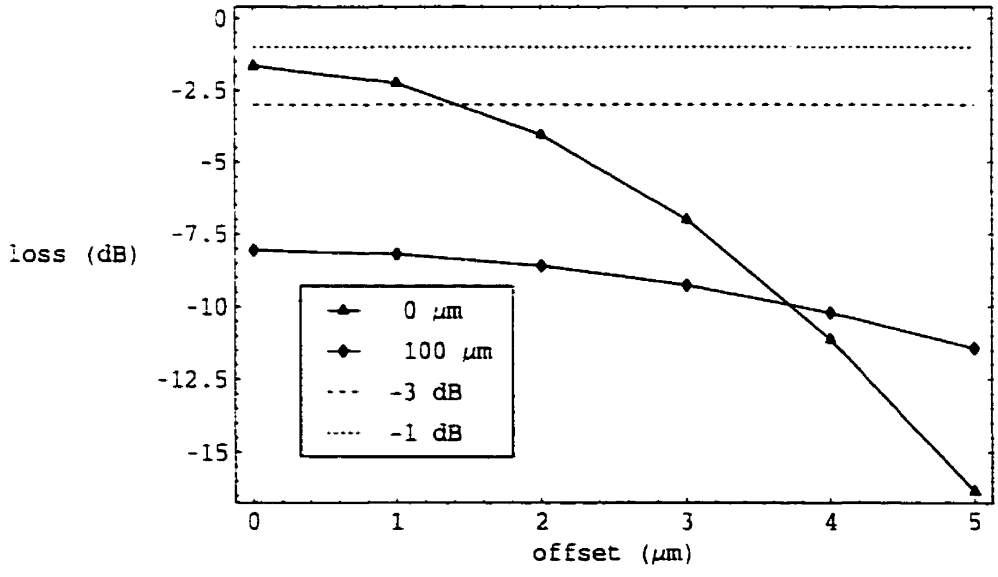

FIGURE 3.11 Insertion loss as a function of offset and distance. The core radius is 1.6 μm.

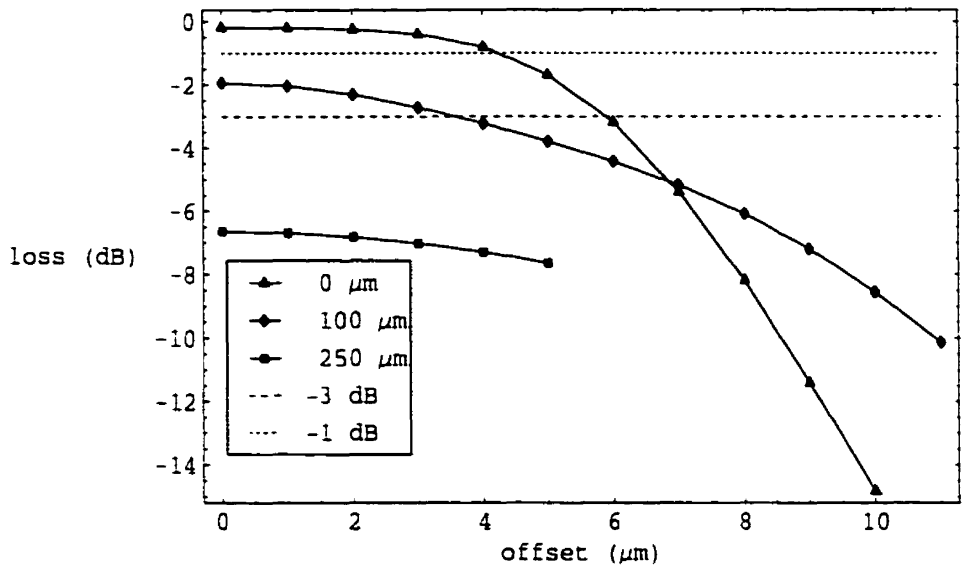

FIGURE 3.12 Insertion loss as a function of offset and distance. The core radius is 5 μm.

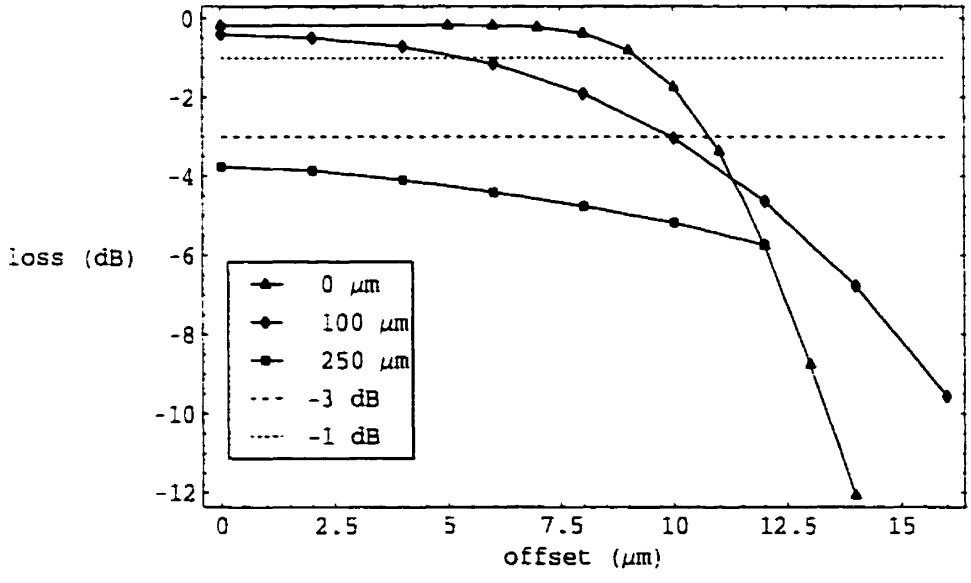

FIGURE 3.13 Insertion loss as a function of offset and distance. The core radius is 10 μm.

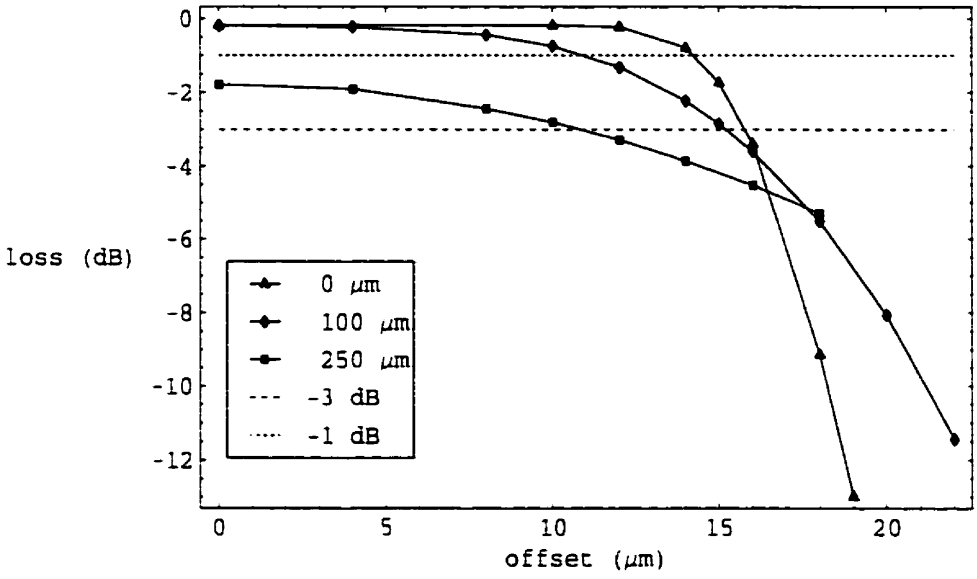

FIGURE 3.14 Insertion loss as a function of offset and distance. The core radius is 15 μm.

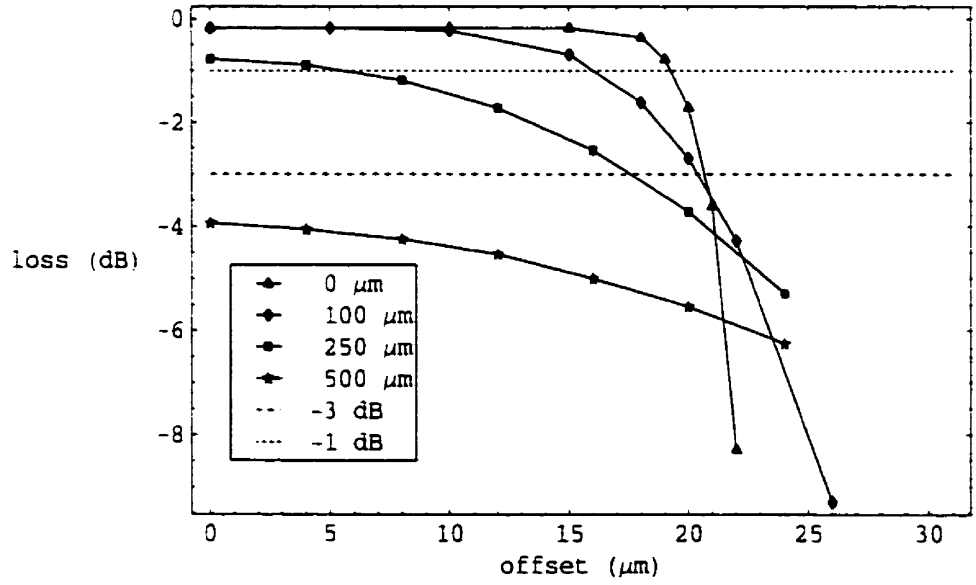

FIGURE 3.15 Insertion loss as a function of offset and distance. The core radius is 20 μm.

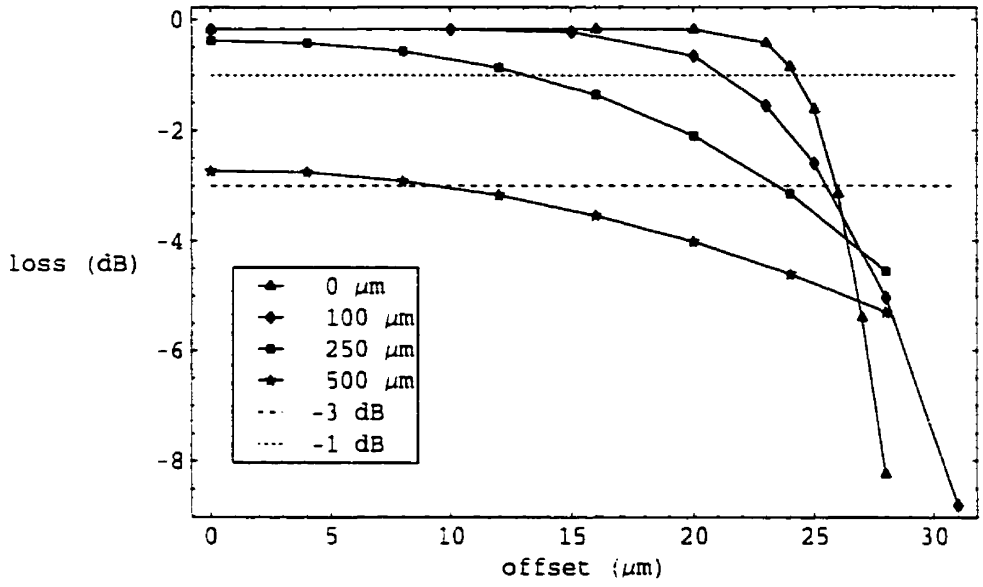

FIGURE 3.16 Insertion loss as a function of offset and distance. The core radius is 25 μm.

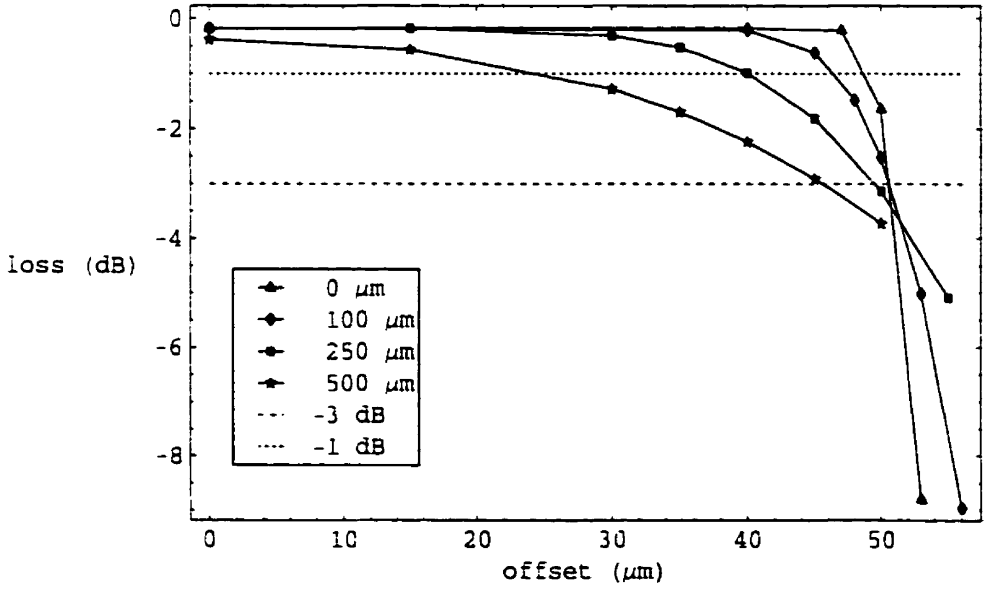

FIGURE 3.17 Insertion loss as a function of offset and distance. The core radius is 50 μm.

Conceptually, we can understand these facts on the basis that as long as the beam enters the fiber through the core, the efficiency remains high with little variation. As the beam begins to enter the cladding due to offset, the efficiency experiences a drop, and becomes low when the beam completely exits the core. At larger distances, the beam has a larger spread, thus less offset is needed for the efficiency to drop, but more offset is needed for the beam to exit the core completely. Since the beam waist is twice as large as the radius of single-mode fiber, significant loss occurs immediately with offset and thus there is no plateau.

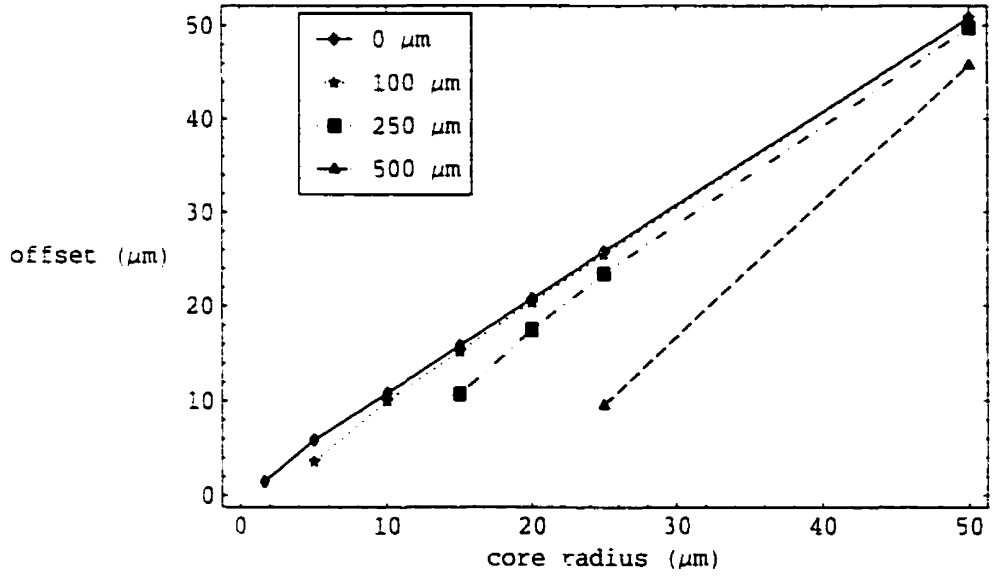

FIGURE 3.18 Offset alignment tolerances (-3 dB) as a function of offset and distance.

Figure 3.18 and 3.19 show respectively the -3 dB and -1 dB alignment tolerances to offset. The alignment tolerances are in both cases generally linear with core radius. In these plots we also see quite clearly the loss of tolerance that occurs with VCSEL-fiber distance. For example, if a = 25 μm then the -1 dB lateral alignment requirements are

respectively 24 μm, 21 μm, and 13 μm at a distance of 0μm, 100 μm, and 250 μm (-1 dB performance is not possible at 500 μm for this core size). As discussed in chapter 1, it is at present possible to construct with the rod in tube method an array that have individual 25 μm cores that deviate no more than 5 μm from their ideal position. This leaves respectively a tolerance budget for packaging of 19 μm, 16 μm, and 7 μm.

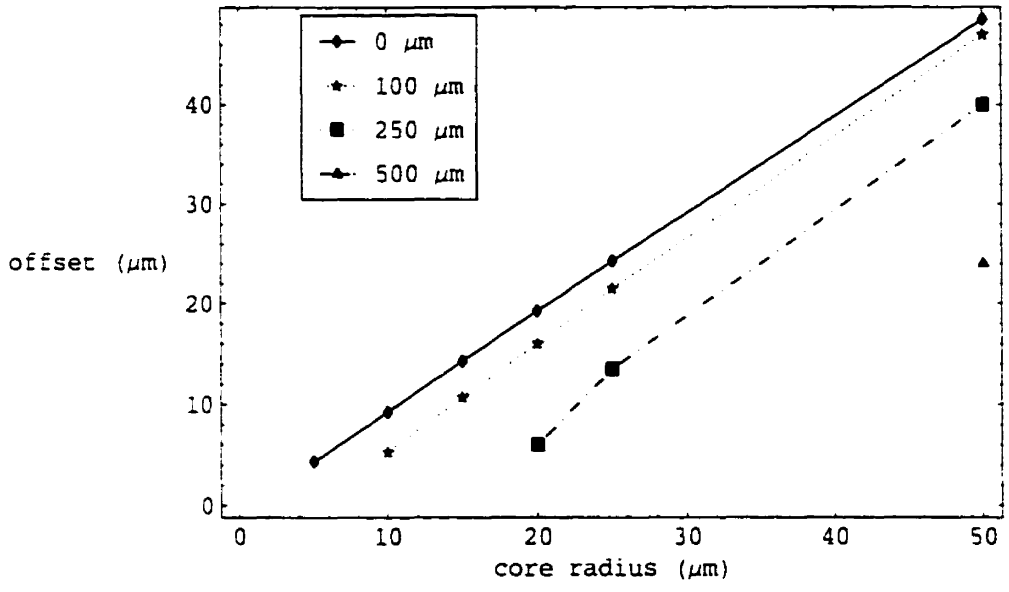

FIGURE 3.19 Offset alignment tolerances (-1 dB) as a function of offset and distance.

3.3.3 Roll

We have so far considered translational degrees of freedom. We will now consider rotations. Under their influence, the launching efficiency is no longer uniform across the array. When roll misalignment is present, it creates an offset in each fiber which increases with the distance *S* from the center of rotation (figure 3.5). To obtain an alignment tolerance to roll for the array, we must study its effects on the furthest channels relative to the rotation axis, in other words, the channels at the corners of the square array.

From the Cosine Law of trigonometry, the following expression relating channel offset and roll, as a function of S, is derived,

$$O = S\sqrt{2(1-\cos\Theta)}, \tag{3.2}$$

where O is the value of the offset induced by the roll angle Θ. This expression is very useful since it provides a means by which we can scale our previous results for lateral (uniform) misalignment into results for roll.

When considering an 8x8 250 μm pitch array with the rotation axis located at the center, then S = 1237 μm for the corner channels. In that case, figures 3.11 to 3.17 are changed in scale to produces figures 3.20 and 3.26, respectively, which thus show the same basic patterns for lateral displacements: plateaus of increasing length with core size, and and a loss of tolerance at larger spacings.

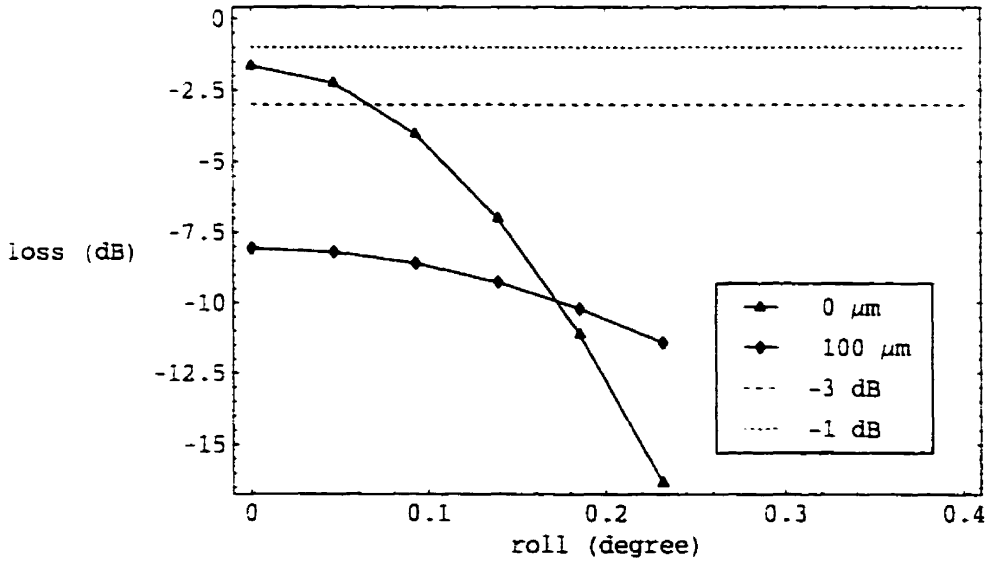

FIGURE 3.20 Insertion loss as a function of roll and distance. The core radius is 1.6 μm.

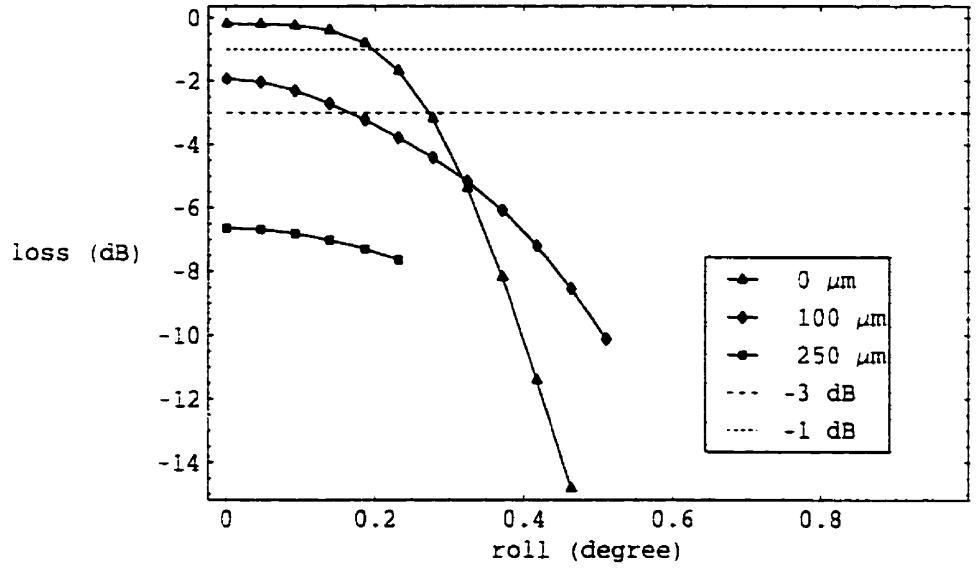

FIGURE 3.21nsertion loss as a function of roll and distance. The core radius is 5 μm.

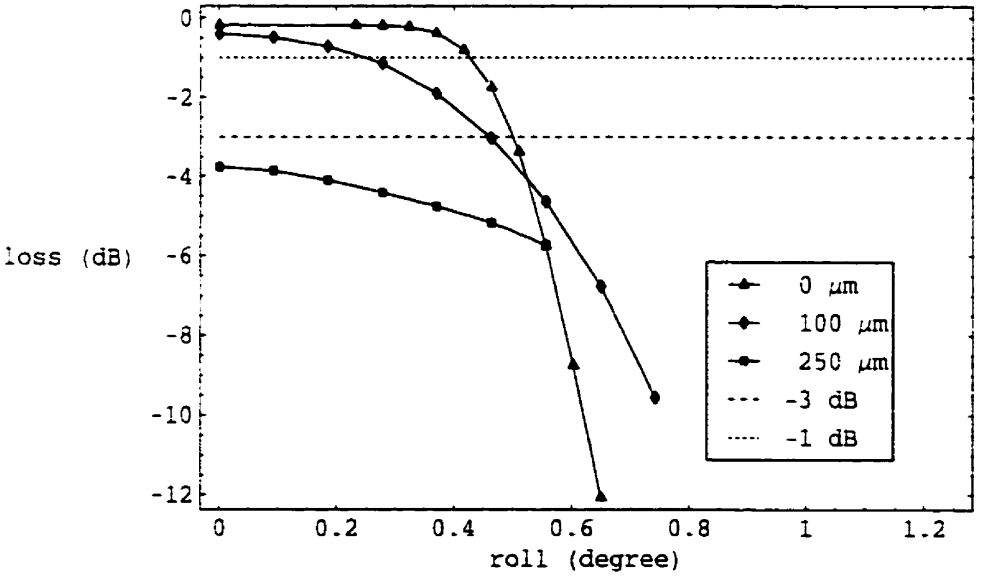

FIGURE 3.22 Insertion loss as a function of roll and distance. The core radius is 10 μm.

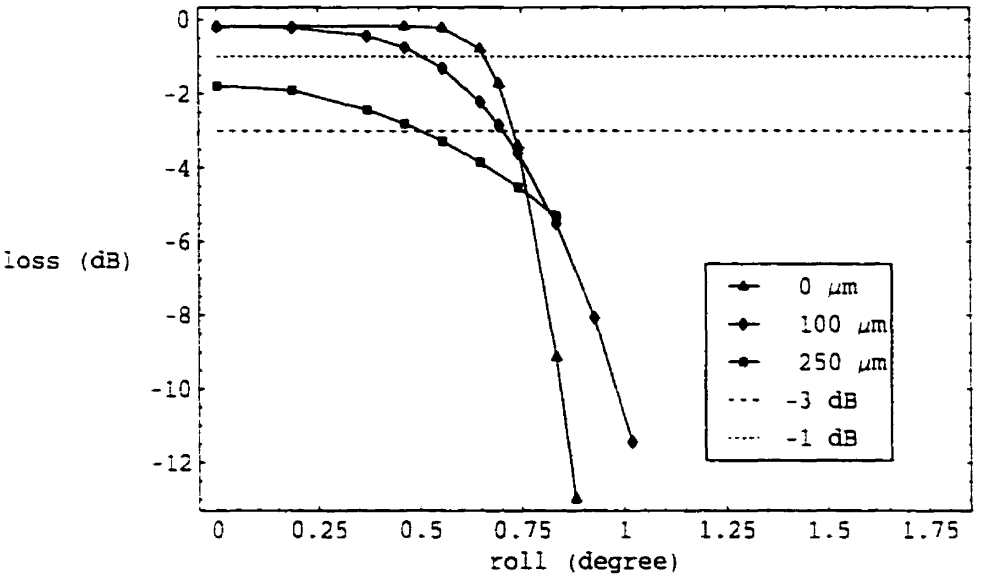

FIGURE 3.23 Insertion loss as a function of roll and distance. The core radius is 15 μm.

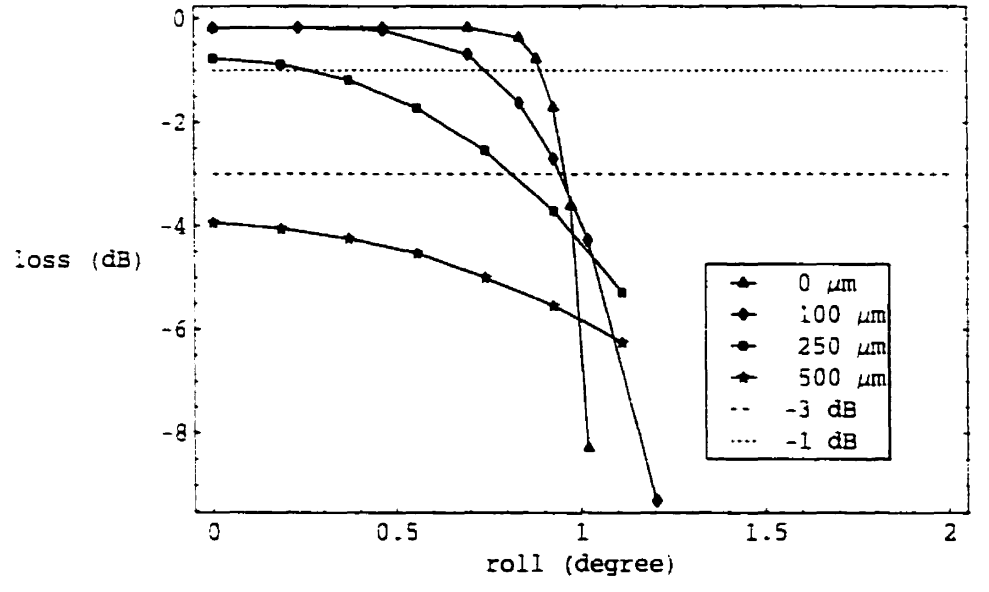

FIGURE 3.24 Insertion loss as a function of roll and distance. The core radius is 20 μm.

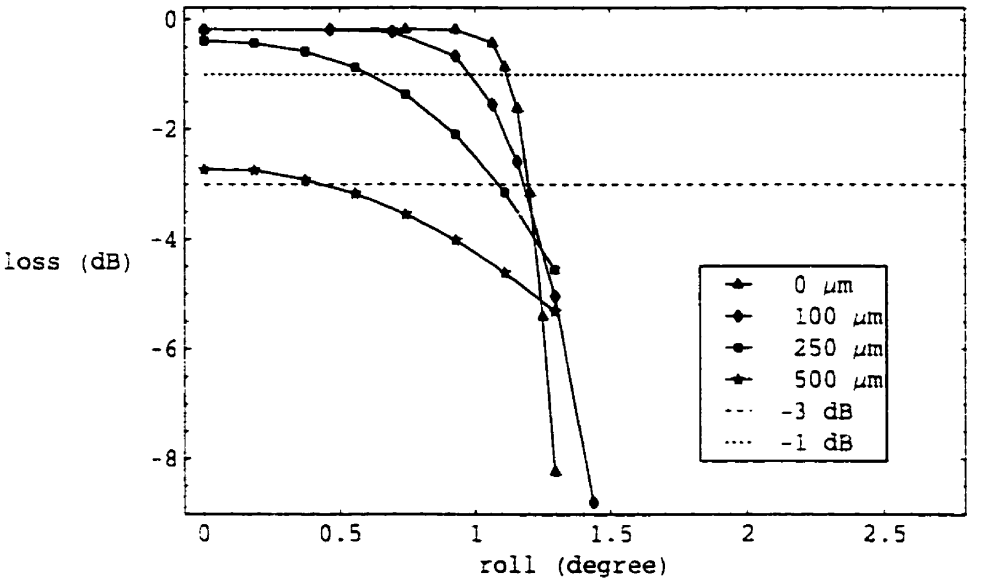

FIGURE 3.25 Insertion loss as a function of roll and distance. The core radius is 25 μm.

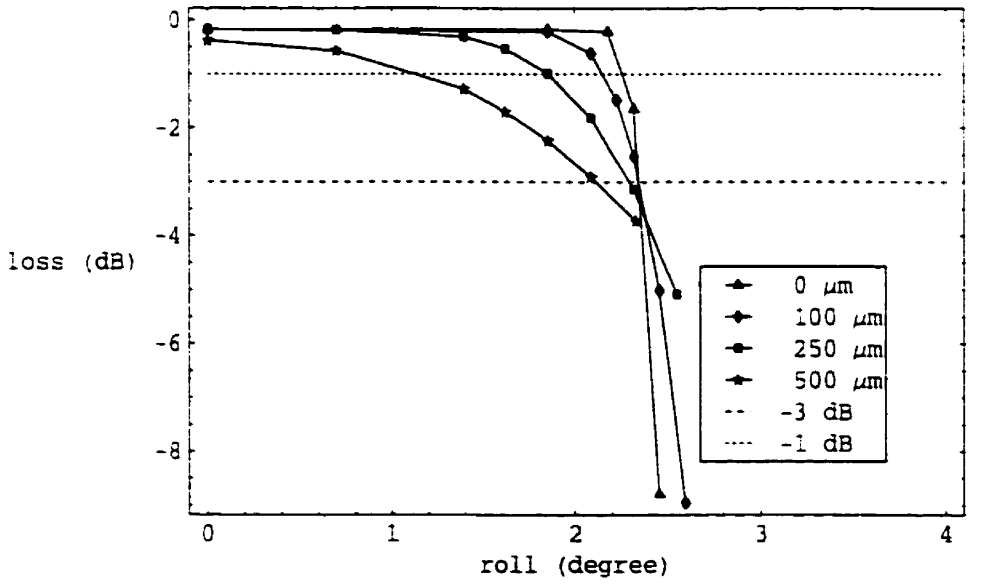

FIGURE 3.26 Insertion loss as a function of roll and distance. The core radius is 50 μm.

For systems using fibers with $a = 5$ μm, the -1 dB tolerance to roll is 0.2 degrees at a distance of 0 μm . For systems using larger core sizes, the tolerances are more relaxed, ranging from half a degree to 2.4 degrees depending on the value of a and the distance. When $a = 25$ μm, the -1 dB alignment requirements are respectively 1.1 degrees , 0.95 degrees, and 0.55 degrees, at distances of 0 μm, 100 μm, and 250 μm.

Though achievable, these tolerances are unnecessarely strict for an 8x8 array of channels. Certainly in the case of the smaller fibers, and even for 50 μm core fiber, a 250 μm pitch creates an enormous waste of available space, with tens of micrometers of cladding unnecessary to efficiently guide the light. By reducing the pitch and maintaining the number of channels, we linearly reduce S, which translates directly to an inverse linear increase (for small angles) in alignment tolerances to roll. Conversely, one can accept the previous alignment tolerances, reduce the pitch and increase the number of channels (half the pitch to obtain 4 times the number of channels). Figures 3.27 to 3.30 show the changes in roll tolerances which occurs with a change of pitch in our 8x8 array, for the different distances between source array and fiber array considered so far.

In many cases, depending on the core radius and the distance, it is possible to obtain alignment requirements ranging of 2 to 5 degrees with an appropriate selection of the pitch. The choice is not arbitrary and there are some fundamental limits to consider. An obvious limit is that the pitch should not reach the point where the cores begin to touch, in which case they can no longer be considered waveguides. But before such a limit is attained, unacceptable levels of crosstalk usually occur. If the cores of two waveguides are sufficiently close such that the fields of their modes overlap, light can be coupled from one

into the other as it propagates. Signals from one channel can leak to and mix with those of other channels.

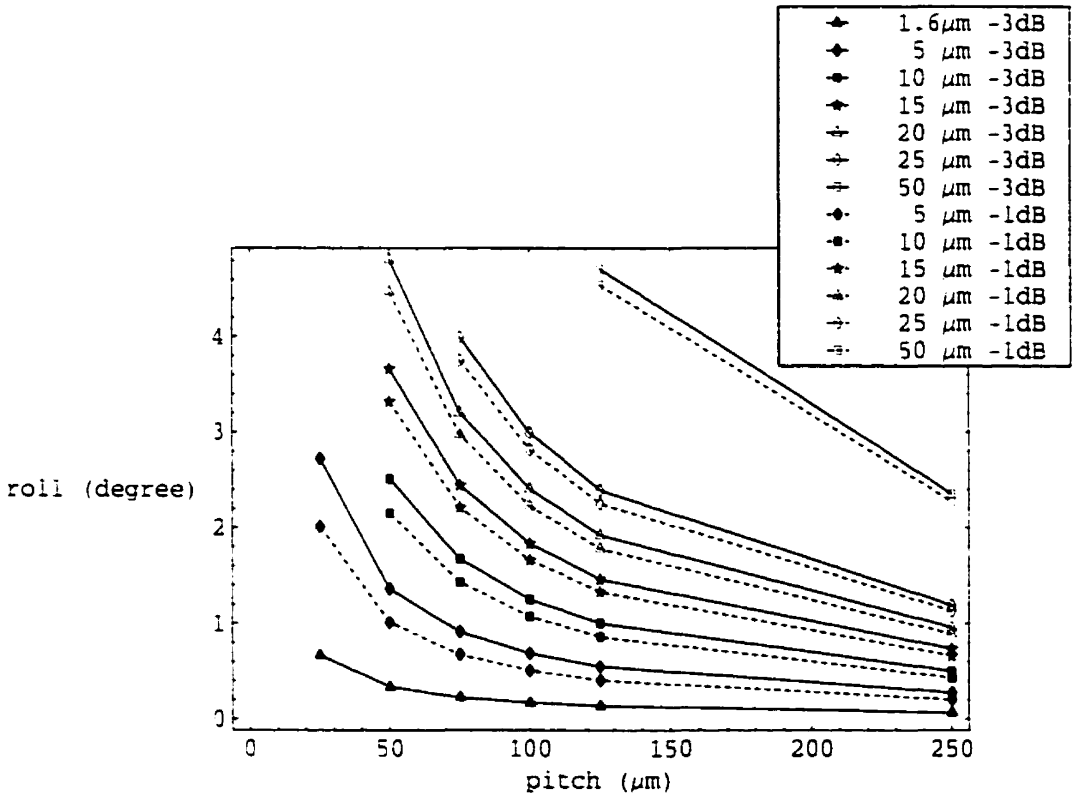

FIGURE 3.27 Roll alignment tolerances as a function of pitch, core radius, and minimum power requirements. The distance is 0 μm.

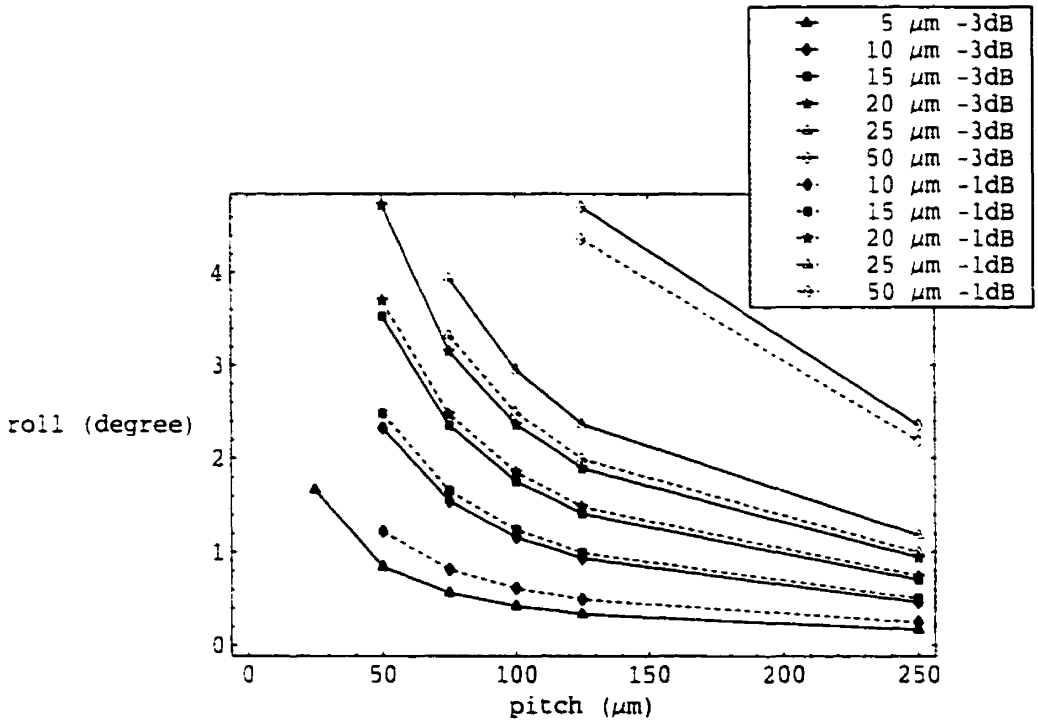

FIGURE 3.28 Roll alignment tolerances as a function of pitch, core radius, and minimum power requirements. The distance is 100 μm.

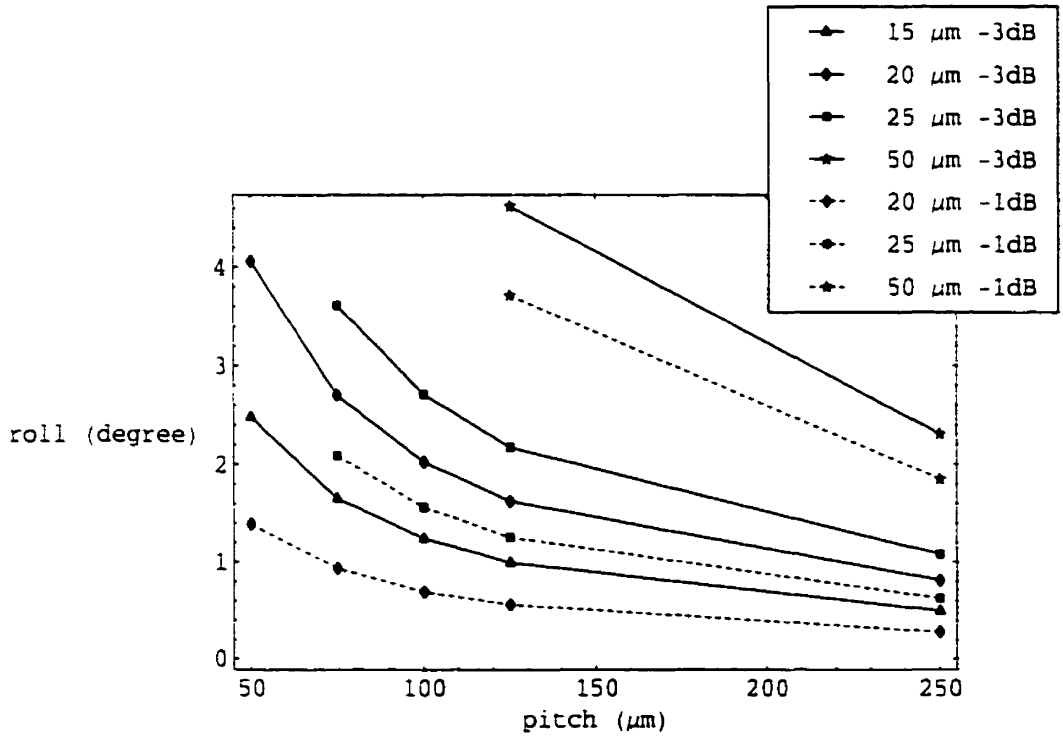

FIGURE 3.29 Roll alignment tolerances as a function of pitch, core radius, and minimum power requirements. The distance is 250 μm.

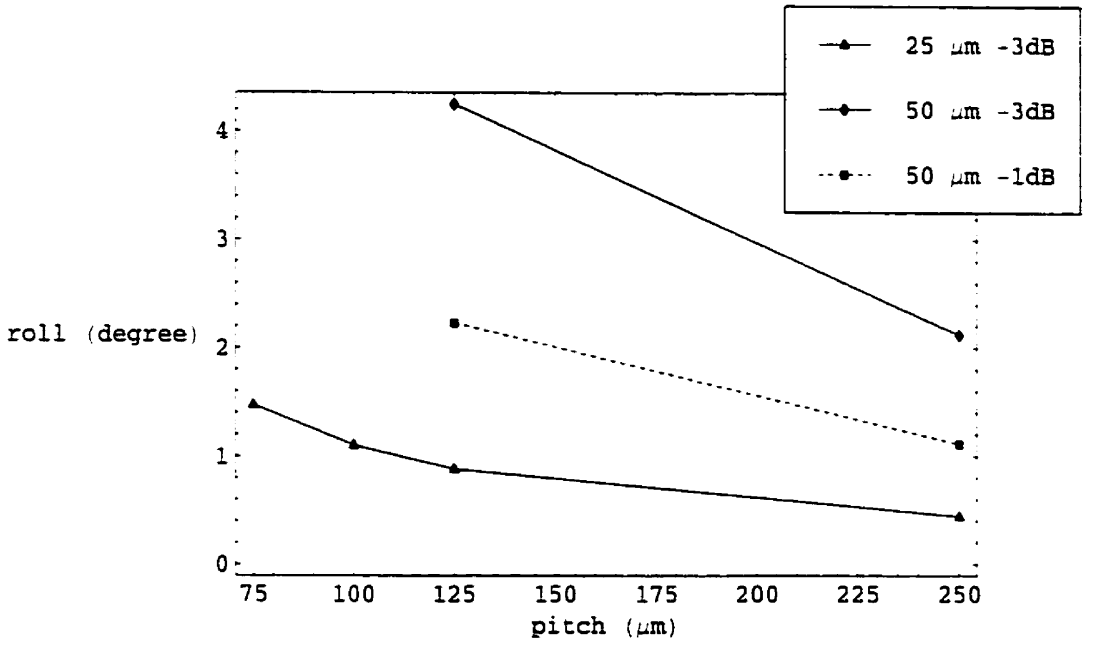

FIGURE 3.30 Roll alignment tolerances as a function of pitch, core radius, and minimum power requirements. The distance is 500 μm.

A formal approach to estimating optical crosstalk, by solving Maxwell's equations in the different regions of the array and using boundary conditions to determine the modes of the overall structure (which are different from those of the fibers taken in isolation), or by solving the equations of coupled-mode theory, is beyond the scope of this thesis. What we can do is estimate the optical crosstalk that occurs through the mechanism of direct launching of a beam's power into fibers adjacent to its appropriate channel. In the discussion that follows, any mention of optical crosstalk is assumed to refer to that which occurs through this process. A value for the crosstalk is obtained by calculating the launching efficiency for a fiber with an offset equal to the pitch. This approach assumes, as has been implicitely assumed so far, that the modes are those of the fibers taken in isolation (which becomes more inexact as the pitch becomes smaller and/or the core radius becomes larger). Results for different distances are show in figures 3.31 to 3.33, respectively. We

assume that aside from the axial separation the arrays are otherwise perfectly aligned. We included in the plots, in dashed lines, the -28 dB and -50 dB levels which corresponds to the total optical crosstalk between nearest neighbor and third-nearest neighbor channels, respectively, as measured in fiber image guides by Kosaka et al. 1997 for a 46 μm spacing between beams.

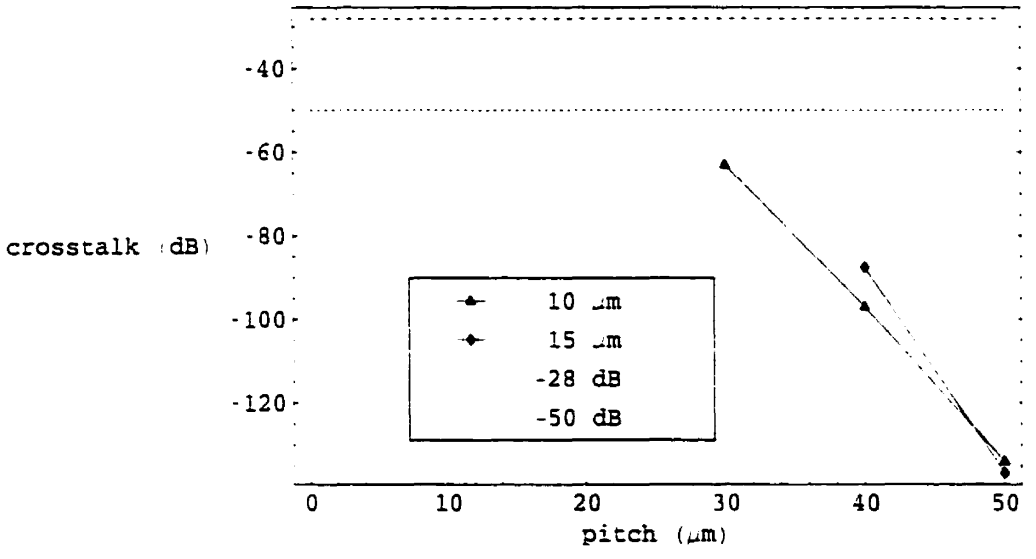

FIGURE 3.31 Crosstalk as a function of pitch and core radius. The distance is 100 μm.

Optical crosstalk increases with distance since the beam has a larger cross-section which penetrates a larger portion of the cladding and, in extreme cases, even the core of adjacent fibers. At a distance of 100 μm, the beams do not have enough spread to induce significant crosstalk in any of the fibers with $a \geq 10$ μm for any reasonable value of the pitch (no less than 10 μm of cladding between cores).

At a distance of 250 μm, significant amounts of crosstalk can occur in the smaller core fibers depending on the exact value of the pitch. For a given pitch, crosstalk increases with core radius, which is reasonable considering that the modes also increase in spread, thus

penetrating the cladding to a greater extent and making it easier for the power from adjacent beams to couple into them. In a 50 μm pitch array, the optical crosstalk is approximately -48 dB, -38 dB, and -30 dB for a core radius of 10 μm, 15 μm, and 20 μm, respectively. We must modify these values to account for the fact that most of the fibers have 4 nearest neighbors, in which case we must add +6 dB ($10\log_{10}4$) to the results. The first two cases compare favorably with image guides while we must consider an increase of pitch to 60 μm in the third case. If we increase the distance further, to 500 μm, only a pitch equal to or greater than 100 μm should be considered.

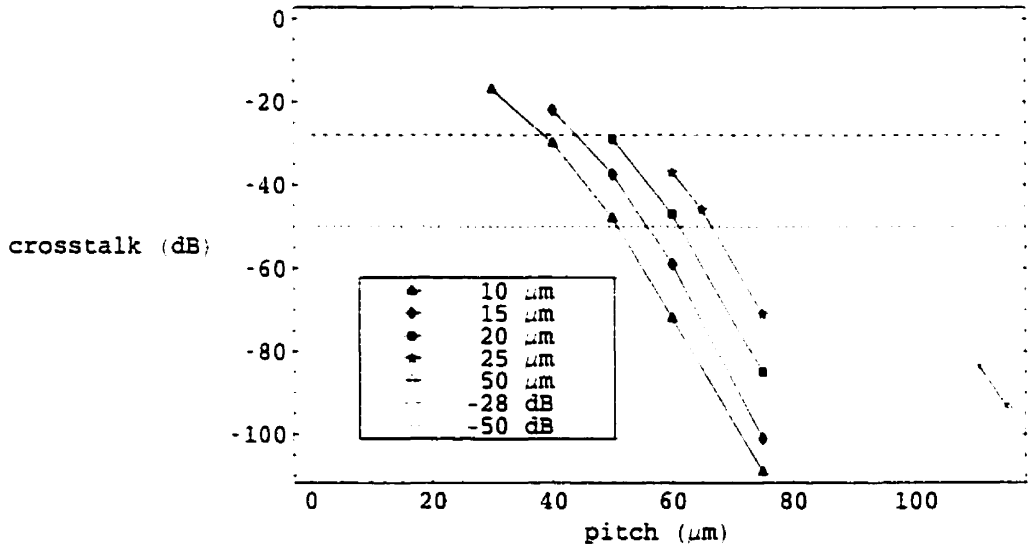

FIGURE 3.32 Crosstalk as a function of pitch and core radius. The distance is 250 μm.

For 25 μm core radius fibers, a 75 μm pitch array seems to be a suitable and even conservative choice (assuming no transfer between channels during propagation as discussed earlier), with an estimated value of optical crosstalk of less -70 dB for distances less than 250 μm, caused by direct launching at the input plane. To conclude this section, the -1 dB tolerances to roll for this array are 3.8 degrees, 3.4 degrees, and 2.1 degrees, at a

distance of 0 μm, 100 μm, and 250 μm, respectively. These results can easily be reduced to account for the 5 μm uncertainty in fiber position: 2.9 degrees, 2.5 degrees, and 1.1 degrees, respectively.

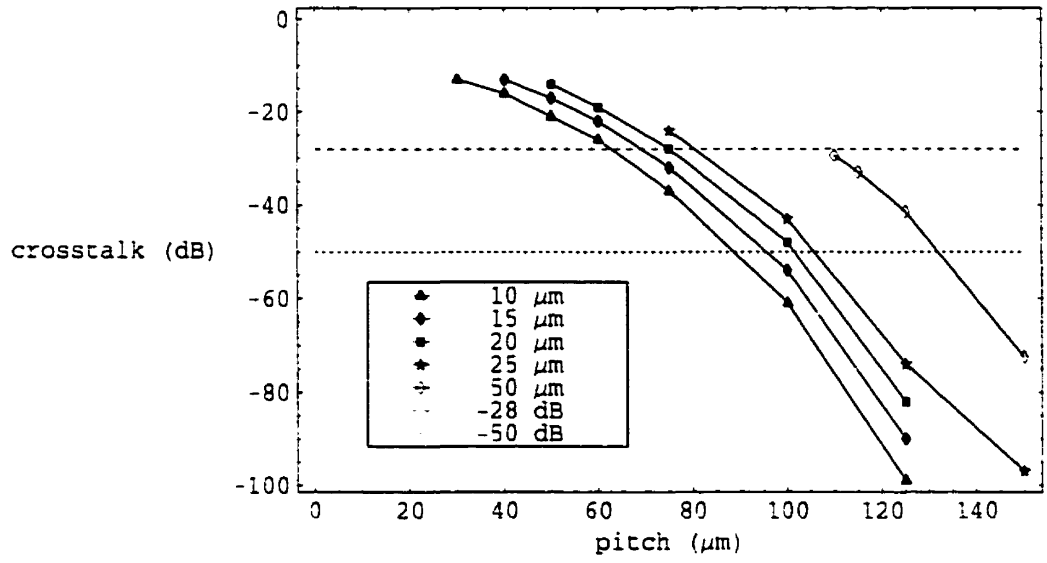

FIGURE 3.33 Crosstalk as a function of pitch and core radius. The distance is 500 μm.

3.3.4 Tilt

Finally, we consider tilt (figure 3.6). In this configuration, the channels in the bottom row (designated row 1) have a uniform launching efficiency which is only influenced by the oblique incidence of the beam. The top row (designated row 8) has additional offset and axial separation. This additional offset, o, and distance, s, is related to the tilt angle, α, by

$$\begin{aligned} o &= S(1-\cos\alpha) \\ s &= S\sin\alpha \end{aligned} \qquad (3.3)$$

where S is the distance between row 1 and 8.

For an 8x8 250 μm pitch array, S = 1750 μm. For this array, insertion loss curves as a function of tilt are shown in figure 3.34 to 4.40, respectively for each core size considered

here. In each these plots, we include data for both row 1 and row 8, for two values of the distance between the row 1 and the VCSEL array, 0μm, and 100 μm.

The launching efficiency in row 1 (the triangles) follow a definite pattern. For single-mode fiber, the -3 dB tilt tolerance for row 1, at a distance of 0 μm, is ~3.7 degrees. As the core radius increases, the -3 dB tolerances at 0 μm and 100 μm converge rapidly to a value quite close to that of the acceptance angle of the individual fibers (as determined by numerical aperture; ~11 degrees). In contrast, the launching efficiency of row 8 (the diamonds) drops much more quickly for fibers that have a small core radius. As the core radius increases, the fiber becomes less influenced by offset and distance, and tilt tolerances for row 8 improves. For 50 μm fiber, there is no significant difference between the tolerances of row 1 and row 8 up to the considered distance of 100 μm and none is expected up to 500 μm on the basis of the previous results for offset and VCSEL-fiber spacing.

As in the case of roll, alignment requirements for tilt can be improved by reducing the pitch of the array, in which case the tolerances of smaller core fibers should have values nearer to the acceptance angle, and this at larger distances. In our previous example, an 8x8 75 μm pitch array of 25 μm fibers, we find -1 dB alignment tolerances to tilt of 9 degrees at a distance of 0 μm and 100 μm, and 7 degrees at 250 μm.

We have investigated the effect of alignment on the insertion losses between an array of VCSELs and an ordered array of fibers. We will discuss the impact our results have on system design in the following chapter.

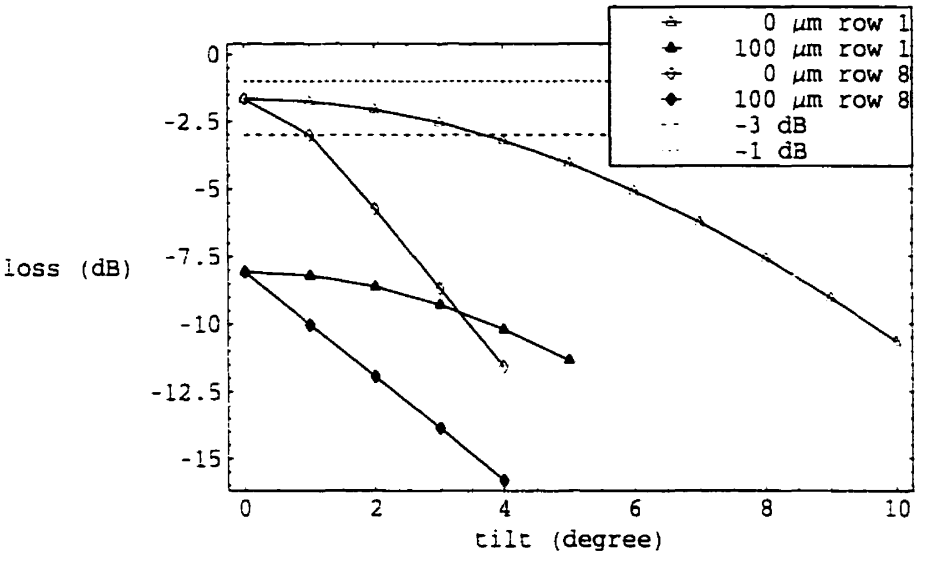

FIGURE 3.34 Insertion loss as a function of tilt, distance, and row number. The core radius is 1.6 μm.

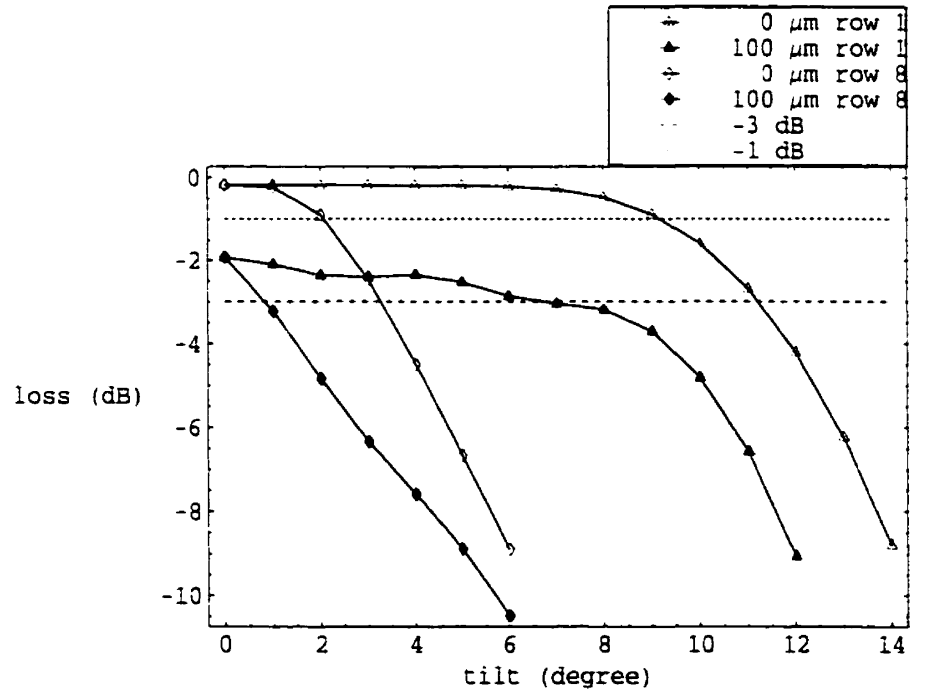

FIGURE 3.35 Insertion loss as a function of tilt, distance, and row number. The core radius is 5 μm.

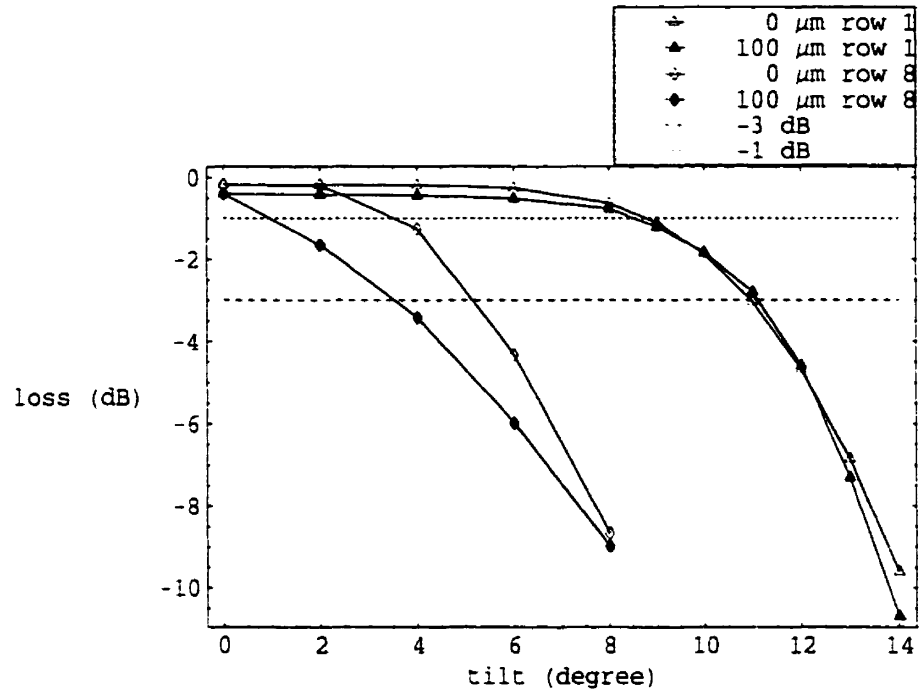

FIGURE 3.36 Insertion loss as a function of tilt, distance, and row number. The core radius is 10 μm.

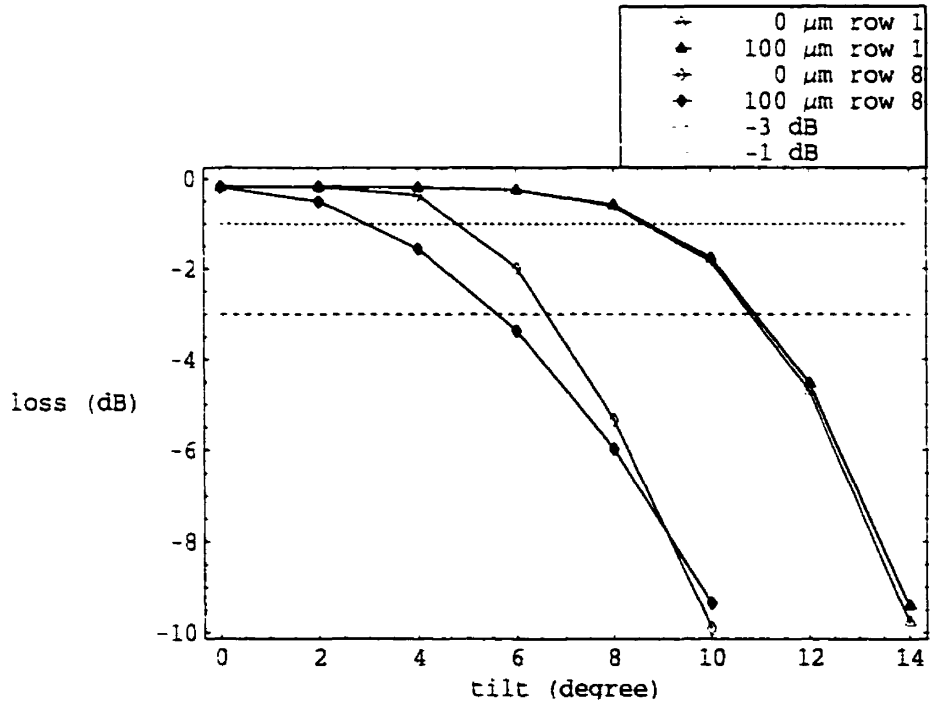

FIGURE 3.37 Insertion loss as a function of tilt, distance, and row number. The core radius is 15 μm.

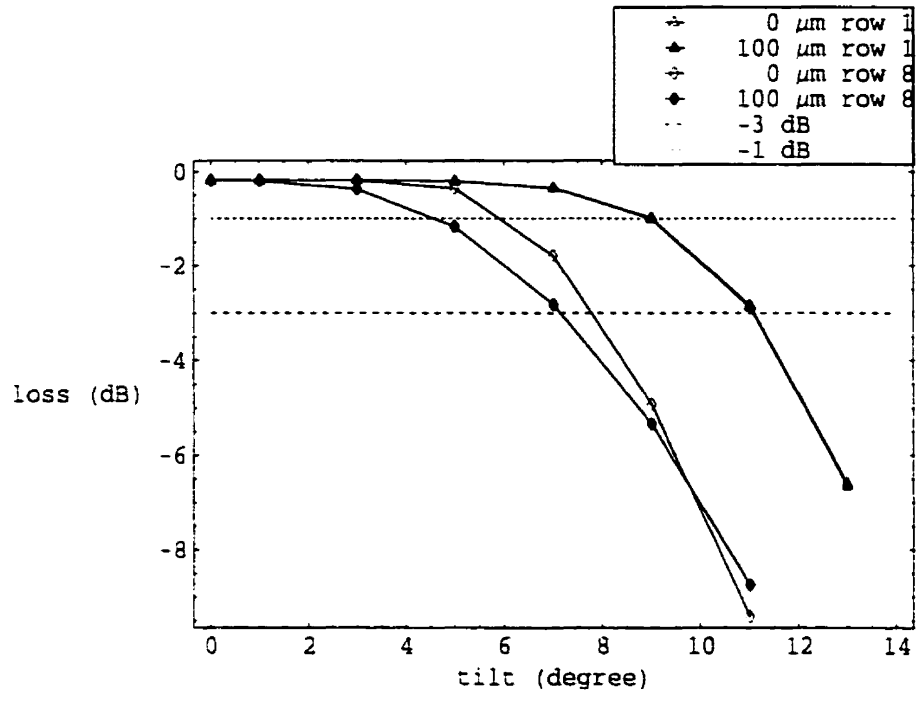

FIGURE 3.38 Insertion loss as a function of tilt, distance, and row number. The core radius is 20 μm.

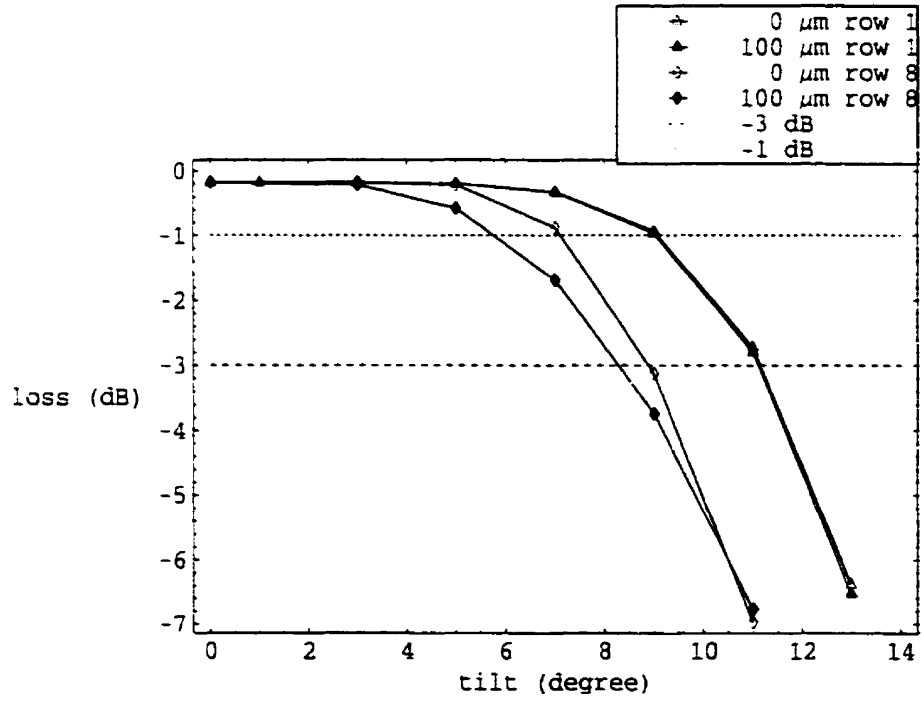

FIGURE 3.39 Insertion loss as a function of tilt, distance, and row number. The core radius is 25 μm.

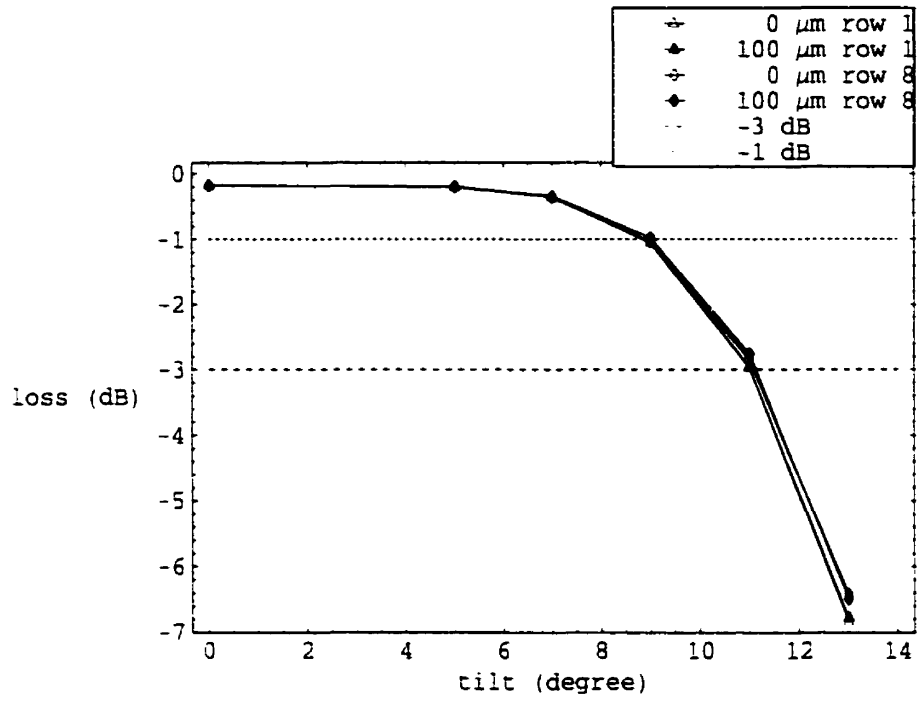

FIGURE 3.40 Insertion loss as a function of tilt, distance, and row number. The core radius is 50 μm.

Chapter 4

Conclusion

In the previous chapter, we presented results on the total launching efficiency under several alignment conditions between a fiber array and a typical VCSEL array, based on the numerical solutions to the equations derived in chapter 2. From these results, we were able to obtain -3 dB and -1 dB alignment requirements for distance, offset, roll, and tilt, as a function of the various choices of the array parameters: core size and array dimensions.

The launching efficiency coefficients were expressed by a normalized overlap integral between the aperture field and the individual fiber modes. The analysis involved several approximations of the underlying physics. The Born-Kirchhoff approximation simplifies the problem considerably by describing the aperture field in terms of plane waves from a uniform semi-infinite dielectric interface. We then assumed that the output from each VCSEL can be adequately modeled by a Gaussian beam. Based on previous research done by others, we then argue that the aperture field can also be described by a Gaussian beam whose parameters can be derived from the incident field. A small angle of incidence and the Fresnel approximation was frequently invoked to simplify our mathematical treatment. Finally, we assumed expressions for the optical modes which have been derived for an isolated, semi-infinite, single-clad, weakly-guiding, cylindrical

waveguide structure. The approximations described here are extensively used in research to model fiber coupling.We now offer a summary of our results.

As expected, alignment tolerances are strictest for single-mode fiber and become more relaxed with increasing core radius. Our results show that -1 dB performance is not possible for single-mode fiber without the use of some sort of focusing optical element, and the -3 dB tolerance to offset is ~1 μm. Since the issue of modal dispersion is not as critical for the transmission distances of data which characterizes optical backplane applications, the poorer insertion loss and stricter alignment conditions of single-mode fibers compared to multimode fiber does not justify their use at this interconnection level.

We have shown that the spacing between the source array and fiber array is a critical design parameter to minimize since not only does it set the baseline minimum insertion loss when no other forms of misalignment is present, its increase also reduces alignment tolerances to offset, roll, and tilt. Beyond a certain distance, high power transmission can no longer be supported by smaller core fibers. This distance will usually be restricted by the specifics of the packaging design, and will in turn determine the minimum value of the core radius of the fiber array elements (or vice-versa). Any design that can constrain the spacing between VCSELs and fibers to under 100 μm can support ordered arrays with individual core radii of 10 μm or more.

The lateral alignment of each individual fiber element to its beam is an equally important consideration for system design. Alignment tolerances to offset are approximately equal to the core radius for a VCSEL-fiber spacing of 0 μm and, though reduced, continue to increase linearly with it at larger spacings.

Roll misalignment can be treated as a special case of offset for the purpose of doing calculations, where the lateral displacement produced in individual fiber elements increases further away from the rotation axis. The roll tolerances are thus sensitive to the dimensions of the array, increasing with decreasing pitch or increasing for a smaller number of channels. In many cases, tolerances to roll of 2 to 4 degrees can be achieved for a suitable choice of pitch.

We base this choice of pitch on the premise of a preliminary study of optical crosstalk, involving the direct coupling of a beam into adjacent fibers. As expected, we find that arrays made of large core radius fiber cannot support pitches as low as those made of smaller core radius fiber. Nevertheless, we should note that arrays made of larger core fibers usually remain somewhat more tolerant to roll than smaller ones. The main impact on system design is that there is a trade-off between relaxed alignment tolerances and throughput density (bandwidth per unit area).

When tilt is considered, we have shown that high numerical aperture fiber elements are unnecessary. When the core radius is small, the alignment tolerance is determined by the axial and lateral shift in the row furthest to the tilt axis rather than by the acceptance angle of the individual fiber elements. For larger core radii, the alignment tolerances rapidly converges to a value equal to or slightly lower than the acceptance angle. The acceptance angle in this case is 11.54 degrees for $NA = 0.2$, which is more than sufficient for alignment purposes when larger core fibers are involved.

As a design example, we have also underlined the -1 dB alignment tolerances for an 8x8 75 μm pitch array, with individual cores of 25 μm radius located within 5 μm of their

ideal lateral position (the square lattice). With these parameters, we concluded that the remaining tolerance budgets for packaging are, at a distance of 0 μm, 100 μm, and 250 μm respectively: 19 μm, 16 μm, and 7 μm for offset, 2.9 degrees, 2.5 degrees, and 1.1 degrees for roll, and finally, 9 degrees of tilt in the first and second case and 7 degrees in the third.

Of course, these numbers are suitably reduced when more than one form of misalignment is present. Nevertheless, connectors are routinely being made to position a single single-mode fiber to micrometer accuracy for long-distance telecommunications and it should not be difficult to design, manufacture and maintain one to position the above fiber array to within the above specifications for interboard data transmission. With each channel operating at 1 Gb/s, the total throughput for the above interconnect would be 64 Gb/s, with a throughput density of 17.8 Tb s^{-1} cm^{-2}. Interestingly, extremely large core radius fiber elements are not necessary to obtain adequate positioning requirements. Given the recent popularity of large core ($a > 250$ μm) plastic optical fiber, interconnects made of these fibers would be bulky and have lower throughput densities then those made of fiber elements with $a \leq 50$ μm.

We have thus demonstrated that multimode ordered fiber arrays fabricated with the rod in tube method can be attractive candidates for high-speed parallel optical short-distance communications. These arrays can be easily mass-produced and have the advantage of more efficient power transmission over traditional, closely packed, image guide technologies. Furthermore, we argue that their reduced alignment tolerances, compared to image guides, should be compatible with present-day packaging capabilities. That is the main conclusion of this thesis.

Finally, we offer several directions for additional research. Do the actual numbers presented here reflect the true performance of a device? Certainly, experimental measurements should be attempted. Rigorous ab initio methods can also be of use to verify our results. For instance, it may be possible in certain cases to solve Maxwell's equations numerically by using a finite element or a finite-difference time-domain approach. A more thorough study of optical crosstalk inside the fiber array, using realistic models, can provide a better measure of the lower limit of the pitch for a given core radius. From these results, a clearer understanding can be obtained of the trade-offs between the alignment tolerances, total throughput and throughput density of interconnects using these arrays. A dispersion analysis can be performed to determine the maximum modulation for each channel. If needed, arrays of graded-index fibers could conceivably be constructed, and the model presented in chapter 2 can be adapted to estimate the launching efficiency. Cross-coupling between modes during propagation can be investigated. Other refinements, such as realistic beam models, are also possible. Finally, a more exhaustive search of parameter space can be attempted to constrain the optimal interconnect design. The only limit is time and effort.

Appendix A

Optical fiber modes

A.1 Exact Expressions

An outline of how the exact forms for the modes are obtained is instructive and will help understand the approximations that will follow. Formally, the modes can be found by solving Maxwell's equations for a charge-free dielectric medium.

$$\begin{aligned} \nabla\times\boldsymbol{H} &= \varepsilon\frac{\partial \boldsymbol{E}}{\partial t} \\ \nabla\times\boldsymbol{E} &= -\mu\frac{\partial \boldsymbol{H}}{\partial t} \\ \nabla\bullet(\varepsilon\boldsymbol{E}) &= 0 \end{aligned} \qquad \text{(A-1)}$$

where ε and μ are the electric and magnetic permeabilities of the medium. Since most fibers are cylindrically symmetric, the use of the cylindrical coordinate system is convenient. But because the unit vectors $\mathbf{a}_\rho$ and $\mathbf{a}_\phi$ are vectors which change direction relative to a cartesian coordinate system, the wave equations involving the transverse components, derived from equations (A-1), are quite complicated. However, the wave equations for the longitudinal components, the z direction, remains simple as shown below:

$$\left[a^2\nabla_t^2 + \begin{pmatrix} u_p^2 \\ -w_p^2 \end{pmatrix}\right]\{E_{pz} \text{ or } H_{pz}\} = 0 \qquad \begin{matrix} R<1 \\ R>1 \end{matrix}, \tag{A-2}$$

where $R = \rho/a$ is the normalized radius, $\nabla_t^2 = \nabla^2 - \partial^2/\partial z^2$ is the transverse Laplacian and u_p and w_p are the normalized transverse propagation and attenuation constants, respectively. Furthermore, u_p and w_p are interrelated because

$$u_p^2 + w_p^2 = V^2, \tag{A-3}$$

where V is the normalized frequency given by

$$V = \frac{2\pi a}{\lambda_0}\sqrt{n_1^2 - n_2^2}, \tag{A-4}$$

where λ_0 is the wavelength in free space.

Due to cylindrical symmetry, the p^{th} mode propagating along the fiber has vector fields given by

$$\begin{aligned} \boldsymbol{E}_p(x, y, z) &= \{\boldsymbol{e}_p(x, y) + \boldsymbol{E}_{pz}(x, y)\}e^{j\left(\omega t - \frac{\beta_p}{a}z\right)} \\ \boldsymbol{H}_p(x, y, z) &= \{\boldsymbol{h}_p(x, y) + \boldsymbol{H}_{pz}(x, y)\}e^{j\left(\omega t - \frac{\beta_p}{a}z\right)} \end{aligned}. \tag{A-5}$$

where the fields have been separated in transverse and longitudinal components. β_p is the normalized modal propagation constant given by

$$\beta_p = k'^2(1 - \theta_p^2), \tag{A-6}$$

where

$$\theta_p = \frac{u_p}{k'} = \sqrt{\delta}\frac{u_p}{V} \tag{A-7}$$

and k' is the normalized propagation constant in the z direction in the core medium

$$k' = \frac{2\pi a}{\lambda_c} = \frac{2\pi a}{\lambda_0} n_1 . \tag{A-8}$$

When the dielectric and magnetic permeabilities are functions of the transverse coordinates only, the transverse components of the modal fields are derivable from the longitudinal components (Stratton 1941):

$$\begin{pmatrix} u_p^2 \\ -w_p^2 \end{pmatrix} \boldsymbol{h}_p = ja\beta_p \left[\nabla_t H_{pz} + \left(\frac{k'}{\beta_p}\right) \sqrt{\frac{\varepsilon_1}{\mu}} \begin{pmatrix} 1 \\ 1-\delta \end{pmatrix} \hat{z} \times \nabla_t E_{pz} \right] \qquad \begin{matrix} R < 1 \\ R > 1 \end{matrix}$$

$$\begin{pmatrix} u_p \\ -w_p \end{pmatrix} \boldsymbol{e}_p = ja\beta_p \left[\nabla_t E_{pz} + \left(\frac{k'}{\beta_p}\right) \sqrt{\frac{\mu}{\varepsilon_1}} \hat{z} \times \nabla_t H_{pz} \right] \qquad \begin{matrix} R < 1 \\ R > 1 \end{matrix} \tag{A-9}$$

where δ is given by

$$\delta = 1 - \left(\frac{\varepsilon_2}{\varepsilon_1}\right) = 1 - \left(\frac{n_2}{n_1}\right)^2 . \tag{A-10}$$

From equations (A-2) and (A-9), we can obtain expressions for the modes,

$$e_\rho = j\beta\begin{bmatrix}\frac{1}{u}\{\gamma_1 J_{l-1}(uR)+\gamma_2 J_{l+1}(uR)\}\\ \frac{\eta_3}{w}\{\gamma_1 K_{l-1}(wR)-\gamma_2 K_{l+1}(wR)\}\end{bmatrix} g_1(\varphi) \qquad \begin{bmatrix}R<1\\ R>1\end{bmatrix}$$

$$e_\varphi = j\beta\begin{bmatrix}\frac{1}{u}\{\gamma_1 J_{l-1}(uR)-\gamma_2 J_{l+1}(uR)\}\\ \frac{\eta_3}{w}\{\gamma_1 K_{l-1}(wR)+\gamma_2 K_{l+1}(wR)\}\end{bmatrix} g_2(\varphi) \qquad \begin{bmatrix}R<1\\ R>1\end{bmatrix}$$

$$h_\rho = j\,k'\sqrt{\frac{\varepsilon_1}{\mu}}\begin{bmatrix}\frac{1}{u}\{-\gamma_3 J_{l-1}(uR)+\gamma_4 J_{l+1}(uR)\}\\ -\left(\frac{\eta_3}{w}\right)\{\gamma_5 K_{l-1}(wR)+\gamma_6 K_{l+1}(wR)\}\end{bmatrix} g_2(\varphi) \qquad \begin{bmatrix}R<1\\ R>1\end{bmatrix}. \qquad \text{(A-11)}$$

$$h_\varphi = j\,k'\sqrt{\frac{\varepsilon_1}{\mu}}\begin{bmatrix}\frac{1}{u}\{\gamma_3 J_{l-1}(uR)+\gamma_4 J_{l+1}(uR)\}\\ \frac{\eta_3}{w}\{\gamma_5 K_{l-1}(wR)-\gamma_6 K_{l+1}(wR)\}\end{bmatrix} g_1(\varphi) \qquad \begin{bmatrix}R<1\\ R>1\end{bmatrix}$$

$$E_z = \begin{bmatrix}J_l(uR)\\ \eta_3 K_l(wR)\end{bmatrix} g_1(\varphi) \qquad \begin{bmatrix}R<1\\ R>1\end{bmatrix}$$

$$H_z = \sqrt{\frac{\varepsilon_1}{\mu}}\left(\frac{F_2}{\beta}\right)\left\{\frac{g_1(\varphi)}{g_2(\varphi)}\right\}E_z$$

where

$$\eta_3 = \frac{J_l(u)}{K_l(w)}. \qquad \text{(A-12)}$$

The γ's are given by

$$\begin{aligned}2\gamma_1 &= F_2 - 1\\ 2\gamma_2 &= F_2 + 1\\ 2\gamma_3 &= F_1 - 1\\ 2\gamma_4 &= F_1 + 1\\ 2\gamma_5 &= 2\gamma_3 + \delta\\ 2\gamma_6 &= 2\gamma_4 - \delta\end{aligned}, \qquad \text{(A-13)}$$

where

$$F_1 = \frac{1}{F_2} - \frac{\theta_p^2 w^2 \eta_2}{l}, \tag{A-14}$$

$$F_2 = \left(\frac{v}{uw}\right)^2 \left[\frac{l}{\eta_1 + \eta_2}\right], \tag{A-15}$$

$$\eta_1 = \frac{J_l'(u)}{uJ_l(u)} = \pm\left[\frac{J_{l\pm1}(u)}{uJ_l(u)}\right] \mp \frac{l}{u^2}, \tag{A-16}$$

and

$$\eta_2 = \frac{K_l'(w)}{wK_l(w)} = -\left[\frac{K_{l\pm1}(w)}{wK_l(w)}\right] \mp \frac{l}{w^2}. \tag{A-17}$$

The g functions are given by

$$g_1(\varphi) = \begin{pmatrix} \sin(l\varphi) \\ \text{or} \\ \cos(l\varphi) \end{pmatrix}$$

$$g_2(\varphi) = \begin{pmatrix} \cos(l\varphi) \\ \text{or} \\ -\sin(l\varphi) \end{pmatrix} \tag{A-18}$$

The two possible choices for each function g corresponds to the two possible states of polarization.Whenever the double sign notation is used, upper sign corresponds to the hybrid HE_{lm} modes while the lower sign is for the EH_{lm} modes. The subscript l corresponds to azimuthal variations and m corresponds to radial variations. The J_l and K_l are the Bessel

function of order l and modified Hankel function of order l, respectively. When $l = 0$, the fields degenerate to the TM_{0m} and TE_{0m} modes:

$$E_z = \begin{bmatrix} J_0(uR) \\ \eta_3 K_0(wR) \end{bmatrix} \qquad \begin{matrix} R < 1 \\ R > 1 \end{matrix}$$

$$e_\rho = j\,\beta \begin{bmatrix} \dfrac{J_1 uR}{u} \\ \dfrac{-\eta_3 K_1(wR)}{w} \end{bmatrix} \qquad \begin{matrix} R < 1 \\ R > 1 \end{matrix} \qquad TM_{0m}. \tag{A-19}$$

$$h = \frac{k'}{\beta}\sqrt{\frac{\varepsilon_1}{\mu}}\hat{z} \times e \begin{bmatrix} 1 \\ 1-\delta \end{bmatrix} \qquad \begin{matrix} R < 1 \\ R > 1 \end{matrix}$$

and

$$H_z = \frac{\beta}{k'}\sqrt{\frac{\varepsilon_1}{\mu}} \begin{bmatrix} J_0(uR) \\ \eta_3 K_0(wR) \end{bmatrix} \qquad \begin{matrix} R < 1 \\ R > 1 \end{matrix}$$

$$e_\phi = j\,\beta \begin{bmatrix} \dfrac{J_1(uR)}{u} \\ \dfrac{\eta_3 K_1(wR)}{w} \end{bmatrix} \qquad \begin{matrix} R < 1 \\ R > 1 \end{matrix} \qquad TE_{0m}. \tag{A-20}$$

$$h = \frac{\beta}{k'}\sqrt{\frac{\varepsilon_1}{\mu}}\hat{z} \times e \qquad \begin{matrix} R < 1 \\ R > 1 \end{matrix}$$

The subscript p has been dropped for convenience.

The next step is to apply boundary conditions to the fields at the interface between the core and the cladding. By so doing, one obtains the eigenvalue equation of the waveguide

$$F_2 - F_1 = \theta_p^2 F_2 \qquad \text{or equivalently} \qquad \left(\frac{1}{F_2}\right)^2 - 1 = \theta_p^2\left[\frac{w_p^2\eta_2}{lF_2} - 1\right]. \tag{A-21}$$

The eigenvalue equation can then be solved to obtain the complete set of u_p's.

A.2 Asymptotic expressions

Snyder (1969a) noted that considerable simplification results in the eigenvalue equations when $\theta_p \ll 1$. By representing all quantities by a power series of θ_p, zero-order expressions can be obtained. Thus, for example, we have

$$u_p(v, \theta_p) = U + \theta_p u^{(1)} + \theta_p^2 u^{(2)} + \ldots. \tag{A-22}$$

$$w_p(v, \theta_p) = W + \theta_p w^{(1)} + \theta_p^2 w^{(2)} + \ldots. \tag{A-23}$$

$$F_2(\theta_p) = F_2^{(0)} + \theta_p F_2^{(1)} + \theta_p^2 F_2^{(2)} + \ldots. \tag{A-24}$$

Substituting the power series within the eigenvalue equation and the equation for V leads to simple expressions when like powers of θ_p are equated. The zero-order in θ_p-U_p expressions are given by

$$V^2 = U^2 + W^2, \tag{A-25}$$

$$F_1^{(0)} = F_2^{(0)} = \mp 1, \tag{A-26}$$

and

$$\frac{UJ_l(U)}{J_{l\mp1}(U)} = \pm\frac{WK_l(W)}{K_{l\mp1}(W)}, \tag{A-27}$$

where the last equation is the asymptotic form of the eigenvalue equation.

An equivalent equation can be obtain by substituting appropriate Bessel recurrence formulas (Snyder 1969a) into (A-27) to obtain

$$\frac{UJ_{l\mp 2}(U)}{J_{l\mp 1}(U)} = \mp\frac{WK_{l\mp 2}(W)}{K_{l\mp 1}(W)} \qquad \text{(A-27 b)}$$

The eigenvalue equation can be solved numerically or graphically (see figure A.1) for U.

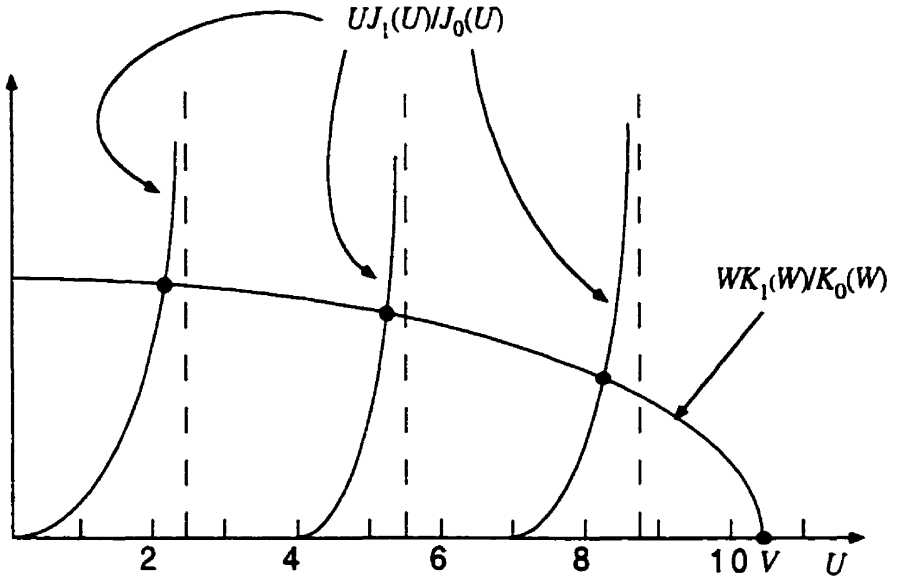

FIGURE A.1 Graphical construction for solving equation (A-27 b) for the HE_{1m} modes

Each intersection in figure A.1 represents a solution, with $U_p = U$, to the eigenvalue equation and corresponds to a valid mode. The left-handed side of the eigenvalue equation has multiple branches, which are independent of V, intersecting the abscissa at the roots of $J_{l\mp 2}(U)$ while the right-handed side intersects each branch once and meets the abscissa

when $U = V$. As V increases, so does the number of modes allowed. The roots of $J_{l-2}(U)$ are called the cutoff values of the modes, since V must be higher than this value in order for the appropriate mode to be excited. When V<2.405, all modes except HE_{11} are cut off and operates as a single-mode waveguide. Near cutoff,

$$\begin{aligned} U_p &\approx V \\ W_p &\approx 0 \end{aligned} \tag{A-28}$$

while far from cutoff,

$$U_p \approx U_p^{\infty}, \tag{A-29}$$

where U_p^{∞} are the roots of $J_{l \mp 1}(U)$, and corresponds to the dashed line in fig.A.1: that is,

$$U_p^{\infty} \approx \begin{cases} 2.405 & HE_{11} \\ 3.832 & TM_{01}, TE_{01}, HE_{21} \\ 5.135 & EH_{11}, HE_{31} \\ 5.520 & HE_{12} \\ 6.370 & EH_{21}, HE_{41} \\ 7.016 & TM_{02}, TE_{02}, HE_{22} \end{cases} . \tag{A-30}$$

From the definition of θ_p (2.11), it can be seen that $\theta_p^2 \ll 1$ for all δ when far from cutoff. However, at cutoff, $\theta_p^2 = \delta$ which is it's largest value. Thus, if $\delta \ll 1$ then the asymptotic approximation is valid for all values of V.

Although the eigenvalue equation require numerical or graphical solutions, it can be shown (Snyder 1969a) that U_p is in excellent agreement with

$$U_p(V) = U_p^{\infty} e^{-1/V}, \tag{A-31}$$

unless near cutoff.

The expressions for the fields also take simpler forms when $\theta_p^2 \ll 1$. Using

$$\beta_p = k' + O(\theta_p^2), \tag{A-32}$$

then (A-9) becomes

$$\boldsymbol{h}_p = \sqrt{\frac{\varepsilon_1}{\mu}} \begin{bmatrix} 1 \\ 1-\delta \end{bmatrix} \hat{z} \times \boldsymbol{e}_p \qquad \begin{bmatrix} R<1 \\ R>1 \end{bmatrix} + O(\theta_p^2), \tag{A-33}$$

and when $\delta \ll 1$,

$$\boldsymbol{h}_p = \sqrt{\frac{\varepsilon_1}{\mu}} \hat{z} \times \boldsymbol{e}_p \qquad \text{for all } R. \tag{A-34}$$

Furthermore, by expanding the fields, given by (A-11), as power series of θ_p and equating like powers we can obtain approximate forms for the fields.

From the zero-order expressions of F_1 and F_2 (2.31), the γ's are given by

$$\begin{aligned} \gamma_1^{(0)} = \gamma_3^{(0)} &= \begin{cases} 1 & \text{HE} \\ 0 & \text{EH} \end{cases} \\ \gamma_2^{(0)} = \gamma_4^{(0)} &= \begin{cases} 0 & \text{HE} \\ 1 & \text{EH} \end{cases} \end{aligned} \tag{A-35}$$

Using (A-27),(A-32), (A-35) and multiplying by a common factor

$$\begin{cases} \dfrac{jU}{kJ_{l\mp1}(U)} & \text{hybrid modes} \\ \dfrac{-jU}{kJ_1(U)} & l = 0 \text{ modes} \end{cases} \tag{A-36}$$

the longitudinal components become

$$E_{pz} = \begin{cases} j\,\theta_p\left(\dfrac{J_l(U)}{J_{l\mp1}(U)}\right)\begin{pmatrix}\sin(l\varphi)\\ \text{or}\\ \cos(l\varphi)\end{pmatrix} f_{l\pm1}(R) & \text{hybrid} \\ -j\,\theta_p\left(\dfrac{J_0(U)}{J_1(U)}\right) f_0(R) & \text{TM} \\ 0 & \text{TE} \end{cases}$$

$$H_{pz} = \begin{cases} \mp\sqrt{\dfrac{\varepsilon_1}{\mu}}\begin{pmatrix}\cot(l\varphi)\\ \text{or}\\ -\tan(l\varphi)\end{pmatrix} E_{pz} & \text{hybrid} \\ 0 & \text{TM} \\ -j\sqrt{\dfrac{\varepsilon_1}{\mu}}\theta_p\left(\dfrac{J_0(U)}{J_1(U)}\right) f_0(R) & \text{TE} \end{cases} \tag{A-37}$$

while the transverse components are given by

$$e_\rho = \begin{cases} \pm\begin{pmatrix}\sin(l\varphi)\\ \text{or}\\ \cos(l\varphi)\end{pmatrix} f_l(R) & \text{hybrid} \\ -f_0(R) & \text{TM} \\ 0 & \text{TE} \end{cases} \tag{A-38}$$

$$e_\phi = \begin{cases} \begin{pmatrix} \cos(l\varphi) \\ \text{or} \\ -\sin(l\varphi) \end{pmatrix} f_l(R) & \text{hybrid} \\ 0 & \text{TM} \\ f_0(R) & \text{TE} \end{cases} . \tag{A-39}$$

where

$$f_l(R) = \begin{cases} \dfrac{J_{l\mp1}(UR)}{J_{l\mp1}(U)} & R<1 \\ \dfrac{K_{l\mp1}(WR)}{K_{l\mp1}(W)} & R>1 \end{cases} . \tag{A-40}$$

The longitudinal fields are of order θ_p smaller than the transverse fields and are negligible.

We require that the modes be orthonormal. Thus we define a normalization constant

$$\psi_p = \int (\boldsymbol{e}_p \times \boldsymbol{h}_p)\cdot \hat{\mathbf{z}}\, da = \sqrt{\frac{\varepsilon_1}{\mu}}\int |\boldsymbol{e}_p|^2 da = 2\pi a^2 \sqrt{\frac{\varepsilon_1}{\mu}}\int_0^\infty R\, f_l^2(R)\, dR . \tag{A-41}$$

After doing the integration and applying the eigenvalue equation, we find

$$\psi_p = \sqrt{\frac{\varepsilon_1}{\mu}}\pi a^2 \left(\frac{V}{U_p}\right)^2 \xi , \tag{A-42}$$

where

$$\xi = \frac{K_l(W)K_{l\mp2}(W)}{K_{l\mp1}(W)}. \tag{A-43}$$

Normalizing and applying a coordinate transformation to (2.43) and (2.44) leads to

$$\sqrt{\psi_p}\boldsymbol{e}_p = \sqrt{\psi_p}\sqrt{\frac{\varepsilon_1}{\mu}}\boldsymbol{h}_p \times \hat{z} = \begin{cases} \left[\hat{x}\begin{bmatrix}\sin(l\mp1)\varphi \\ \text{or} \\ \cos(l\mp1)\varphi\end{bmatrix} + \hat{y}\begin{bmatrix}\cos(l\mp1)\varphi \\ \text{or} \\ -\sin(l\mp1)\varphi\end{bmatrix}\right] f_l(R) & \text{hybrid} \\ -(\hat{x}\cos\varphi + \hat{y}\sin\varphi)f_0(R) & \text{TM} \\ (-\hat{x}\sin\varphi + \hat{y}\cos\varphi)f_0(R) & \text{TE} \end{cases} \tag{A-44}$$

Equation (A-44) will be the expressions used in chapter 2. Notice that the HE_{1m} modes have no azimuthal dependence.

Gloge (1971) has shown that from the asymptotic expressions for the fields, it is possible to construct modes, the LP_{lm} modes, whose transverse components are essentially polarized in one direction. LP modes constitute a different basis which we could have used to expand the fields at the fiber face. The LP basis was not used here in order to keep the notation consistent with Snyder (1969b).

For weakly-guiding fiber, $\delta \ll 1$, most of the modes are actually degenerate meaning that they have identical eigenvalues, U_p; that is, most modes satisfy an identical eigenvalue equation to that of other modes, (A-27) or (A-27 b), once the appropriate transformation by Bessel function recurrence formula is performed. Thus, the TM_{0m} and TE_{0m} modes are degenerate with the HE_{2m} modes. The same is true between the EH_{lm} and $HE_{(l+2)m}$ modes.

Appendix B

Gaussian beams

The Gaussian beam is a frequently used model in optics. Its popularity stems from the fact that it represents a possible solution for the field inside a cavity resonator (Kogelnik and Li 1966), and so is an adequate initial model for many lasers.

Let assume that the tangential component of the electric field on the reference plane $z'=0$ (see figure 2.4) is well described by the Gaussian function $\exp(-\rho^2/w_0^2)$:

$$\boldsymbol{E}(x', y', 0) = E_0 e^{-(\rho'/w_0)^2} \hat{\boldsymbol{y}}'. \tag{B-1}$$

The constant w_0 is called the beam waist and corresponds to the radial distance from the origin, along the $z'=0$ plane, defining the circle into which 86% of the power of the beam is concentrated. The spectral function (Smith 1997) corresponding to (B-1) is given by

$$F_y(k_x, k_y) = E_0 \int_{x=-\infty}^{\infty} e^{-(x/w_0)^2 + jk_x x} dx \int_{x=-\infty}^{\infty} e^{-(y/w_0)^2 + jk_y y} dy, \tag{B-2}$$

where the superscript ' have been conveniently omitted, and k_x and k_y are the vector wave number components along x and y respectively. Each of the integrals can be evaluated using

$$\int_{-\infty}^{\infty} e^{-(pu)^2 \pm qu} du = \frac{\sqrt{\pi}}{p} e^{(q/2p)^2} \qquad p > 0, \tag{B-3}$$

to obtain

$$F_y(k_x, k_y) = \pi w_0^2 E_0 e^{-(k_x^2 + k_y^2)(w_0/2)^2}. \tag{B-4}$$

Interestingly enough, the Fourier transform is also a Gaussian function.

The electromagnetic field in the half space $z>0$ can be obtained (Smith 1997) from the expression

$$\boldsymbol{E}(x, y, z) = \frac{1}{(2\pi)^2} \int_{-\infty}^{\infty} \int_{-\infty}^{\infty} \left(\hat{y} - \frac{k_y}{k_z} \hat{z} \right) F_y(k_x, k_y) e^{-j(k_x x + k_y y + k_z z)} dk_x dk_y. \tag{B-5}$$

The integration of (B-5) for an arbitrary point in space cannot be performed in closed form. Fortunately, the problem can be simplified considerably by applying the paraxial (or Fresnel) approximation. In this approximation, we assume that the spectral function is of negligible amplitude except for vector wave numbers that are nearly parallel to the z axis. In mathematical terms, this means

$$F_y(k_x, k_y) \approx 0, \tag{B-6}$$

unless

$$\sqrt{k_x^2 + k_y^2} \ll k_0, \tag{B-7}$$

where k_0 is the magnitude of the vector wave number in free space. The wave number k_z is then approximately given by

$$k_z = \sqrt{k_0 - (k_x^2 + k_y^2)} \approx k_0 \left(1 - \frac{(k_x^2 + k_y^2)}{2k_0^2} \right), \tag{B-8}$$

in the exponential term of (B-5), and by

$$k_z \approx k_0, \tag{B-9}$$

elsewhere. The second order term for the wave number is kept in the exponential term to take account of its greater sensitivity to errors.

The electric field becomes

$$\boldsymbol{E}(x, y, z) = \frac{1}{(2\pi)^2} e^{-jk_0 z} \int_{-\infty}^{\infty} \int_{-\infty}^{\infty} \left(\hat{y} - \frac{k_y}{k_0} \hat{z} \right) F_y(k_x, k_y) e^{-j\left(k_x x + \frac{k_x^2 z}{2k_0}\right)} e^{-j\left(k_y y + \frac{k_y^2 z}{2k_0}\right)} dk_x dk_y \, .$$

(B-10)

which can be rewritten as

$$\boldsymbol{E}(x, y, z) = \frac{1}{(2\pi)^2} e^{-jk_0 z} \left(\hat{y} - \hat{z} \frac{j}{k_0} \frac{\partial}{\partial y} \right) \int_{-\infty}^{\infty} \int_{-\infty}^{\infty} F_y(k_x, k_y) e^{-j\left(k_x x + \frac{k_x^2 z}{2k_0}\right)} e^{-j\left(k_y y + \frac{k_y^2 z}{2k_0}\right)} dk_x dk_y \, .$$

(B-11)

The spectral function (B-4) satisfies the conditions (B-6) and (B-7) provided that $k_0 w_0 >> 1$. The beam waist must be large compared to the wavelength. After substituting (B-4) into (B-11) and using (B-3), the electric field of the Gaussian beam becomes

$$\boldsymbol{E}(x, y, z) = \frac{E_0 w_0}{w(z)} e^{j\Phi(z)} \left[\hat{y} + j \frac{\gamma(y) w_0}{w(z)} e^{j\Phi(z)} \hat{z} \right] e^{-\left(\frac{\rho}{w(z)}\right)^2} e^{-j\left(k_0 z + \frac{k_0 \rho^2}{2\Gamma(z)}\right)}. \tag{B-12}$$

where

$$\begin{aligned} \gamma(y) &= 2y/k_0 w_0^2 \\ \Phi(z) &= \tan^{-1}(2z/k_0 w_0^2) \\ w(z) &= w_0 \sqrt{1 + (2z/k_0 w_0^2)^2} \\ \Gamma(z) &= z[1 + (k_0 w_0^2/2z)^2] \end{aligned} \tag{B-13}$$

The function $w(z)$ is called the beam radius and defines a circle into which 86% of the total power of the beam is concentrated. When z=0, then $w(z)$=w_0. $\Gamma(z)$ is the the radius of curvature of the wavefronts for points along the axis of the beam (the z axis). Near the beam waist, the wavefronts are planar ($\Gamma(z)$ becomes infinite), then their radius of curvature decreases to a minimum at the *Rayleigh range* (z=$k_0 w_0^2/2$), after which they begin to propagate as spherical wavefronts with increasing $\Gamma(z)$. $\Phi(z)$ is a phase retardation term which corresponds to a cumulative excess delay of the wavefront, in comparison with a plane wave or a spherical wave, as it travels along z. This phenomenon is known as the Guoy effect.

Generally speaking, the z directed component of the field is completely negligible. Furthermore, a paraxial electromagnetic wave behaves locally as a TEM plane wave. At each point, the vectors $\boldsymbol{E}$ and $\boldsymbol{H}$ lie in a plane tangential to the wavefront surfaces; that is, normal to the vector wave number $\boldsymbol{k}$. The optical power flows along the direction $\boldsymbol{E} \times \boldsymbol{H}$,

which is parallel to $\boldsymbol{k}$, which is approximately parallel to z. The intensity is thus approximately given by the expression appropriate for TEM plane waves; that is,

$$I = \frac{|E|^2}{2\eta}, \tag{B-14}$$

where $\eta=(\mu/\varepsilon)^{1/2}$ is the impedance of the medium. The total power flow is obtained by integrating the intensity over a reference plane of constant z. Setting this power to 1 W, we can constrain the value of E_0. Thus, using z=0 as a reference plane,

$$\begin{aligned} P &= \frac{E_0^2}{2\eta}\int_0^{2\pi}\int_0^{\infty} e^{-2\rho^2/w_0^2}\rho\, d\rho\, d\varphi \\ &= \frac{E_0^2}{2\eta}(2\pi)\frac{w_0^2}{4} = \frac{\pi E_0^2 w_0^2}{4\eta} = 1 \end{aligned} \tag{B-15}$$

The electric field of the normalized Gaussian beam becomes

$$\boldsymbol{E}(x, y, z) = \frac{2\sqrt{\eta/\pi}}{w(z)} e^{j\Phi(z)} e^{-\left(\frac{\rho}{w(z)}\right)^2} e^{-j\left(k_0 z + \frac{k_0\rho^2}{2\Gamma(z)}\right)}\hat{y}. \tag{B-16}$$

which will be the expression used in chapter 2. Obviously, the choice of the y direction for polarization is arbitrary, which can take any direction orthogonal to the z axis.

Appendix C

Mathematica programs

C.1 HeModeSolver.m

```
(* :Title: HeModeSolver.m *)

(* :Context: MyPackages`HeModeSolver` *)

(* :Author: Frederick Mathieu *)

(* :Summary: Determines the set of allowed HE modes in a specified weakly-guiding
cylindrical single-clad optical fiber. Also solves the characteristic equation for the eigen-
value. U, for each of the allowed HE modes*)

(* :Copyright: © 1999 by Frederick Mathieu *)

(* :Package Version: 1.0 *)

(* :Mathematica Version: 3.0 *)

(* :Keywords: Optical fiber, caracteristic equation *)

(* :Sources: Frederick Mathieu 1999, M.Eng. thesis, McGill University*)

(* :Limitations: The function BesselJZeros[8,x] displays odd behavior when used as an
argument for other functions. To work around the problem. I simply generated a list of its
values which where assigned to grr which then was used as the argument.*)

(* :Requirements: NumericalMath/BesselZeros.m*)
```

```
(* set up the package context, including public imports *)

BeginPackage["MyPackages`HeModeSolver`"]

(* usage messages for the exported functions and the context itself *)

HeModeSolver::usage = "HeModeSolver.m is a package that determines the set of allowed HE modes in a specified weakly-guiding cylindrical single-clad optical fiber. Also solves the characteristic equation for the eigenvalue, U, for each of the allowed HE modes."

CutOff::usage = "Cutoff[v_] creates a list of the cutoff values of U<=v for the HElm modes."

HeModeSolve::usage = "HeModeSolve[v_] creates a list of the eigenvalues of the allowed HE modes for a given value of the normalized frequency v."


Begin["`Private`"]   (* begin the private context (implementation part) *)

Needs["NumericalMath`BesselZeros`"]


(* definition of auxiliary functions*)


CutOff[v_]:=

Module[{temp={},result={},i,j=0,k=0,grr={}},

(*Creates a list the cutoffs of HE1m, which satisfies J_-1(cutoff)=-J_1(cutoff)=0,and must also include cutoff=0*)

For[i=1,BesselJZeros[1,{i,i}][[1]]<=v,i++,j=i];

result=Append[result,Prepend[BesselJZeros[1,j],0]]; j++; (*to compensate for the added 0*)

(* Appends the list of the cutoffs of HElm where l>1, which satisfie J_l-2(cutoff)=0, and must not include cutoff=0*)

grr=BesselJZeros[8,75];

While[If[temp!={},Last[temp]>v,False],grr=Delete[grr,Length[grr]]]; (* For Unknown reasons, BesselJZeros[8,j] hangs in functions*)
```

```
While[j>0,

If[k!=8,temp=BesselJZeros[k,j],temp=grr];

While[If[temp!={},Last[temp]>v,False],temp=Delete[temp,Length[temp]]];

j=Length[temp]; If[temp!={},result=Append[result,temp]]; k++];

Return[result]

] (*end of cutoff module*)


HeModeSolve[v_]:=

 Module[{c,l,m,result={},temp1={},temp2={}},

 c=CutOff[v];

 l=Length[c];

 Do[m=Length[c[[j]]];

  Do[

temp1=FindRoot[u*(BesselJ[j,u]/BesselJ[j-1,u])==Sqrt[v^2-u^2]*(BesselK[j,Sqrt[v^2-
u^2]]/BesselK[j-1,Sqrt[v^2-u^2]]),{u,c[[j,i]]+0.0001,c[[j,i]],If[m>i,c[[j,i+1]],v]},Damp-
ingFactor->1/3,MaxIterations->200];

 temp2=Append[temp2,temp1],{i,1,m}];result=Append[result,temp2];temp2={},{j,1,l}];

 result=u/.result;

 Return[result]

 ] (*end of HeModeSolve module*)

End[ ]       (* end the private context *)


Protect[ CutOff, HeModeSolve ]   (* protect exported symbols *)


EndPackage[ ]  (* end the package context *)
```

C.2 CouplingEfficiency.m

```
(* :Title: CouplingEfficiency.m *)

(* :Context: MyPackages`CouplingEfficiency` *)

(* :Author: Frederick Mathieu *)

(* :Summary: Finds the ratio of coupled power to input power, into a completely specified
fiber mode. Assumes a Gaussian beam input.*)

(* :Copyright: © 1999 by Frederick Mathieu *)

(* :Package Version: 1.0 *)

(* :Mathematica Version: 3.0 *)

(* :History: one line description of earlier versions and change log*)(*Optional*)

(* :Keywords:Gaussian beam, optical fiber, mode excitation, coupling efficiency  *)

(* :Sources: Frederick Mathieu 1999, M.Eng. thesis, Mcgill University*)

(* :Warnings: The argument u for the eigenvalues of the modes are not independant to the
normalized frequency v. Thus, incorrect u values for a given v will give physically mean-
ingless results without generating a error message.*)

(* Limitation: Can only handle tilts and offsets in the same direction*)



(*BeginPackage["MyPackages`CouplingEfficiency`"]*)

CouplingEfficiency::usage = "CouplingEfficiency.m is a package that generates a list

of the launching efficiency for the given optical fiber modes excited by a Gaussian beam."

Efficiency::usage = "Efficiency is a function that returns a list

of the launching efficiency for the given optical fiber modes excited by a Gaussian beam."


Begin["`Private`"]
```

```
fl[v_,q_,l_,y_]/;y<=1 := BesselJ[l-1,q*y]/BesselJ[l-1,q]

fl[v_,q_,l_,y_]/; y>1 := BesselK[l-1,Sqrt[v^2-q^2]*y]/BesselK[l-1,Sqrt[v^2-q^2]]



EfficiencyNoMisAlignment[a_,v_,u_List,d_,w0_,lambda_,z_]:=

Module[{w,r,G,p,ksi,result={}},

w=w0*Sqrt[1+((z*lambda)/(Pi*w0^2))^2];

r=z*(1+((Pi*w0^2)/(z*lambda))^2);

Do[

ksi=BesselK[1,Sqrt[v^2-u[[1,i]]^2]]*BesselK[-1,Sqrt[v^2-u[[1,i]]^2]]/
(BesselK[0,Sqrt[v^2-u[[1,i]]^2]])^2 :

G=NIntegrate[x*fl[v,u[[1,i]],1,x]*Exp[-((a*x)^2)*((1/w^2)+(I*Pi)/
(lambda*r))],{x,0,d},MaxRecursion->10,AccuracyGoal->6,PrecisionGoal->6];

 p=(8/ksi)*(Abs[(a*u[[1,i]]*G)/(w*v)])^2;

 Print[i," ",p,"   ",G];

 result=Append[result,p],{i,1,Length[u[[1]]]}];

Return[{result}]

| (*end of EfficiencyNoMisAlignment module*)



EfficiencyOffset[a_,v_,u_List,d_,w0_,lambda_,z_,of_]:=

Module[{w,r,G,p,ksi,sca,result={},result2={}},

w=w0*Sqrt[1+((z*lambda)/(Pi*w0^2))^2];

r=z*(1+((Pi*w0^2)/(z*lambda))^2);

 sca=Exp[-(of/w)^2];

 Print[sca];

Do[
```

```
Do[

ksi=BesselK[j,Sqrt[v^2-u[[j,i]]^2]]*BesselK[j-2,Sqrt[v^2-u[[j,i]]^2]]/(BesselK[j-
1,Sqrt[v^2-u[[j,i]]^2]])^2 ;

G=NIntegrate[sca*x*fl[v,u[[j,i]],j,x]*Exp[-((a*x)^2)*((1/w^2)+(I*Pi)/
(lambda*r))]*BesselI[j-1,2*a*x*of*((1/w^2)+(I*Pi)/(lambda*r))]

,{x,0,d},MaxRecursion->10,AccuracyGoal->6,PrecisionGoal->6];

p=(8/ksi)*(Abs[(a*u[[j,i]]*G)/(w*v)])^2;

Print[i," ",j," ",p,"    ",G];


result=Append[result,p],{i,1,Length[u[[j]]]}];result2=Append[result2,result];result={},{j,
1,Length[u]}];

Return[result2]

] (*end of EfficiencyOffset module*)



EfficiencyTilt[a_,v_,u_List,d_,w0_,lambda_,z_,an_]:=

Module[{w,r,G,p,ksi,result={},result2={}},

w=w0*Sqrt[1+((z*lambda)/(Pi*w0^2))^2];

r=z*(1+((Pi*w0^2)/(z*lambda))^2);

Do[

Do[

ksi=BesselK[j,Sqrt[v^2-u[[j,i]]^2]]*BesselK[j-2,Sqrt[v^2-u[[j,i]]^2]]/(BesselK[j-
1,Sqrt[v^2-u[[j,i]]^2]])^2 ;

G=NIntegrate[x*fl[v,u[[j,i]],j,x]*Exp[-((a*x)^2)*((1/w^2)+(I*Pi)/(lambda*r))]*BesselJ[j-
1,a*x*an*2*Pi/lambda]

,{x,0,d},MaxRecursion->10,AccuracyGoal->6,PrecisionGoal->6];

p=(8/ksi)*(Abs[(a*u[[j,i]]*G)/(w*v)])^2;

Print[i," ",j," ",p,"    ",G," ",ksi];
```

```
result=Append[result,p],{i,1,Length[u[[j]]]}];result2=Append[result2,result];result={},{j,
1,Length[u]}];

Return[result2]

] (*end of EfficiencyTilt module*)



EfficiencyOffsetPlusTilt[a_,v_,u_List,d_,w0_,lambda_,z_,of_,an_]:=

Module[{w,r,G,p,ksi,sca,result={},result2={}},

w=w0*Sqrt[1+((z*lambda)/(Pi*w0^2))^2];

r=z*(1+((Pi*w0^2)/(z*lambda))^2);

 sca=Exp[-(of/w)^2];

 Print[sca];

Do[

Do[

ksi=BesselK[j,Sqrt[v^2-u[[j,i]]^2]]*BesselK[j-2,Sqrt[v^2-u[[j,i]]^2]]/(BesselK[j-
1,Sqrt[v^2-u[[j,i]]^2]])^2 ;

G=NIntegrate[sca*x*fl[v,u[[j,i]],j,x]*Exp[-((a*x)^2)*((1/w^2)+(I*Pi)/
(lambda*r))]*BesselI[j-1,2*a*x*of*((1/w^2)+(I*Pi)/(lambda*r)-(I*Pi*an)/(lambda*of))]

  ,{x,0,d},MaxRecursion->10,AccuracyGoal->6,PrecisionGoal->6];

  p=(8/ksi)*(Abs[(a*u[[j,i]]*G)/(w*v)])^2;

  Print[i,"  ",j,"  ",p,"    ",G];


result=Append[result,p],{i,1,Length[u[[j]]]}];result2=Append[result2,result];result={},{j,
1,Length[u]}];

Return[result2]

] (*end of EfficiencyOffsetPlusTilt module*)
```

```
Efficiency[a_,v_,u_List,d_,w0_,lambda_,z_,of_,an_]/;((of==0)&&(an==0)):=Efficiency
NoMisAlignment[a,v,u,d,w0,lambda,z]

Efficiency[a_,v_,u_List,d_,w0_,lambda_,z_,of_,an_]/;((of!=0)&&(an==0)):=Efficiency
Offset[a,v,u,d,w0,lambda,z,of]

Efficiency[a_,v_,u_List,d_,w0_,lambda_,z_,of_,an_]/;((of==0)&&(an!=0)):=Efficien
cyTilt[a,v,u,d,w0,lambda,z,an]

Efficiency[a_,v_,u_List,d_,w0_,lambda_,z_,of_,an_]/;((of!=0)&&(an!=0)):=Efficiency
OffsetPlusTilt[a,v,u,d,w0,lambda,z,of,an]

End[ ]      (* end the private context *)
Protect[CouplingEfficiency]   (* protect exported symbols *)
EndPackage[ ]
```

References

Antar, Y.M., and Boerner, W.M. 1973, "Gaussian Beam Interaction with a Planar Dielectric Interface", Canadian Journal of Physics, 52, 962

Brenner, K.H., and Huang, A. 1988, "Optical Implementation of the Perfect Shuffle Interconnection", Applied Optics, 27, 135

Cartledge, J.C. 1978, "Excitation of a Doubly Clad Optical Fiber by Misaligned Gaussian Beams", Applied Optics, 17, 2086

Chandra, R. 1979, "Fundamental Mode Excitation by Tilted or Off-Axis Gaussian Beams in a Tube Waveguide With an Outer Higher-Index Cladding", Wave Electronics, 3, 335

Choquette, K.D., Schneider, R.P., Jr., Lear, K.L., and Geib, K.M. 1994, "Record Performance from Vertical-Cavity Lasers Fabricated by Selective Oxidation", Proceedings of the 14th IEEE Semiconductor Laser Conference, post deadline paper 4, 10

Collin, R.E. 1960, Field Theory of Guided Waves (New York: McGraw-Hill)

Cryan, C.V. 1998, "Two-Dimensional Multimode Fiber Array for Optical Interconnects", Electronics Letters, 34, 586

El-Mikati, H.A., and Davies, J.B. 1985, "Coupling to an Endfaced Multi-clad Optical fiber from a Misaligned Gaussian Beam or a Separated Multi-clad fiber", Optical Quantum Electronics, 17, 297

Gloge, D. 1971, "Weakly Guiding Fibers", Applied Optics, 10, 2252

Hayashi, Y., Mukaihara, T., Hatori, N., Ohnoki, N., Matsutani, A., Koyama, F. and Iga, K. 1996, "Lasing Characteristics of Low-Threshold Oxide Confinement InGaAs-GaAlAs Vertical-Cavity Surface-Emitting Lasers", IEEE Photonics Technology Letters, 7, 1324

Hinton, H.S., Cloonan, T.J., McCormick, F.B., Jr., Lentine, A.L., and Tooley, F.A.P. 1994, "Free-Space Digital Optical Systems", Proceedings of the IEEE, 82,1632

Horowitz, B.R., and Tamir, T. 1971, "Lateral Displacement of a Light Beam at a Dielectric Interface", Journal of the Optical Society of America, 61, 586

Iga, K., Koyama, F., and Kinoshita, S. 1988, "Surface Emitting Semiconductor Lasers", IEEE Journal of Quantum Electronics, 24, 1845

Imai, M., and Hara, E.H. 1974, "Excitation of Fundamental and Low-Order Modes of Optical Fiber Waveguides by Gaussian Beams. 1: Tilted Beams", Applied Optics, 13, 1893

Imai, M., and Hara, E.H. 1975, "Excitation of Fundamental and Low-Order Modes of Optical Fiber Waveguides by Gaussian Beams. 1: Offset Beams", Applied Optics, 14, 169

Jäger, R., Grabherr, M., Jung, C., Michalzik, R., Reiner, G., Weigl, B., and Ebeling, K.J. 1997, "57% Wallplug Efficiency Oxide-Confined 850 nm Wavelenght GaAs VCSELs", Electronic Letters, 33, 330

Jahns, J., and Murdocca, M.J. 1988, "Crossover Networks and their Optical Implementation", Applied Optics, 27, 3155

Kawai, S. 1997, "Skew- Free Optical Interconnections Using VCSEL-Based Fiber Image-Guides", MOC/GRIN '97. Technical Digest of the Sixth Microoptics Conference and the Fourteenth Topical Meeting on Gradient-Index Optical Systems. Japan Soc. Appl. Phys., 78

Kirk, A., Mathieu, F., Lacroix, F., Plant, D., Mony, M., Khurana, P., Cryan, C., Tateno, K., and Kurokawa, T. 1997, "Two-Dimensional Interconnects with Fiber Arrays". MOC/GRIN '97. Technical Digest of the Sixth Microoptics Conference and the Fourteenth Topical Meeting on Gradient-Index Optical Systems. Japan Soc. Appl. Phys., 296

Koepf, G.A., and Marly, B.J. 1984, "Fabrication and Characterization of a 2-D Fiber Array", Applied Optics, 23, 3515

Kosaka, H., Kajita, M., Li, Y., and Sugimoto, Y. 1997, "A Two-Dimensional Optical Parallel Transmission Using a Vertical-Cavity Surface-Emitting Laser Array Module and an Image Fiber", IEEE Photonics Technology Letters, 9, 253

Kosaka, H., Kajita, M., Yamada, M., and Sugimoto, Y. 1997, "A 16x16 Optical Full-Cross-Bar Connection Module with VCSEL-Array Push/Pull Module and Polymer-Waveguide Coupler Connector", IEEE Photonics Technology Letters, 9, 244

Kozaki, S., and Sakurai, H. 1977, "Characteristics of a Gaussian Beam at a Dielectric Interface", Journal of the Optical Society of America, 68, 508

Lebby, M., Gaw, C.A., Jiang, W., Kiely, P.A., Shieh, C.L., Claisse, P.R., Ramadani, J., Hartman, D.H, Schwartz, D.B., and Grula, J. 1996, "Characteristics of VCSEL Arrays for Parallel Optical Interconnections", Proceedings of the 46th Electronic Components and Technology Conference, 279

Marcuses, D. 1970, "Excitation of the Dominant Mode of a Round Fiber by a Gaussian Beam", Bell Systems Techical Journal, 49, 1695

Miller, D. 1997, "Physical Reasons for Optical Interconnection", International Journal of Optoelectronics, 11, 155

Miyagi, M., Yoneyama, T., and Nishida, S. 1975, "Theoretical Study of Excitation of Clad Optical Fibers by a Cylindrical Gaussian Beam", Electronics and Communications in Japan, 58-C, 96

Morgan, R.A., Chirovski, L.M.F., Focht, M.W., Guth, G., Asom, M.T., Leibenguth, R.E., Robinson, K.C., Lee, Y.H., and Jewell, J.L. 1991, "Progress in Planarized Vertical Cavity Surface Emitting Laser Devices and Arrays", Proceedings of Spie - the International Society for Optical Engineering, 1562, 149

Morgan, R.A., Guth, G.D., Focht, M.W., Asom, M.T., Kojima, K., Rogers, L.E., and Callis, S.E. 1993, "Transverse Mode Control of Vertical-Cavity Top-Surface-Emitting Lasers", IEEE Photonics Technology Letters, 5, 374

Morgan, R.A., Hibbs-Brenner, M.K., Lehman, J.A., Kalweit, E.L., Walterson, R.A., Marta, T.M., and Akinwande, T. 1995, "Hybrid Dielectric/AlGaAs Mirror Spatially Filtered Vertical Cavity Top-Surface Emitting Laser", Applied Physics Letters, 66, 1157

Morse, P., and Feshbach, H. 1953, Methods of Theoretical Physics (New York: McGraw-Hill)

Mostafavi, M., Itoh, T., and Mittra, R. 1975, "Excitation of an Optical fiber by a Gaussian Beam", Applied Optics, 14, 2190

Mukaihara, T., Ohnoki, N., Hayashi, Y., Hatori, N., Koyama, F., and Iga, K. 1995, "Excess Intensity Noise Originated From Polarization Fluctuation In Vertical-Cavity Surface-Emitting Lasers", IEEE Photonics Technology Letters, 7, 1113

Plant, D. 1997, "Packaging techniques for smart pixel optoelectronics", International Journal of Optoelectronics, 11, 169

Proudley, G.M., Stace, C., and White, H. 1994, " Fabrication of Two-Dimensional Fiber Optic Arrays for an Optical Crossbar Switch", Optical Engineering, 33, 627

Ra, J.W., Bertoni, H.L., and Felsen, L.B.1973, "Reflection and Transmission of Beams at a Dielectric Interface", SIAM Journal of Applied Mathematics, 24, 396

Sandusky, J.V., and Brueck, S.R.J. 1996, "A CW External-Cavity Surface-Emitting Laser", IEEE Photonics Technology Letters, 8, 313

Sasian, J.M., Novotny, R.A., Beckman, M.G., Walter, S.L., Wojcik, M.J., and Hinterlong, S.J. 1994, "Fabrication of Fiber Arrays for Optical Computing and Switching Systems", Optical Communication, WD6, 229

Siegman , A.E. 1986, Lasers (Mill Valley: University Science Books)

Smith, G.S. 1997, " An Introduction to Classical Electromagnetic Radiation" (New York: Cambridge University Press)

Schnitzer, P., Fiedler, U., Grabherr, M., Jung, C., Reiner, G., Zick, W., and Ebeling, K.J. 1996, "Bias-Free 1 Gb/s Data Transmission Using Single-Mode GaAs VCSELS at λ=835 nm", Electronics Letters, 32, 2145

Snyder, A.W. 1969a "Asymptotic Expressions for Eigenfunctions and Eigenvalues of a Dielectric or Optical Waveguide", IEEE Transactions on Microwave Theory and Techniques, MTT-17, 1130

Snyder, A.W 1969b, "Excitation and Scattering of Modes on a Dielectric or Optical fiber", IEEE Transactions on Microwave Theory and Techniques, MTT-17, 1138

Stern, J.R., Peace, M., and Dyott, R.B. 1970, "Launching into Optical-Fibre Waveguides", Electronic Letters, 6, 160

Stern, J.R., and Dyott, R.B 1971, "Off-Axis Launching into a Fibre-Optical Waveguide", Electronic Letters, 7, 52

Stratton, J.A. 1941, Electromagnetic Theory (New York: McGraw-Hill)

Sutherland, J.S. 1997, "Optical Coupling Modeling and Passive alignment techniques for Parallel Optoelectronic Interfaces", Ph.D. thesis, Cornell University

Takahashi, M., Egami, N., Mukaihara, T., Koyama, F., and Iga, K. 1997, "Lasing Characteristics of GaAs(311)A Substrate Based InGaAs-GaAs Vertical-Cavity Surface-Emitting Lasers", IEEE Journal of Selected Topics in Quantum Electronics, 3, 372

Tooley, F.A.P. 1996, "Challenges in Optically Interconnecting Electronics", IEEE Journal of Selected Topics in Quantum Electronics, 2, 3

White, I.A., Snyder, A.W., and Pask, C. 1977, "Directional Change of Beams Undergoing Partial Reflection", Journal of the Optical Society of America, 67, 703